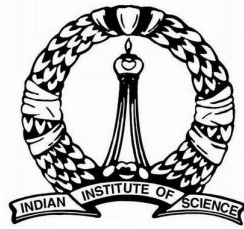


Correlation, superconductivity, and topology in twisted and untwisted layered systems

A THESIS
SUBMITTED FOR THE DEGREE OF
Doctor of Philosophy
IN THE FACULTY OF SCIENCE

by
Sujay Ray



Department of Physics
Indian Institute of Science
Bangalore - 560012

Declaration

I hereby declare that the work reported in this thesis is original. It was carried out by me during my tenure as an Int. Ph.D. student at the Department of Physics, Indian Institute of Science, Bangalore. This thesis has not formed the basis for the award of any degree, diploma, associateship, membership or similar title of any university or institution. Wherever contributions of others are involved, every effort is made to indicate this clearly, with due reference to the literature, and acknowledgement of collaborative research.

The work is done under the supervision of Dr. Tanmoy Das.

Sujay Ray

28th September, 2021

Acknowledgment

The accelerating progress in the field of science is the result of sharing our knowledge and ideas. One of the most important things I learnt from my Ph.D. supervisor Prof. Tanmoy Das is that - only through discussions we are able to sharpen our understanding and broaden our views. I am grateful to Tanmoy for the countless discussions we had on various fields of Physics, some of which have shaped the current thesis. His attitude towards Physics to intuitively understand the subject in its simplest form is always inspiring. At the same time, his continuous effort to push for creative ideas taught me to grow independently. Every small effort to understand Physics was always appreciated by him. Even if it started with a failed initial effort, his encouragement would make it converge self-consistently to a successful understanding. I thank him for all the academic and non-academic support and most importantly for guiding with my Ph.D. work.

I sincerely thank Prof. Jeil Jung and Bheema Lingam Chittari for collaborative projects and many illuminating discussions. Working with them was a great learning experience for me. I am greatly thankful to Kapildeb Dolui for collaboration in my first project and various helps and discussions on DFT in other projects as well.

I thank Prof. Aveek Bid, Prof. Anindya Das and Prof. Srimanta Middey for experimental collaboration, which gave me inspiring and widening view of the experimental front of the current Physics problems and correlate them with theoretical understanding. I thank Sourav Srivastav, Priya Tiwary, Hemanta Kundu, Shashank Kumar Ojha and Manebendra Kuri for collaborative experimental studies. I acknowledge Prof. Subroto Mukerjee and Prof. Aindam Ghosh for the summer projects and all the faculties of Physics department of IISc - Prof. Diptiman Sen, Prof. Sumilan Banerjee, Prof. Vijay Shenoy, Prof. Manish Jain, Prof. Chandan Das Gupta for their insightful suggestions and discussions. I thank all the past and present department Chairs and all the office staff. I express my gratitude to Srinivas for numerous helps with cluster support and SERC for the supercomputer facility, which made our projects possible.

I am thankful to my group members - Priyo Adhikari, Kale Bala Yogendra Babu, Priyanshi

Bhasin, Partha Sarathi Rana, Suman Karmakar for insightful discussions. I sincerely thank Sibaram Ruidas for the help with Monte Carlo simulation. I am thankful to my seniors - Gaurav, Rituparno, Ananya, Abhash, Adheep, Sayoni and my juniors - Debasmita, Sudipta, Joyita, Jagannath for various discussions. My batchmates - Kausik, Soumi, Arup, Manas, Aswini, Neha, Ramya, Mithun, Soutik were constant companions for all the years of staying in IISc. They along with my friends from other departments - Tanaya, Paramita, Jyotirmoy, Sanhita, Manujda, Sangramda, Abhirukda made the hostel life exciting and enjoyable through numerous discussions on life, politics and through our adventurous trekkings in the Himalayas.

I am grateful to the great Physicists and Scientists, whose knowledge and understanding is the foundation of my research in Physics. I am grateful to all the philosophers and artists for their illuminating views towards the pursuit of truth. I specially thank great painters for inspiring me with their timeless creations, which is always a source of peace and tranquility. I greatly acknowledge all the men and women in history who dedicated their lives to establish science and logic.

Lastly, I would like to express my gratitude for my parents - my mother for supporting and guiding me from my childhood and my father for inspiring me to go for higher knowledge and wisdom in life. And I sincerely acknowledge the constant support from Armin in difficult times. I thank her for numerous illuminating discussions on science and philosophy and for her delightful inspiration.

Preface

This thesis is an effort to understand some of the interesting features induced by strong correlation - superconductivity, topology, non-Fermi liquid (NFL) in two dimensional (2D) layered materials. 2D layered materials are exciting due to their extreme tunability and the rich physics that can be invoked without worrying about the complexity of three dimension. In this thesis I explore various interplay of these tuning parameters and their manifestation in real 2D materials.

This thesis has five chapters. In Chapter 1, I introduce some basic concepts like Fermi liquid (FL), NFL, superconductivity, topology etc. to facilitate the understandings in the subsequent chapters. In chapter 2, I present the non-Fermi liquid (NFL) behavior due to momentum-dependent density-density fluctuation method in cuprates. In Fermi-liquid (FL) theory, the imaginary part of the self-energy scales quadratically with energy, which changes to linear behavior in an NFL case. My calculation shows that due to strong momentum dependent distributions of the itinerant, and local densities, the resulting self-energy becomes strongly anisotropic. The computed self-energy exhibits a marginal-FL (MFL)-like frequency dependence only in the antinodal region, and FL-like behavior elsewhere at all dopings. The DC conductivity shows that the resistivity-temperature exponent $n = 1$ near the optimal doping. Surprisingly, in the extreme NFL state (near the optimal doping in cuprates), MFL-like self-energy occupies the largest volume in momentum space but the nodal region still contains FL-like self-energies. Similarly, in the FL state (in overdoped region), not all quasiparticles are necessarily long-lived and the antinodal region remains NFL-like.

Chapter 3 and 4 are about twisted bilayer systems. Condensed matter systems host a plethora of emergent low-energy properties due to the interplay between electronic structure, magnetism, correlation, and topology. Without losing lattice translational invariance, one can tune this interplay with spatially averaged parameters such as doping, pressure, magnetic field,

and temperature. Twisted bilayers systems give a new tool to achieve local tunability with discrete translational invariance in the Moire supercell. This allows us to study emergent spatial-dependent phases beyond the typical mean-field order parameters. In chapter 3, I study the formation of superconducting pairs of Wannier orbitals in twisted bilayer graphene. Recently, superconductivity is discovered in twisted bilayer graphene (TBG) which is believed to be unconventional in nature. TBG has flat bands in the Moire supercell, which are describable by Wannier orbitals spreading over many graphene unit cells. Here I have studied the spin-fluctuation mediated superconductivity by employing an effective low energy model for TBG and by solving the linearized superconducting gap equation due to spin-fluctuation mediated pairing potential. I found an extended- s wave as the leading pairing symmetry in TBG, in which the nearest neighbor Wannier sites form Cooper pairs. I have also studied similar systems like single-layer graphene (SLG) without a moiré pattern and graphene on boron-nitride (GBN) possessing a different moiré pattern than TBG. Similar calculation shows that GBN has $p + ip$ -wave pairing between nearest-neighbor Wannier states with odd-parity phase, while SLG has the $d + id$ -wave symmetry for inter-sublattice pairing with even-parity phase.

Recent discovery of 2D Van der Waals (VdW) magnetic layers motivated me to study a similar Moire physics in twisted magnetic bilayers. In Chapter 4, I explore the twisted bilayers of 2D VdW magnets where spatially modulated inter-layer interactions arise naturally due to Moire geometry. By considering long-ranged Heisenberg exchange (J_{\perp}) and dipole-dipole (J_D) interlayer interactions and ferromagnetic exchange and z-axis asymmetric intra-layer interactions, I obtain the microscopic spin texture with Monte Carlo simulation. The $J_{\perp} - J_D$ parameter space unveils a hierarchy of distinct skyrmions phases, ranging from point-, rod-, and ring-shaped topological charge distributions. A novel topological antiferroelectric phase is also found, where oppositely charged antiskyrmion pairs are formed, and the corresponding topological charge distribution shows a dipole formation in the Moire supercell. The dipoles become ordered in a Néel-like state, which form a topological antiferroelectric state.

In chapter 5, I conclude the thesis with a brief summary and impact of the works described here and with a discussion on possible future prospects and outlook.

List of Publications

1. Sujay Ray and Tanmoy Das
Coexistence of non-Fermi liquid and Fermi liquid self-energies at all dopings in cuprates
Journal of Physics: Condensed Matter **31**, 36 (2019).
2. Sujay Ray, Jeil Jung, and Tanmoy Das
Wannier pairs in the superconducting twisted bilayer graphene and related systems
Phys. Rev. B **99**, 134515 (2019).
3. Sujay Ray and Tanmoy Das
A hierarchy of multi-order skyrmion phases in twisted magnetic bilayers
Phys. Rev. B **104**, 014410 (2021).

Other publications by the author (not included in the thesis):

4. K. Dolui, S. Ray, and T. Das
Intrinsic large gap quantum anomalous Hall insulators in LaX ($X = Br, Cl, I$)
Phys. Rev. B **92**, 205133 (2015).
5. H. K. Kundu, S. Ray, K. Dolui, V. Bagwe, P. Roy Choudhury, S. B. Krupanidhi, T. Das, P. Raychaudhuri, and A. Bid
Quantum phase transition in few-layer $NbSe_2$ probed through quantized conductance fluctuations
Phys. Rev. Lett. **119**, 226802 (2017).
6. S. K. Ojha, S. Ray, T. Das, S. Middey, S. Sarkar, P. Mahadevan, Z. Wang, Y. Zhu, X. Liu, M. Kareev, J. Chakhalian
Anomalous electron transport in epitaxial $NdNiO_3$ films
Phys. Rev. B **99**, 235153 (2019).

7. P. Tiwari, S. Kumar Srivastav, S. Ray, T. Das, and A. Bid
Observation of time-reversal invariant helical edge-modes in bilayer graphene/ WSe2 heterostructure
ACS Nano **15**, 1, 916–922 (2021).
8. M. Kuri, S. K. Srivastav, S. Ray, K. Watanabe, T. Taniguchi, T. Das, and A. Das
Enhanced electron-phonon coupling in doubly aligned hexagonal boron nitride bilayer graphene heterostructure
Phys. Rev. B **103**, 115419 (2021).

Contents

1	Introduction	1
1.1	Fermi liquid	1
1.2	Non-Fermi liquid	9
1.3	Unconventional superconductivity	16
1.4	Topology	20
1.5	Moiré pattern and twisted bi-layer	31
2	Co-existence of Fermi liquid and non-Fermi liquid	37
2.1	Introduction	37
2.2	Momentum anisotropy in self energy	39
2.3	Perturbative approach and MRDF model	40
2.4	Self energy results	46
2.5	Resistivity calculation	50
2.6	Materials dependence of n and its correlation with T_c	52
2.7	U dependence of various results	54
2.8	Discussions	55
2.9	Outlook and conclusions	67
3	Wannier pairs in superconducting twisted bilayer graphene and related systems	69
3.1	Introduction	69
3.2	Model Hamiltonians for different systems	73
3.3	Electronic structure and FS nestings	77
3.4	Pairing potential calculation	78

3.5	Pairing symmetry calculations	80
3.6	Results	82
3.7	Discussions and conclusions	89
4	Spin topology in twisted bi-layer Moiré pattern	91
4.1	Introduction	91
4.2	Theoretical model for twisted bi-layer spins	94
4.3	Monte Carlo method	98
4.4	Results	100
4.5	Discussions and Conclusions	112
5	Conclusions and outlook	115
A	Appendix for chapter 2	139
A.1	Extraction of the exponents	139
A.2	Details of the MRDF calculations	140
B	Appendix for chapter 4	145
B.1	Ground state spin configurations	145
B.2	Dipole and quadrupole moments in Phase II	146

List of Figures

1.1	Schematic phase diagram of a generic quantum phase transition due to spin fluctuation and phase diagram of Millis model	14
1.2	Feynmann diagrams for Dyson’s equation and the RPA self-energy	17
1.3	Two different types of edge states with Kramer’s degeneracy	25
1.4	Green’s function method for topological invariant in Kane-Mele model	27
1.5	Moiré pattern created in bilayer by twist angle and lattice mismatch	32
2.1	Schematic superconducting phase diagram of LSCO	38
2.2	Schematic diagram showing the self consistent loop of MRDF method	42
2.3	Feynmann diagrams of various quantities of the MRDF model	44
2.4	Density fluctuation spectrum for spin and charge channels in 20% hole doped LSCO	45
2.5	Imaginary part of self-energy at different momentum points in the Brillouin zone for 20 % hole doped LSCO in MRDF method	47
2.6	The self-energy frequency exponent, inverse of quasiparticle weight and spectral weight plots in the entire first quadrant of the Brillouin zone for LSCO at different hole doping	49
2.7	Resistivity vs temperature plot and the resistivity-temperature exponent in the low temperature region as a function of dopings for LSCO	51
2.8	The resistivity temperature exponent at the optimal doping for different cuprate materials	53
2.9	Self-energy frequency exponent for three different values of Hubbard U for LSCO at 20% hole doping	54

2.10	The resistivity temperature exponent at the optimal doping for different cuprate materials for different Hubbard U and the corresponding density of states . . .	55
3.1	Fermi surfaces and lattice structure (Wannier orbitals) for single layer graphene (SLG), graphene on hexagonal boron nitride (GBN) and twisted bilayer graphene (TBG)	71
3.2	Momentum-space formulation of TBG Moiré pattern	76
3.3	RPA spin susceptibility and superconducting pairing symmetry for SLG, GBN and TBG	83
3.4	RPA spin susceptibility and superconducting pairing symmetry for valley interactions in TBG	87
3.5	Maximum pairing eigenvalue (SC coupling constant) λ as a function of chemical potential shift μ for TBG	88
4.1	Twisted bilayer setup and five distinct topological spin configurations in real space	93
4.2	Effective magnetic fields along the z -direction in the Moiré unit cell due to the inter-layer exchange and dipole coupling	98
4.3	Phase diagram of five distinct topological phases in twisted bilayer spin system	101
4.4	Local variation of polarity, vorticity, and topological charge densities in the five different topological phases in twisted bilayer spin system	103
4.5	Topological antiferroelectric phase of antiskyrmion pair	105
4.6	Topological electric field lines for different phases in twisted bilayer spin system	108
4.7	Various structure factors for five different phases in twisted bilayer spin system	109
4.8	Various correlation functions and magnetization at phase transition points in twisted bilayer spin system	111
A.1	Curve fitting procedure for the extraction of frequency exponent of imaginary part of self-energy	139
B.1	Ground state spin configurations from Monte Carlo simulation for different phases	145

B.2 Plots of topological charge density in many Moir'e unit cells 147

List of Tables

2.1	Full tight binding parameters for LSCO	42
4.1	Critical values of r_d and J_{\perp}/J_D at different phase transition points	107
B.1	Values of charge, dipole moments, quadrupole moments in phase II for two different dipole coupling strengths (J_D)	146

Chapter 1

Introduction

In this thesis, I have studied a collection of physical properties connecting many body atomic systems in the condensed matter compounds. My theoretical exploration ranges from modeling of non-Fermi liquid behaviour, superconductivity to topology in both electronic structure and in spatial spin configurations (skyrmion). I have investigated these properties in three dimensional bulk material as well as in various 2D materials, heterostucture, twisted bi-layer graphene and twisted magnetic bi-layer. In this chapter, I give introduction to some of the key concepts in the field of strong correlation and topology, building on previous works, which will set the stage for discussions of my various works in the subsequent chapters.

1.1 Fermi liquid

Landau's Fermi liquid theory [1, 2] describes the behavior of electron gas with small density-density interactions between the electrons. It successfully predicts the low temperature electronic properties of many metals. According to Landau, the effect of (weak) electron electron interaction in a system of electron gas can be captured by a smooth change in the distribution function. In other words, the difference between non-interacting and interacting distribution function is analytic. Physically it means we can take a non-interacting system and slowly tune the interaction strength to the desired value without encountering any phase transition.[3] According to Landau, any interacting system that can be prepared by such a process will have excitations which are in one to one correspondence with the particle and hole excita-

tions of the non-interacting systems. These excitations of the interacting systems are called quasiparticles.[1, 4, 5, 6] However, there are two limits in the tuning process - the rate at which the interaction is switched on (τ_s^{-1}), and the strength of the interaction. The tuning rate (τ_s^{-1}) should be slow enough so that the whole process is adiabatic and the switching time (τ_s) should be smaller than the life time of the quasiparticle. Otherwise the quasiparticle will decay before it is created. And the interaction strength must be smaller than a critical value and the critical value denotes a point at which the ground state of the interacting system becomes unstable (e.g., Stoner instability, Pomeranchuk or Mott instability, leading to phase transition).

The interacting systems that satisfy the above conditions preserve the quantum numbers which are used to describe the non-interacting counterpart. In other words, quantities like total particle number (N), momentum (\mathbf{p}) and spin (σ) are conserved, and are still good quantum numbers for the interacting system. Let us take a non-interacting system at zero temperature and suppose p_F is the Fermi momentum the system (for simplicity here I consider an isotropic Fermi Liquid i.e, the Fermi momentum does not depend on the direction in the momentum space.) This ground state is called the Fermi sea. Now I put a fermion above the Fermi sea with momentum $p > p_F$. If the interaction strength is tuned, the Fermi momentum p_F remains unchanged, and a quasiparticle (excited) state with momentum $\mathbf{p}(p > p_F)$ and spin σ can be defined, or if I remove a particle from Fermi sea with momentum $p < p_F$, I can define a quasihole state with momentum $-\mathbf{p}$ and spin $-\sigma$. The decay rate of such a quasiparticle or quasihole state is proportional to $(p - p_F)^2$ and therefore such states only make sense when the excitations are close to the Fermi surface i.e., $|p - p_F| \ll p_F$. This means the particles on the Fermi surface have zero decay rate or infinite lifetime. So the Fermi surface remains well defined in the FL theory.

The energy due quasiparticle excitations can be described in terms of change in occupation number $\delta n_{\mathbf{p}\sigma} = n_{\mathbf{p}\sigma} - n_{\mathbf{p}\sigma}^0$ where $n_{\mathbf{p}\sigma}^0$ is the occupation density of the ground state, and $n_{\mathbf{p}\sigma}$ is the occupation number after adding the quasiparticle. Landau energy functional is given by[3, 7]

$$\xi(\{n_{\mathbf{p}\sigma}\}) = E - E_0 = \sum_{\mathbf{p}\sigma} \epsilon_{\mathbf{p}\sigma}^0 \delta n_{\mathbf{p}\sigma} + \frac{1}{2} \sum_{\mathbf{p}\sigma, \mathbf{p}'\sigma'} f_{\mathbf{p}\sigma, \mathbf{p}'\sigma'} \delta n_{\mathbf{p}\sigma} \delta n_{\mathbf{p}'\sigma'} + \dots, \quad (1.1.1)$$

where the energy E is measured with reference to the ground state energy E_0 . In the above

equation, the first term is for the energy of isolated quasiparticles ($\epsilon_{\mathbf{p}\sigma}^0$) and the second term represents interactions between quasiparticles. Alternatively it can be said that energy of a quasiparticle in an interacting system is

$$\epsilon_{\mathbf{p}\sigma} = \epsilon_{\mathbf{p}\sigma}^0 + \sum_{\mathbf{p}'\sigma'} f_{\mathbf{p}\sigma, \mathbf{p}'\sigma'} \delta n_{\mathbf{p}'\sigma'} + \dots \quad (1.1.2)$$

The interaction part can further be split into a spin-dependent magnetic (f^a) and spin independent non-magnetic (f^s) part. Because of fermionic property the spin-dependent part is antisymmetric with respect to spin (f^a), while the other one is symmetric (f^s), written as

$$f_{\mathbf{p}\sigma, \mathbf{p}'\sigma'} = f_{\mathbf{p}, \mathbf{p}'}^s + f_{\mathbf{p}, \mathbf{p}'}^a \sigma \sigma'. \quad (1.1.3)$$

In an isotropic Fermi liquid, these terms can further be simplified because the interaction only depends on the relative angle θ between \mathbf{p} and \mathbf{p}' which gives $f_{\mathbf{p}, \mathbf{p}'}^{s/a} = f^{s/a}(\cos \theta)$. By introducing the quasiparticle density of states $N^*(0)$, the interaction terms can be turned dimensionless as

$$F^{s/a}(\cos \theta) = N^*(0) f^{s/a}(\cos \theta). \quad (1.1.4)$$

This dimensionless interaction term can be written in terms of a few parameters with the help of multipole expansion such as

$$F^{s/a}(\cos \theta) = \sum_{l=0}^{\infty} (2l+1) F_l^{s/a} P_l(\cos \theta). \quad (1.1.5)$$

These parameters are called the Landau parameters. Depending on the nature and symmetries of the interaction only a few Landau parameters are sufficient to describe a FL system. One of the key features of the FL theory is the feedback effect which enters via the dependence of the quasiparticle energy on the quasiparticle number density, and vice versa. Quasiparticle number density for a FL is given by

$$n_{\mathbf{p}\sigma} = f(\epsilon_{\mathbf{p}}^{(0)} + \delta\epsilon_{\mathbf{p}\sigma}) = f(\epsilon_{\mathbf{p}}^{(0)}) + f'(\epsilon_{\mathbf{p}}^{(0)}) \delta\epsilon_{\mathbf{p}\sigma}. \quad (1.1.6)$$

So the change in quasiparticle number density becomes $\delta n_{\mathbf{p}\sigma} = n_{\mathbf{p}\sigma} - n_{\mathbf{p}\sigma}^{(0)} = -\delta(\epsilon_{\mathbf{p}}^{(0)})\delta\epsilon_{\mathbf{p}\sigma}$, assuming $f'(\epsilon_{\mathbf{p}}^{(0)}) \rightarrow \delta(\epsilon_{\mathbf{p}}^{(0)})$ at low temperature. With this the feedback effect, the energy functional becomes

$$\delta\epsilon_{\mathbf{p}\sigma} = \delta\epsilon_{\mathbf{p}\sigma}^{(0)} - \sum_{\mathbf{p}'\sigma'} f_{\mathbf{p}\sigma, \mathbf{p}'\sigma'} \delta(\epsilon_{\mathbf{p}}^{(0)}) \delta\epsilon_{\mathbf{p}\sigma}. \quad (1.1.7)$$

This feedback effect is an important feature of the FL theory which results in many interesting outcomes in the response functions, like charge and spin susceptibilities, mass renormalization, scattering rate. In the above equation $\delta\epsilon_{\mathbf{p}\sigma}^{(0)}$ is like change of the chemical potential of the system by some external perturbation and $\delta\epsilon_{\mathbf{p}\sigma}$ is the resultant change of the fully interacting quasiparticle energy which can be seen as the response or effect of the external perturbation. With the assumption that the change in bare quasiparticle potential has a particular multipole symmetry and the response also has the same symmetry, I can write

$$\delta\epsilon_{\mathbf{p}\sigma}^{(0)} = \nu_l Y_{lm}(\mathbf{p}), \quad (1.1.8)$$

$$\delta\epsilon_{\mathbf{p}\sigma} = t_l Y_{lm}(\mathbf{p}), \quad (1.1.9)$$

where $Y_{lm}(\mathbf{p})$ is a spherical harmonic. By combining Eq. (1.1.4)- (1.1.9) I arrive at the important connection between perturbation and response in a FL theory[3]

$$t_l = \frac{\nu_l}{1 + F^{s/a}}. \quad (1.1.10)$$

If the interaction is repulsive $F^{s/a} > 0$, the response is suppressed; where as in case of an attractive interaction $F^{s/a} < 0$, the response is enhanced. In particular, if the interaction is too strong so that $F^{s/a} = -1$, the response formula hits a singularity. Such an instability causes the breakdown of FL theory and is known as the Pomeranchuk instability.[8] These general concepts of the feedback effect can be shown to cause various interesting properties in the FL theory, some of which I shall discuss now. The derivations of all the results are similar to the general one described above.

Mass renormalization and density of states: Fermi velocity of a FL can be defined as

$$v_F = \left(\frac{d\epsilon_p^0}{dp} \right)_{p=p_F}. \quad (1.1.11)$$

Since, the Fermi momentum remains unchanged by interaction we can invoke the usual momentum formula to express effective mass m^* in a FL as $v_F = p_F/m^*$ and the density of states can now be expressed in terms of m^* as

$$\begin{aligned} N^*(\epsilon) &= \frac{p^2}{\pi^2 \hbar^3} \frac{dp}{d\epsilon_p^0}, \\ N^*(0) &= \frac{m^* p_F}{\pi^2 \hbar^3}. \end{aligned} \quad (1.1.12)$$

This implies that the density of states at the Fermi level can be increased with large effective mass.

According to Landau, the effective mass is connected to the dipole component of the interaction, and the feedback effect for mass is expressed as $m^* = m(1 + F_1^s)$. Since the Landau parameter $F_1^s = N^*(0)f_1^s$ and the density of states itself depends on the effective mass, the effective mass formula can be expressed in terms of unrenormalized density of states, which is given by

$$m^* = \frac{m}{1 - N(0)f_1^s}. \quad (1.1.13)$$

The above equation shows that the effective mass becomes very large if the denominator is small and it becomes a heavy electron system, and the electrons become slow. If the denominator is further pushed to zero or $N(0)f_1^s = 1$, it leads to an instability, which can be identified as Mott instability[9] where the electrons become immobile or localized. Apart from transport properties, effective mass also changes the linear specific heat of the system.

Specific heat: Specific heat of a Fermi liquid system is given by[10]

$$\begin{aligned} C_V &= \frac{\partial \epsilon}{\partial T} = \sum_{\mathbf{p}\sigma} \epsilon_{\mathbf{p}\sigma}^{(0)} \left(\frac{\partial f(\epsilon_{\mathbf{p}\sigma}^{(0)})}{\partial T} \right) \rightarrow N^*(0) \int_{-\infty}^{\infty} d\epsilon \epsilon \left(\frac{\partial f(\epsilon)}{\partial T} \right), \\ &= \gamma T \quad \text{where} \quad \gamma = \frac{\pi^2 k_B^2}{3} N^*(0). \end{aligned} \quad (1.1.14)$$

The leading order in temperature dependence is the same as that of a free electron gas. Only the linear coefficient is modified with the renormalized density of states or in terms of effective mass it has increased by a factor of m^*/m .

Charge and spin susceptibility: Charge susceptibility (proportional to compressibility), is a measure of change in number density of quasiparticles for change in chemical potential, which is given by

$$\chi_c = \frac{1}{V} \frac{\partial N}{\partial \mu}. \quad (1.1.15)$$

For a chemical potential shift $\delta \epsilon_{\mathbf{p}\sigma}^{(0)} = -\delta \mu$, the response function changes in an isotropic manner $\delta \epsilon_{\mathbf{p}\sigma} = -\lambda_c \delta \mu$, which gives the expression for λ_c when the feedback effect is included as

$$\lambda_c = \frac{1}{1 + F_0^s}. \quad (1.1.16)$$

Here the symmetric channel is used for non-magnetic effect, and $l = 0$ channel is used for the isotropic process. The change in number density is then given by $\delta N/V = \delta n = \lambda_c N^*(0) \delta \mu$ and the charge susceptibility is given by

$$\chi_c = \lambda_c N^*(0) = \frac{N^*(0)}{1 + F_0^s}. \quad (1.1.17)$$

In a similar manner, the spin susceptibility can be derived by the change in bare quasiparticle energy due to an applied magnetic field B is $\delta \epsilon_{\mathbf{p}\sigma}^{(0)} = -\sigma \mu_F B$, and the response is $\delta \epsilon_{\mathbf{p}\sigma} = -\sigma \lambda_s \mu_F B$, where μ_F is the magnetic moment of an isolated fermion. Taking the feedback

effect leads to

$$\lambda_s = \frac{1}{1 + F_0^a}, \quad (1.1.18)$$

where assymmetric channel is used for magnetic effect, and $l = 0$ for the isotropic process. Change in number density of up-spin and down-spin particles in the presence of a magnetic field is $\delta n_\uparrow = -\delta n_\downarrow = \frac{\lambda_s}{2} N^*(0) \mu_F B$. The net change in magnetization is given by $\delta M = \mu_F (\delta n_\uparrow - n_\downarrow) = \lambda_s N^*(0) \mu_F^2 B$. Spin susceptibility measures the change in magnetization in unit volume for change in magnetic field, and is given by

$$\chi_s = \frac{1}{V} \frac{\partial M}{\partial B} = \lambda_s \mu_F^2 N^*(0) = \frac{\mu_F^2 N^*(0)}{1 + F_0^s}. \quad (1.1.19)$$

Both χ_c and χ_s is suppressed for a repulsive interaction $F_0^{s/a} > 0$, and for $F_0^a = -1$, there is an instability called the Stoner instability[11] which indicates a ferromagnetic quantum critical point.

Spectral function: Landau's FL theory can be described in terms of Feynman diagrams in many body diagrammatic approach or Green's function approach.[12, 13, 14] The Green's function or the propagator for a non-interacting free particle is given by

$$G_0(\mathbf{k}, \omega) = \frac{1}{\omega - \epsilon_{\mathbf{k}} + i\eta_{\mathbf{k}}}, \quad (1.1.20)$$

where ω is the frequency, $\epsilon_{\mathbf{k}}$ is non-interacting dispersion relation, and $\eta_{\mathbf{k}} \rightarrow 0_+$ for $k > k_F$ and $\eta_{\mathbf{k}} \rightarrow 0_-$ for $k < k_F$ which is added to avoid divergence at $\omega = \epsilon_{\mathbf{k}}$. The Fourier transformation of the Green's function gives

$$G_0(\mathbf{k}, \tau) \propto e^{-i\epsilon_{\mathbf{k}}\tau} e^{-|\eta_{\mathbf{k}}|\tau}. \quad (1.1.21)$$

The above equation shows that the imaginary part $\eta_{\mathbf{k}}$ is related to the decay of the particle. Since for non-interacting particle $\eta_{\mathbf{k}}$ is infinitesimally small the particle does not decay fast, or the particle remains stable in its ground state. Spectral function is defined as the imaginary

part of the Green's function

$$A(\mathbf{k}, \omega) = -\frac{1}{\pi} G_0(\mathbf{k}, \omega). \quad (1.1.22)$$

For non-interacting system ($\eta_k \rightarrow 0$ limit) the spectral function is a dirac delta function. When interaction is added the Green's function is modified with the addition of a self energy $\Sigma = \Sigma' + i\Sigma''$, and is given by

$$G(\mathbf{k}, \omega) = \frac{1}{\omega - \epsilon_{\mathbf{k}} - \Sigma' - i\Sigma''}. \quad (1.1.23)$$

By expanding Σ' in linear ω and introducing quasiparticle weight $Z_{\mathbf{k}} = \left(1 - \frac{\partial \Sigma'}{\partial \omega}\right)^{-1}$, the Green's function and spectral weight can be written in terms of modified dispersion $\epsilon_{\mathbf{k}} \rightarrow Z_{\mathbf{k}}(\epsilon_{\mathbf{k}} - \Sigma'(\omega = 0))$ and $\eta_{\mathbf{k}} = Z_{\mathbf{k}}\Sigma''$ as

$$\begin{aligned} G(\mathbf{k}, \omega) &= \frac{1}{\omega - \epsilon_{\mathbf{k}} - i\eta_{\mathbf{k}}}, \\ A(\mathbf{k}, \omega) &= \frac{1}{\pi} \frac{\eta_{\mathbf{k}}}{(\omega - \epsilon_{\mathbf{k}})^2 + \eta_{\mathbf{k}}^2}. \end{aligned} \quad (1.1.24)$$

From Eq. (1.1.24) the spectral function can be predicted as a function of ω . For a fixed value of \mathbf{k} , the spectral function has its highest value when $\omega = \epsilon_{\mathbf{k}}$ and is proportional to $1/\eta_{\mathbf{k}}$. For a FL, $\eta_{\mathbf{k}} \propto \Sigma'' \propto -\omega^2$. So the spectral function has a peak at $\omega = \epsilon_{\mathbf{k}}$ with a continuous background for other ω s, and the width of the peak goes as $\eta_{\mathbf{k}} \propto \omega^2$. So for $k \neq k_F$ the spectral weight peak has a finite broadening proportional to quadratic power of ω , and at $k = k_F$, the spectral weight peak becomes infinitely sharp as $\omega \rightarrow 0$. This peak is called the quasiparticle peak, and can be used to validate the FL ansatz. This suggests that a stable (long-lived) quasiparticle can only be defined for small value of ω , which are the states lying near the Fermi surface. For state at the Fermi surface, the fermions have infinite lifetime, or in other words, in the FL theory the Fermi surface remains stable.

Quasiparticle scattering rate: Scattering process in the FL theory is controlled by the Pauli exclusion principle, which restricts the phase space for scattering. The scattering phenomena happen only within a small phase space volume near the Fermi surface due to conservation

of momentum and energy. The dominant process is the scattering of a quasiparticle state to another state via creation of a quasiparticle-quasihole pair. Suppose, a quasiparticle state with energy $\epsilon_1 > \epsilon_F$ is scattered to a state $\epsilon_2 < \epsilon_1 > \epsilon_F$. To conserve energy, a quasiparticle with energy $\epsilon_3 < \epsilon_F$ will be excited to energy ϵ_4 , creating a quasihole at ϵ_3 state. Such a process, together with temperature contribution makes the scattering rate quadratic in excitation energy and in temperature as

$$\Gamma(\epsilon) \propto [\epsilon^2 + \pi^2 T^2]. \quad (1.1.25)$$

When $|\epsilon_p| \ll \pi k_B T$ thermal excitation is the main reason for scattering, which goes as T^2 . For $|\epsilon_p| \gg \pi k_B T$, the higher energy quasiparticle is dominated by the ϵ_p^2 dependence of the scattering rate.

Resistivity: Starting from the Drude model and substituting the life time as above, one can obtain the resistivity vs temperature relation as

$$\rho(T) = \rho_0 + AT^2. \quad (1.1.26)$$

This resistivity is the electronic contribution. So the co-efficient A comes from the electron-electron scattering, and ρ_0 arises from the impurity scattering. T^2 dependence of ρ is considered as a hallmark of Landau FL theory, and is used extensively in experiments to verify the applicability of FL ansatz.

1.2 Non-Fermi liquid

Deviation from FL behavior, e.g., the T^2 dependence of resistivity or constant specific heat coefficient, is considered as a signature of the non-Fermi liquid (NFL) behavior. One of the main characteristics of FL state is the quasiparticle descriptions. On the basis of this ansatz there are two distinct categories of NFL state. First, there are a few cases of NFL state, where it can be explained by approximate FL concepts. Such examples include FL with disorder or Hertz-Millis model for quantum phase transition in 3D. Quasiparticle concept can still be

used to derive the non-quadratic temperature dependence of resistivity or other temperature dependent properties. In the second scenario, the FL descriptions completely break down, and new theoretical concepts and formalisms are needed to explain such states. Luttinger liquid, fractional quantum Hall states are a few examples where fermionic quasiparticle excitations do not appear. There are also other cases where a well-defined quasiparticle description is not at all possible. E.g., incoherent excitations lead to non-analytic behavior. A well-established theory for the NFL state is not yet known, and it remains an interesting and open field of research.

There is a third way to look at the NFL states, and the non-analyticity that arises in such states (Note that within FL theory also, instability such as Stoner, Pomeranchuk or Mott instability arises which are also signature of a NFL behavior. But, a generic NFL theory beyond these instability is my present interest as seen in many materials). Instead of bulk properties like specific heat or resistivity, one can look into the NFL behavior in the spectral function in terms of self energy. In general the imaginary part of self-energy can be described as $\Sigma''(\omega) \propto -|\omega|^p$ at low frequency ($\omega \rightarrow 0$). $p = 2$ is the FL case and when $p < 2$ the system is said to be in NFL regime, which is reflected in the temperature exponent of resistivity. For simplicity I assume no momentum dependence in p . The real and imaginary part of self-energy are related by the Kramers-Krönig relation as

$$\Sigma'(\omega) = P \int \frac{\Sigma''(\omega')}{\omega' - \omega} d\omega', \quad (1.2.1)$$

where P denotes the principle value. At low frequency the real part of self-energy becomes

$$\Sigma'(\omega \rightarrow 0) = P \int \frac{|\omega'|^p}{\omega'} d\omega'. \quad (1.2.2)$$

From the above equation, it becomes clear if $p < 1$ the integrand diverges at zero frequency. So the self-energy becomes non-analytic. Perturbative approach fails in such cases and demand a completely new theoretical formalism. However, if $1 < p < 2$ self-energy is analytic at low frequency and perturbative methods may be used to describe such states. $p = 1$ is the marginal case where the self-energy is still analytical, and this is known as the marginal Fermi liquid (MFL) behavior. Below, I briefly describe a few well-established theoretical models that gives

NFL states.

1.2.1 Theoretical models for NFL

Multichannel Kondo model: In multichannel Kondo model, developed by Nozières and Blandin,[15] an impurity spin is coupled to several identical conduction bands which are also called channels. The Hamiltonian is given by

$$H_K = \sum_{k,m,\sigma} \epsilon_k a_{km\sigma}^\dagger a_{km\sigma} + J \sum_{k,k',m,\sigma,\sigma'} \mathbf{S} \cdot a_{km\sigma}^\dagger \sigma_{\sigma\sigma'} a_{k'm\sigma'}, \quad (1.2.3)$$

where \mathbf{S} is the impurity spin, $a_{km\sigma}^\dagger \sigma_{\sigma\sigma'} a_{k'm\sigma'} = \mathbf{s}$ are the spins of conduction bands, J is the Kondo coupling constant, and m denotes the orbital channels or degrees of freedom. Three cases can arise depending on the number of conduction channels:

1. $m < 2S$, there are not enough conduction channels to fully compensate the impurity spin. Such undercompensated case may give rise to nonanalytic corrections to local FL behavior.
2. $m = 2S$, when the conduction channels completely compensate the impurity spin. $S = 1/2, m = 1$ gives the normal Kondo problem. This leads to the usual FL behavior.
3. $m > 2S$, when the conduction channels overcompensate the impurity spin. Such case leads to NFL behavior. The length scale over which the impurity spin affects the conduction electrons diverges. Resistivity, specific heat etc. also show a NFL behavior. Exact solutions of multichannel Kondo model for dilute impurities give the low-temperature power law behavior of the specific heat, and the spin susceptibility at zero magnetic field for $S = 1/2$, as[16, 17, 18]

$$C_v/T \sim \chi(T) \sim T^{\frac{4}{m+2}-1}, \quad \text{for } m > 2, \quad (1.2.4)$$

$$C_v/T \sim \chi(T) \sim \log\left(\frac{T}{T_K}\right), \quad \text{for } m = 2. \quad (1.2.5)$$

The leading low-temperature power law for resistivity for $S = 1/2$ and $m \geq 2$ is given by

$$\rho(T) - \rho_0 \sim T^\alpha, \quad \text{where} \quad \alpha = \frac{2}{2+m}. \quad (1.2.6)$$

Disorder induced NFL: As discussed in the context of multichannel Kondo model, there is a characteristic temperature T_K below which FL behavior is observed. The Kondo temperature can be expressed in terms of microscopic parameters J and N_0 , the density of states at Fermi energy.[19, 20] However, if the system has disorder it can lead to a distribution of T_K rather than a well-defined value due to disorder induced fluctuations of J and N_0 . In such situations NFL behavior can exist below the average T_K for the system. Such incidents have been reported in metals near metal-insulator transition in alloys with two different non-magnetic constituents.[21, 22, 23] In heavy fermion materials, NFL behavior is reported due to competition of Kondo screening and interactions of magnetic moments.[24, 25]

Near the critical point, disorder can lead to many anomalous behavior. It has been shown that the interplay between disorder and spin fluctuation near a quantum critical point may result into a NFL behavior with resistivity given by $\rho \sim \rho_0 + AT^\alpha$ where $1 \leq \alpha \leq 1.5$. [26] NFL behavior has appeared also in the context of Griffiths phase where the predicted NFL behavior is described as a competition between RKKY spin interactions and Kondo-moment compensation effect in disorder system.[27] In spin glasses, resistivity $\rho = \rho_0 + AT^{1.5}$ has been predicted in disorder model.[28]

Spin fluctuation mediated NFL: A quantum phase transition is characterized by a continuous phase transition at zero temperature, which is usually driven by quantum fluctuation due to some non-thermal control parameter.[29] Near the critical value of this control parameter (critical point), scaling laws with different temperature exponent deviate from the FL result. In a classical phase transition (phase transition at finite temperature), there is an order parameter ϕ which goes to zero at the transition point. Classical partition function Z_{cl} can be written in terms of this order parameter field $\phi(\mathbf{r})$ which is time independent, and the Landau-Ginzburg-Wilson free energy functional $F_{cl}\{\phi\}$ [30] is defined by

$$Z_{cl} = Z_{cl}^0 \int \mathcal{D}\phi e^{-\beta F_{cl}\{\phi\}}, \quad (1.2.7)$$

where $\beta = 1/k_B T$. In case of a quantum system, the order parameter field has a time dependence, and the partition function can be written in a similar manner considering imaginary time such as

$$Z_q(\beta) = Z^0 \int \mathcal{D}\phi(\mathbf{r}, \tau) e^{-S\{\phi\}}, \quad (1.2.8)$$

where $\mathcal{D}\phi$ denotes path integral. The order parameter ϕ satisfies the condition $\phi(\mathbf{r}, 0) = \phi(\mathbf{r}, \hbar\beta)$ and S denotes the Euclidian action given by

$$S\{\phi\} = \int_0^{\hbar\beta} d\tau \int d^d r \mathcal{L}\{\phi(\mathbf{r}, \tau)\}, \quad (1.2.9)$$

where \mathcal{L} is the Lagrangian density. The Fourier transformation of the action S (say for insulating magnet) can be written as

$$S\{\phi\} = \frac{1}{\beta V} \sum_{\mathbf{k}, \omega_n} \phi_{-\mathbf{k}, \omega_n} \left[\epsilon_0 \left(\delta + \xi_0^2 k^2 \right) \omega_n^2 \right] \phi_{\mathbf{k}, \omega_n} + S_4, \quad (1.2.10)$$

with $\omega_n = 2\pi n k_B T$ is bosonic Matsubara frequency, δ is the non-thermal control parameter, \mathbf{k} is the wave vector of order parameter field, and S_4 is fourth order term. Distance to the critical value of the control parameter (δ_c) is denoted by $r = \delta - \delta_c$. For finite temperature phase transition, only the $\omega_n = 0$ term contributes, but for the $T = 0$ phase transition, all other frequencies also contribute. Thus, in quantum phase transition, temporal fluctuations become important. And because of the difference in the gradient of energy in spatial and time direction, the system becomes anisotropic in time and space. This anisotropy is characterized by a dynamical exponent z , which is defined by the relation $\omega \sim k^z$. Thus the effective dimension near the critical point is $d_{eff} = d + z$. Near the phase transition point, the correlation length ξ and correlation time ξ_τ diverge, which is given by the relation

$$\xi \sim |r|^{-\nu}, \quad \text{and} \quad \xi_\tau \sim \xi^z. \quad (1.2.11)$$

The exponent ν in quantum phase transition is different from its classical counterpart ν_{cl} , where the later is given by $\xi \sim |T - T_c|^{-\nu_{cl}}$.

For $T \neq 0$ the quantum system has a finite length in time direction $L_\tau = \hbar\beta$ where

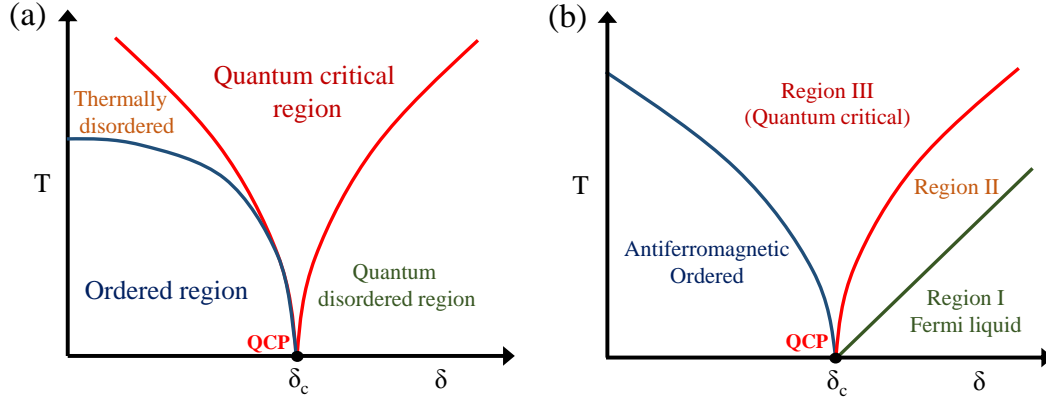


Figure 1.1: (a) Schematic phase diagram of a generic quantum phase transition due to spin fluctuation. (b) Schematic phase diagram of Millis model of quantum phase transition with antiferromagnetic order. Region I is the FL region, region II is quantum to classical crossover region and region III represents quantum critical region. In both figures (a) and (b), T denotes temperature and δ is the non-thermal control parameter such as doping, pressure or external magnetic field, and δ_c is the critical value of the parameter representing quantum critical point (QCP).

$\beta = 1/k_B T$. Fig. 1.1(a) shows a generic phase diagram near a quantum critical point. For $r < 0$ and low- T , there is an ordered phase. The disordered phase on the other hand can be divided into separate regions -

(i) At low T and $r > 0$, it is a quantum disordered state where $L_\tau \gg \xi_\tau$, and thermal effects are negligible in this region. FL behavior is expected here with well defined quasiparticle excitations.

(ii) $T > T_c$ and $r < 0$ is the thermal disordered region, where the order in the ordered phase is destroyed by thermal fluctuation. In this region quasiparticle is still well defined and $L_\tau \gg \xi_\tau$.

(iii) In the region above quantum critical point $\xi_\tau \gg L_\tau$, the quasiparticle is no longer well defined. Instead there is a critical continuum of excitations which results into unusual power law in temperature.

Antiferromagnetic and ferromagnetic ordered phases near QCP has been studied extensively by Hertz[31] and Millis,[32] which shows the value of the dynamical exponent for antiferromagnet is $z = 2$ and for ferromagnet $z = 3$. So for three dimensional systems, the effective dimension is always greater than the upper critical dimension [$d_{eff}(= d + z) > d_c^+(= 4)$]. A schematic phase diagram for the Millis model in the antiferromagnet phase is shown in

Fig. 1.1(b). As discussed in the previous paragraph, antiferromagnetic order appears for low T and $r < 0$. The disordered phase has different regions (see Fig. 1.1(b)). Region I is the FL region where quantum fluctuation dominates over thermal fluctuation. Region II is quantum to classical cross over region where fluctuations are of the order of $k_B T$. Region III is thermally controlled region with critical excitations where temperature exponent has different values than FL. For the antiferromagnetic case, $\rho = \rho_0 + aT^{3/2}$, $C/T = \gamma_0 - a\sqrt{T}$ and for ferromagnetic case $\rho = \rho_0 + cT$, $C/T = a \log(T_0/T)$.

Apart from Hertz and Millis theory, NFL behavior near QCP is also described by so-called self-consistent renormalization (SCR) model developed by Moriya, Takimoto, Kawabata Hasegawa.[33, 34, 35] This model includes some additional coupling between spin-fluctuation than in the theory of Hertz and Millis. SCR model is a one loop approximation for spin fluctuation scattering. It considers weakly interacting spinfluctuation to give a systematic treatment of mode-mode coupling between spin fluctuations at wavevector $q = 0$ and at wavevector of antiferromagnetic order $q = Q$. SCR theory successfully predicts the transition temperature for a large number of d - and f - electron system. It also predicts the same temperature dependence near QCP as in the Hertz-Millis model.

Marginal Fermi liquid (MFL): Marginal Fermi liquid theory proposed by C. M. Verma[36] was aimed to describe linear resistivity behavior in context of high T_c superconductors. MFL phenomenology assumes that polarizabilities (P) has a low energy scale that depends on temperature over a wide range of momentum, charge and spin which is given by

$$\begin{aligned} \text{Im}(P) &\sim -N_0 \frac{\omega}{T}, & \omega \ll T, \\ &\sim -N_0, & T < \omega \ll \omega_c, \end{aligned} \quad (1.2.12)$$

$$\text{Re}(P) \sim N_0 \ln \frac{\omega}{T}, \quad (1.2.13)$$

where ω_c is a cut-off energy. For momentum independent model, which occurs if the Fermi surface is circular, the self energy depends on the frequency ω and temperature T , and takes

the simple form[37]

$$\begin{aligned}\Sigma(\omega, T) &= \left(i\frac{\pi}{2} \max(|\omega|, \pi T) + \omega \ln \left(\frac{\omega_c}{x} \right) \right), \quad \text{for } x = \max(|\omega|, \pi T) \lesssim \omega_c, \\ &= i\frac{\pi}{2} \omega_c, \quad \text{for } \max(|\omega|, \pi T) \gg \omega_c.\end{aligned}\tag{1.2.14}$$

An anisotropy of band structure and consequently anisotropy in Fermi surface would modify the self energy with an additional momentum dependent term as $\Sigma \rightarrow g(\mathbf{k})\Sigma$ where $g(\mathbf{k})$ describes the momentum dependence. It is straightforward to calculate specific heat C_V and resistivity from the above self-energy correction. Heat capacity in the leading order of temperature goes as $C_V \sim T \ln(1/T)$ and the dc conductivity can be calculated from Kubo formula and for $T \rightarrow 0$ is given by

$$\sigma_{dc}(T) \propto \frac{1}{2\text{Im}\Sigma(0, T)}\tag{1.2.15}$$

which gives a temperature dependence of resistivity as $\rho(T) \propto T$.

My work as presented in chapter 2 extends the above calculations to momentum dependent exponent $p_{\mathbf{k}}$ and its manifestation to the NFL behavior.

1.3 Unconventional superconductivity

First successful microscopic theoretical description of superconductivity was given by Bardeen, Cooper, and Schrieffer (BCS theory) in 1957.[38] They assumed a coherent ground state which consists of pair of electrons known as Cooper pair. Such a ground state gives lower energy than the ground state energy of the Fermi sea. Such a pairing between electrons can be obtained from an one-band interacting Hamiltonian as

$$\mathcal{H} = \sum_{\mathbf{k}, s} \varepsilon_{\mathbf{k}} c_{\mathbf{k}s}^\dagger c_{\mathbf{k}s} + \sum_{\mathbf{k}, \mathbf{k}', \mathbf{q}} V_{\mathbf{k}\mathbf{k}'} c_{\mathbf{k}+\mathbf{q}, \uparrow}^\dagger c_{\mathbf{k}'-\mathbf{q}, \downarrow}^\dagger c_{\mathbf{k}'\downarrow} c_{\mathbf{k}\uparrow}.\tag{1.3.1}$$

A Cooper pair order parameter is defined as $\langle c_{\mathbf{k}+\mathbf{q}, \uparrow}^\dagger c_{\mathbf{k}'-\mathbf{q}, \downarrow}^\dagger \rangle$. The most relevant contribution to superconductivity comes from the case where the total linear momentum of a Cooper pair

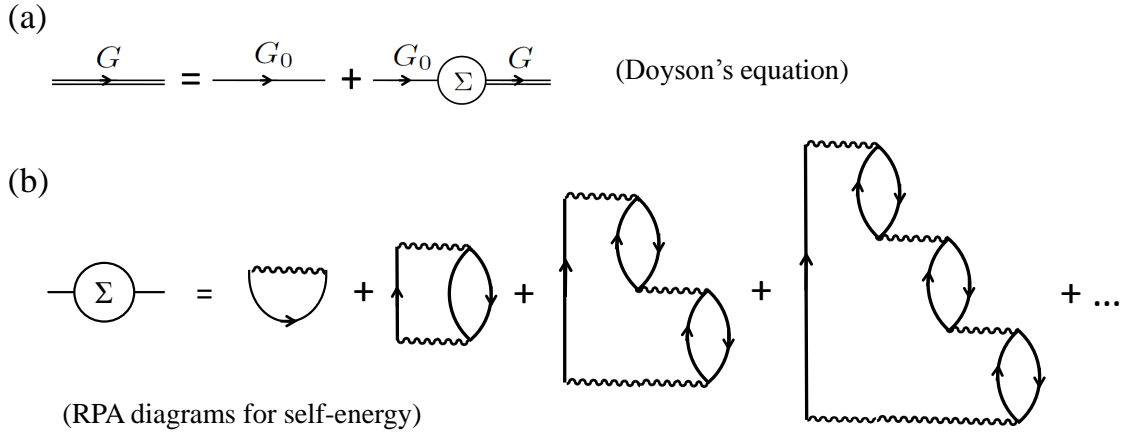


Figure 1.2: Feynmann diagrams for (a) Dyson's equation, and (b) the RPA self-energy. The single solid line represents non-interacting Green's function, the double solid line represents interacting or dressed Green's function, and the curly line represents the Coulomb interactions.

vanishes and the Hamiltonian becomes

$$\mathcal{H} = \sum_{\mathbf{k},s} \varepsilon_{\mathbf{k}} c_{\mathbf{k}s}^{\dagger} c_{\mathbf{k}s} + \sum_{\mathbf{k},\mathbf{k}'} V_{\mathbf{k}\mathbf{k}'} c_{\mathbf{k},\uparrow}^{\dagger} c_{-\mathbf{k},\downarrow}^{\dagger} c_{-\mathbf{k}',\downarrow} c_{\mathbf{k}',\uparrow}. \quad (1.3.2)$$

In BCS theory, the interaction term is given by the electron-phonon coupling, which results into an attractive channel between the electrons to form a pair. The resulting Cooper pair has the most symmetric form, which is the s -wave pairing with vanishing relative orbital angular momentum. For the s -wave symmetry, the spin has to be singlet to satisfy the antisymmetry condition for fermions. This is referred to conventional superconductivity. In the unconventional superconductivity, the pairing happens in lower symmetric (p -wave, d -wave etc.) forms and in the singlet or triplet channels.[39, 40, 41, 42] The mechanism of unconventional superconductor is still an open field of research and there exist many theoretical proposals. As presented in chapter 3, I am interested in a superconductivity from repulsive Coulomb interaction, which arises from spin-fluctuations.

I start with a Coulomb interaction term as

$$H_{int} = \int d\mathbf{r} d\mathbf{r}' \tilde{U} \delta(\mathbf{r} - \mathbf{r}') \rho_{\uparrow}(\mathbf{r}) \rho_{\downarrow}(\mathbf{r}'), \quad (1.3.3)$$

where \tilde{U} is the strength of repulsive contact interaction, $\rho_s(\mathbf{r}) = c_s^{\dagger}(\mathbf{r}) c_s(\mathbf{r})$ denotes the density

of electrons with spin s . Polarized electron spin acts like a local magnetic field, which is given by

$$\mathbf{B}_{eff}(\mathbf{r}, t) = -\frac{U}{\mu_B \hbar} \mathbf{S}(\mathbf{r}, t), \quad (1.3.4)$$

where $U = \tilde{U}/\Omega$ (Ω is the volume). Linear response theory can connect the electron spin and the magnetic field with the response function dynamical susceptibility χ as

$$\mathbf{S}(\mathbf{r}', t') = \mu_B \int d\mathbf{r} dt \chi(\mathbf{r}' - \mathbf{r}, t' - t) \mathbf{B}_{eff}(\mathbf{r}, t), \quad (1.3.5)$$

which results into the spin fluctuation Hamiltonian as

$$\begin{aligned} \mathcal{H}_{sf} &= -\frac{U^2}{\hbar^2} \int d\mathbf{r} d\mathbf{r}' dt dt' \chi(\mathbf{r}' - \mathbf{r}, t' - t) \mathbf{S}(\mathbf{r}, t) \mathbf{S}(\mathbf{r}', t') \\ &= -\frac{U^2}{4} \int d\omega \sum_{\mathbf{q}, \mathbf{k}, \mathbf{k}'} \text{Re} [\chi(\mathbf{q}, \omega)] \sum_{s_1, s_2, s_3, s_4} \left\{ c_{\mathbf{k}+\mathbf{q}, s_1}^\dagger \boldsymbol{\sigma}_{s_1, s_2} c_{\mathbf{k}, s_2} \right\} \cdot \left\{ c_{\mathbf{k}'-\mathbf{q}, s_3}^\dagger \boldsymbol{\sigma}_{s_3, s_4} c_{\mathbf{k}', s_4} \right\}. \end{aligned} \quad (1.3.6)$$

By following the similar procedure as the BCS Cooper pairing with vanishing linear momentum, one arrives at the pairing potential due to electron-paramagnon coupling from spin fluctuation exchange mechanism, which is given by

$$\mathcal{H}_{sf} = \sum_{\mathbf{k}, \mathbf{k}'} \sum_{s_1, s_2, s_3, s_4} V_{\mathbf{k}, \mathbf{k}'; s_1, s_2, s_3, s_4} c_{\mathbf{k}, s_1}^\dagger c_{-\mathbf{k}, s_2}^\dagger c_{-\mathbf{k}', s_3} c_{\mathbf{k}', s_4}, \quad (1.3.7)$$

where

$$V_{\mathbf{k}, \mathbf{k}'; s_1, s_2, s_3, s_4} = -\frac{U^2}{4} \text{Re} [\chi(\mathbf{q} = \mathbf{k} - \mathbf{k}', \omega = \epsilon_{\mathbf{k}} - \epsilon_{\mathbf{k}'})] \boldsymbol{\sigma}_{s_1, s_2} \cdot \boldsymbol{\sigma}_{s_3, s_4}. \quad (1.3.8)$$

The susceptibility can be split into spin and charge channels, and can be evaluated by RPA approximation by considering the diagrams as shown in Fig. 1.2(b). By summing over the diagrams, one arrives at the RPA susceptibility expression given by

$$\chi^{s/c}(\mathbf{q}, \omega) = \frac{\chi_0(\mathbf{q}, \omega)}{1 \mp U \chi_0(\mathbf{q}, \omega)}, \quad (1.3.9)$$

where $\chi^{s/c}$ represents spin/charge susceptibility, and $\chi_0(\mathbf{q}, \omega)$ is the Linhard susceptibility given by

$$\chi_0(\mathbf{q}, \omega) = - \sum_{\mathbf{k}} \frac{f(\epsilon_{\mathbf{k}}) - f(\epsilon_{\mathbf{k}+\mathbf{q}})}{\omega + i\delta - \epsilon_{\mathbf{k}} + \epsilon_{\mathbf{k}+\mathbf{q}}}. \quad (1.3.10)$$

With this definition of susceptibility and from Eq. (1.3.8), the pairing potentials for singlet and triplet channels are given by [43, 44, 45]

$$V_{\mathbf{k}, \mathbf{k}'}^{singlet} = \frac{U^2}{4} \text{Re} [3\chi^s(\mathbf{q}, \omega) - \chi^c(\mathbf{q}, \omega)], \quad (1.3.11)$$

$$V_{\mathbf{k}, \mathbf{k}'}^{triplet} = \frac{U^2}{4} \text{Re} [-\chi^s(\mathbf{q}, \omega) - \chi^c(\mathbf{q}, \omega)]. \quad (1.3.12)$$

With these pairing potentials, the generalized BCS theory can be used to solve for superconductivity. The generalized BCS Hamiltonian can be written as,

$$\mathcal{H}_{gen} = \sum_{\mathbf{k}, s} \epsilon_{\mathbf{k}} c_{\mathbf{k}s}^\dagger c_{\mathbf{k}s} + \sum_{\mathbf{k}, \mathbf{k}'} \sum_{s_1, s_2, s_3, s_4} V_{\mathbf{k}\mathbf{k}'; s_1 s_2 s_3 s_4} c_{\mathbf{k}, s_1}^\dagger c_{-\mathbf{k}, s_2}^\dagger c_{-\mathbf{k}' s_3} c_{\mathbf{k}' s_4}. \quad (1.3.13)$$

The mean-field Cooper pair field is defined as $b_{\mathbf{k}, ss'} = \langle c_{-\mathbf{k}s} c_{\mathbf{k}s'} \rangle$, and the mean field Hamiltonian becomes

$$\begin{aligned} \mathcal{H}_{gen}^{mf} &= \sum_{\mathbf{k}, s} \epsilon_{\mathbf{k}} c_{\mathbf{k}s}^\dagger c_{\mathbf{k}s} - \frac{1}{2} \sum_{\mathbf{k}, s_1, s_2} [\Delta_{\mathbf{k}, s_1 s_2} c_{\mathbf{k}, s_1}^\dagger c_{-\mathbf{k}, s_2}^\dagger + \Delta_{\mathbf{k}, s_1 s_2}^* c_{\mathbf{k}s_1} c_{-\mathbf{k}s_2}] \\ &- \frac{1}{2} \sum_{\mathbf{k}, \mathbf{k}'} \sum_{s_1, s_2, s_3, s_4} V_{\mathbf{k}\mathbf{k}'; s_1 s_2 s_3 s_4} \langle c_{\mathbf{k}, s_1}^\dagger c_{-\mathbf{k}, s_2}^\dagger \rangle \langle c_{-\mathbf{k}' s_3} c_{\mathbf{k}' s_4} \rangle + \text{small terms}, \end{aligned} \quad (1.3.14)$$

where $\Delta_{\mathbf{k}, ss'}$ is the generalized gap function defined by

$$\begin{aligned} \Delta_{\mathbf{k}, ss'} &= - \sum_{\mathbf{k}', s_3 s_4} V_{\mathbf{k}, \mathbf{k}'; ss' s_3 s_4} b_{\mathbf{k}, s_3 s_4}, \\ \Delta_{\mathbf{k}, ss'}^* &= - \sum_{\mathbf{k}', s_1 s_3} V_{\mathbf{k}', \mathbf{k}; s_1 s_2 s' s} b_{\mathbf{k}, s_1 s_2}^*. \end{aligned} \quad (1.3.15)$$

In this notation the generalized gap function is represented by a matrix in the spin basis as

$$\hat{\Delta}_{\mathbf{k}} = \begin{bmatrix} \Delta_{\mathbf{k},\uparrow\uparrow} & \Delta_{\mathbf{k},\uparrow\downarrow} \\ \Delta_{\mathbf{k},\downarrow\uparrow} & \Delta_{\mathbf{k},\downarrow\downarrow} \end{bmatrix}. \quad (1.3.16)$$

And this gap function is related to the Cooper pair wave function by Eq. (1.3.15). The gap function can be written in terms of momentum and spin parts as

$$\Delta_{\mathbf{k},ss'} = \phi(\mathbf{k})\chi_{ss'}, \quad (1.3.17)$$

where ϕ is the spatial momentum part, and χ is the spin part. Due to antisymmetry property of Fermions, the momentum and spin part are related as follows

$$\begin{aligned} \text{Even parity : } \quad \phi(-\mathbf{k}) &= \phi(\mathbf{k})\chi_{ss'} \quad (l = 0, 2..), \\ \chi_{ss'} &= \frac{1}{2}(\uparrow\downarrow - \downarrow\uparrow) \quad \text{singlet} \end{aligned} \quad (1.3.18)$$

$$\begin{aligned} \text{Odd parity : } \quad \phi(-\mathbf{k}) &= -\phi(\mathbf{k})\chi_{ss'} \quad (l = 1, 3..), \\ \chi_{ss'} &= \begin{aligned} &\uparrow\uparrow \\ &\frac{1}{2}(\uparrow\downarrow + \downarrow\uparrow) \quad \text{triplet} . \\ &\downarrow\downarrow \end{aligned} \end{aligned} \quad (1.3.19)$$

In this generalized BCS set up, conventional superconductivity of the BCS theory due to electron phonon coupling corresponds to $l = 0$ singlet s wave pairing. However, there are other unconventional s ($l = 0$) wave pairing like extended- s or s_{\pm} pairing, where pairing eigenvalues change sign on the Fermi surface. The other lower symmetry gap functions ($l = 1, 2, ..$) are considered as unconventional superconductivity. In chapter 3, I extend the formalism in Eq. (1.3.15) to a multiband case and solve for twisted bi-layer graphene.

1.4 Topology

In this section the topology in physics is introduced in a general framework of field theory. I start with the Fermionic σ -model in d ($= 1, 2$) spatial dimensions. The Lagrangian for the

model is given by[46]

$$\mathcal{L}_1 = \psi^* \left(i\hat{D} + im(\Delta_1 + i\gamma_5\Delta_2) \right) \psi \quad \text{for } (1+1) \text{ dim,} \quad (1.4.1)$$

$$\mathcal{L}_2 = \psi^* \left(i\hat{D} + im\mathbf{n}\cdot\boldsymbol{\tau} \right) \psi \quad \text{for } (2+1) \text{ dim,} \quad (1.4.2)$$

where ψ represents a Dirac fermion, $\hat{D} = \gamma_\mu(\partial_\mu - iA_\mu)$, A_μ is the abelian gauge field, γ_μ s are γ -matrices, and τ_μ s are Pauli matrices. Further, a positive value of mass ($m > 0$) is assumed. The chiral fields (Δ_i) introduced in the above equations for $d = 1$ can be written as a phase $\Delta_1 + i\Delta_2 = e^{i\phi}$, and for $d = 2$, it is a unit vector $\mathbf{n} = (n_1, n_2, n_3)$. The topological charge for the system can be written as a spatial integral $Q = \int d^d x J_0$, where J_0 is the zeroth component of the topological current in $(d + 1)$ dimension, which is given by[46]

$$(1+1): \quad J_\mu = \frac{1}{2\pi} \epsilon_{\mu\nu} \partial_{\nu\alpha} \phi, \quad (1.4.3)$$

$$(2+1): \quad J_\mu = \frac{1}{8\pi} \epsilon_{\mu\nu\lambda} \mathbf{n} \cdot \partial_\nu \mathbf{n} \times \partial_\lambda \mathbf{n}. \quad (1.4.4)$$

From the above equations the zeroth component can be written as

$$(1+1): \quad J_0 = \frac{\partial\phi}{\partial x}, \quad (1.4.5)$$

$$\begin{aligned} (2+1): \quad J_0 &= \frac{1}{8\pi} \mathbf{n} \cdot \left(\frac{\partial\mathbf{n}}{\partial x} \times \frac{\partial\mathbf{n}}{\partial y} - \frac{\partial\mathbf{n}}{\partial y} \times \frac{\partial\mathbf{n}}{\partial x} \right) \\ &= \frac{1}{4\pi} \mathbf{n} \cdot \frac{\partial\mathbf{n}}{\partial x} \times \frac{\partial\mathbf{n}}{\partial y}. \end{aligned} \quad (1.4.6)$$

For $d = 1$, Q can be associated with winding number in 1D system and for $d = 2$, Q can be associated with the topological invariant of the system like Chern number for topological insulators or skyrmion number for topological spin-texture. In the following sections, various topological concepts and their physical origins are briefly described for electronic structure (topological insulators) and spin systems (magnetic skyrmions). These concepts will be useful in Chapter 4 and 5, where skyrmions and topological insulators in the bi-layer systems are described.

1.4.1 Berry Phase and Chern number

Quantum mechanical wavefunction can be changed under a $U(1)$ transformation $|\psi\rangle = e^{i\phi}|\psi\rangle$ without changing its properties. Such an ambiguity of phase does not appear in the expectation values of the observables. In case of a lattice, the quantum mechanical states are represented by the Bloch states, and similar phase ambiguity appears $|u_{\mathbf{k}}\rangle \rightarrow e^{i\phi}|u_{\mathbf{k}}\rangle$, where \mathbf{k} is the crystal momentum and u has the periodicity of the reciprocal lattice vector $u_{\mathbf{k}+\mathbf{G}} = u_{\mathbf{k}}$. If ϕ is independent of \mathbf{k} , then the phase does not appear in defining various properties. But such a global gauge can not always be defined in the entire Brillouin zone. Therefore, one needs to use a \mathbf{k} -dependent gauge transformation as

$$|u_{\mathbf{k}}\rangle \rightarrow e^{i\phi(\mathbf{k})}|u_{\mathbf{k}}\rangle. \quad (1.4.7)$$

But such a local gauge transformation in the momentum space requires a gauge field to make the derivative term in the Hamiltonian to be gauge invariant. This is called the Berry connection[47] as defined by

$$\mathbf{A}_{\mathbf{k}} = -i\langle u_{\mathbf{k}}|\nabla_{\mathbf{k}}|u_{\mathbf{k}}\rangle. \quad (1.4.8)$$

Under the gauge transformation of Eq. (1.4.7), the Berry connection changes as $\mathbf{A}_{\mathbf{k}} \rightarrow \mathbf{A}_{\mathbf{k}} + \nabla_{\mathbf{k}}\phi(\mathbf{k})$, which is analogous to the electromagnetic vector potential. By following the analogy further, the gauge invariant Berry phase can be defined as

$$\gamma_C = \oint_C \mathbf{A} \cdot d\mathbf{k} = \int_S \mathcal{F} d\mathbf{k}, \quad (1.4.9)$$

where the first integration is along a closed loop C , and the second one is a surface integration in \mathbf{k} -space, and \mathcal{F} is the Berry curvature defined as $\mathcal{F} = \nabla \times \mathbf{A}$.

To explore a simple physical meaning to the Berry phase, I consider a Hamiltonian of the form $H(\mathbf{k}) = \mathbf{d}(\mathbf{k}) \cdot \boldsymbol{\sigma}$, where $\boldsymbol{\sigma}$ denotes Pauli spin matrices. Berry phase for such a Hamiltonian along a closed loop C in \mathbf{k} -space is the solid angle covered by $\hat{\mathbf{d}}(\mathbf{k})$ as \mathbf{k} goes around the loop. Then the Berry curvature is interpreted as the solid angle per unit area in the

\mathbf{k} -space, which is given by

$$\mathcal{F} = \frac{1}{2}\epsilon_{ij}\hat{\mathbf{d}}\cdot(\partial_i\hat{\mathbf{d}}\times\partial_j\hat{\mathbf{d}}). \quad (1.4.10)$$

And when \mathcal{F} is integrated over the Brillouin zone, we can count the number of times $\hat{\mathbf{d}}$ wraps around the unit sphere created by it. This is denoted by the Chern number[48, 49] given by

$$n = \frac{1}{2\pi} \int_S \mathcal{F} d\mathbf{k}, \quad (1.4.11)$$

which serves as the topological invariant of the system. More physical insights into the Chern invariant can be gained from considering Thouless charge pump.[50, 51]

1.4.2 Thouless charge pump and bulk boundary correspondence

Berry phase can be connected to the polarization of the band structure. To illustrate the idea, let us consider 1D system for which polarization can be given by

$$P = \frac{e}{2\pi} \oint_{BZ} A(k) dk. \quad (1.4.12)$$

In 1D the above expression is not gauge invariant, because a gauge transformation $|u_k\rangle \rightarrow e^{i\phi(k)}|u_k\rangle$ (or equivalently $\mathbf{A}_k \rightarrow \mathbf{A}_k + \nabla_k\phi(\mathbf{k})$) will change the polarization as $P \rightarrow P + ne$ (note that $\phi(\pi/a) - \phi(-\pi/a) = 2\pi n$). To remove the gauge dependence, I consider a Hamiltonian with a tuning parameter t such that when $t = T$ the system comes back to the initial state; Or in other words the Hamiltonian is periodic in $t : H(k, t + T) = H(k, t)$. Now the change in polarization can be shown to be gauge independent as

$$\begin{aligned} \Delta P &= P(t = T) - P(t = 0) \\ &= \frac{e}{2\pi} \left[\oint_{C_{t=T}} - \oint_{C_{t=0}} \right] A(k).dk \\ &= \frac{e}{2\pi} \int_S \mathcal{F} dk dt = ne. \end{aligned} \quad (1.4.13)$$

In the above equation, the line integral is taken in two dimensional space spanned by k and t . At every cycle, n number of electrons are transported from one edge to the other, even if there

is a bulk band gap. In this manner, the polarization which is a phenomena at the boundary can be connected to the Chern number which is a bulk property. In 1D P is called Zack phase. In case of a finite size 2D system, similar argument can show the appearance of the conducting edge states when $n \neq 0$. [52] These edge states have interesting properties. Since these states depend only on the topology of the system they are robust against disorder, and they are chiral since they propagate only in one direction. Although the number of these edge states (N_R for right moving states, N_L for left moving states) is not fixed, the difference between the number of right moving and left moving states is fixed, and is connected to the Chern number as

$$N_R - N_L = \Delta n, \quad (1.4.14)$$

where Δn is the difference in Chern numbers of the two systems across the boundary.

1.4.3 Z_2 topological invariant

If the system has time reversal symmetry, then the total Chern number vanishes. But a new topological invariant can be defined, which takes two values of Z_2 , and such systems are called Z_2 topological insulators. [53, 54] The time reversal operator is an antiunitary operator given by $\Theta = e^{i\pi S_y/\hbar} K$, where S_y is the spin operator, and K is the complex conjugation operator. Θ has the interesting property that $\Theta^2 = -1$ for spin $\frac{1}{2}$ systems. If a Hamiltonian is time reversal (\mathcal{T}) invariant, then it should follow Kramer's theorem, which states that if \mathcal{T} symmetry is maintained, all eigenstates of the Hamiltonian are at least twofold degenerate (For spin 1/2 it is twofold, and for other half-integer spin, degeneracy can be twofold or more). In a system, where spin-orbit coupling (SOC) is absent, Kramer's degeneracy is the degeneracy between up and down spins. And if SOC is present, then spin is no longer a good quantum number, but the same conclusions can be drawn in some other basis, which is called helical basis. At the high symmetry \mathbf{k} points in the BZ, \mathbf{k} point coincides with its \mathcal{T} partner, which is $-\mathbf{k}$. These are called \mathcal{T} invariant momentum points. For example, in 1D, there are two such \mathbf{k} points ($k = 0, \pi/a$) in the half BZ. Only the half BZ is considered because the other half should be symmetric due to the \mathcal{T} symmetry. In 2D square lattice, there are four such points ($(k_x, k_y) = (0, 0), (\pi/a, 0), (0, -\pi/a), (0, \pi/a)$), and in 3D cubic lattice, there are eight such

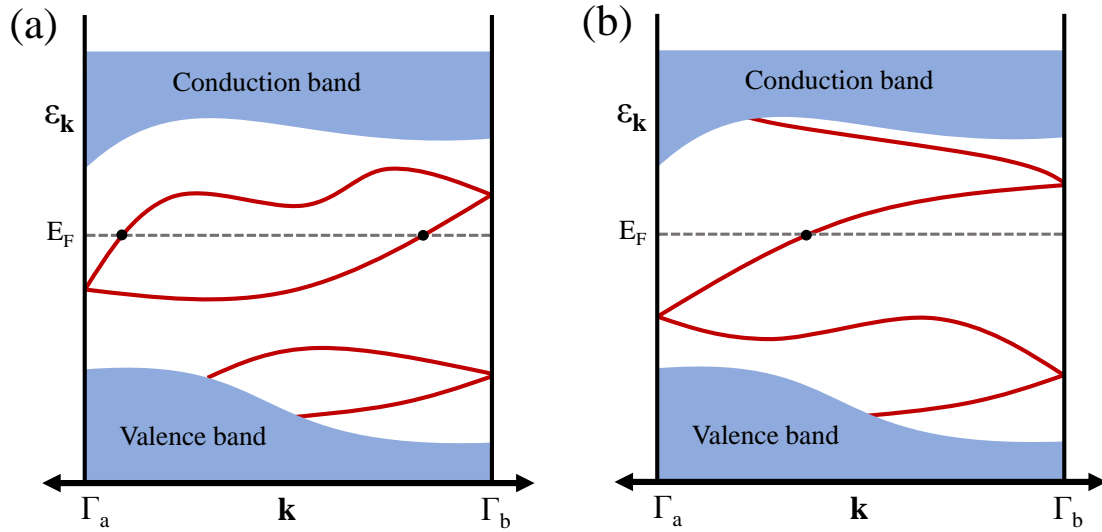


Figure 1.3: Two different types of edge states with Kramer's degeneracy - (a) the edge states, crossing the Fermi energy, are not connected to the valence or conduction bands, and have even number of crossings at the Fermi energy leading to topologically trivial state; (b) The edge states are connected to the valence and conduction bands with odd number of crossings at the Fermi energy leading to topologically non-trivial state.

points and so on. The \mathcal{T} invariant Hamiltonian satisfies the relation $\Theta H(\mathbf{k})\Theta^{-1} = H(-\mathbf{k})$, and has Kramer's degeneracy of the edge states at the \mathcal{T} invariant momentum points. Away from \mathcal{T} invariant momentum points, if the Hamiltonian has SOC, the degeneracy is lifted. With this picture in mind, it is possible to argue that there can be only two values of the topological invariant for such systems.

Let us consider a \mathcal{T} symmetric 2D system with periodic boundary condition in one directions (x direction) and edges in the other direction (y direction). If this system is topologically nontrivial, it should have gapless edge states. Since k_x is a good quantum number in this system, half of the BZ is taken in the k_x direction $0 < k_x < \pi/a$. Two \mathcal{T} -invariant \mathbf{k} points $k_x = 0$ and $k_x = \pi/a$ have degeneracies, which can be fulfilled in two ways as shown in Fig. 1.3(a) and (b).[55] This is a generic bandstructure with Kramer's degeneracy, which consists of bulk bands which are gapped and the edge states are metallic. In Fig. 1.3(a), the edge states maintain the degeneracies in a way that they do not connect to the valence and conduction bulk bands. With disorder, such edge states can be moved so that it does not cross the Fermi level, and thus has a trivial topological property (topological index $\nu = 0$). On the other hand, Fig. 1.3(b) shows the edge states, which connect the valence and conduction bulk bands, and cross the

Fermi level, which cannot be removed by disorder. This has non-trivial topology ($\nu = 1$). In general, if there are N_K number of points, where Kramer's pair cross the Fermi level in the half BZ, then the topological index is given by[56]

$$\nu = \text{mod}(N_K, 2). \quad (1.4.15)$$

If the full BZ is considered, then there are always even number of edge states. For example, where the z -direction of spin is conserved, the sum of the Chern numbers for both up and down spins is zero; but their difference gives a nonzero value, and topological invariant is given by $\nu = \text{mod}((n_\uparrow - n_\downarrow)/2, 2)$. For more general formulation of Z_2 invariant, Bloch functions can be used to define a unitary matrix[57]

$$w_{mn} = \langle u_m(\mathbf{k}) | \Theta | u_n(-\mathbf{k}) \rangle, \quad (1.4.16)$$

where the indices m and n run over occupied bands. At the \mathcal{T} -invariant points Γ_a , the w matrix is antisymmetric, and one can define

$$\delta_a = \frac{\text{Pf}[w(\Gamma_a)]}{\sqrt{\det[w(\Gamma_a)]}} = \pm 1. \quad (1.4.17)$$

Thus, δ_a can be defined in each \mathcal{T} -invariant \mathbf{k} point. Since there is a gauge ambiguity in defining eigenvectors $|u_n(\mathbf{k})\rangle$, the gauge must be chosen continuously in the whole BZ, which is always possible for Z_2 topological insulators, because the total Chern number of occupied bands is zero in these systems. There are various numerical methods like parallel transport of eigenvectors, Wannier function method, Wilson loop method to define a continuous Bloch wavefunctions. The Z_2 invariant, ν , is given by[57, 55]

$$(-1)^\nu = \prod_{a=1}^n \delta_a, \quad (1.4.18)$$

where n is the total number of \mathcal{T} invariant \mathbf{k} points in the half BZ.

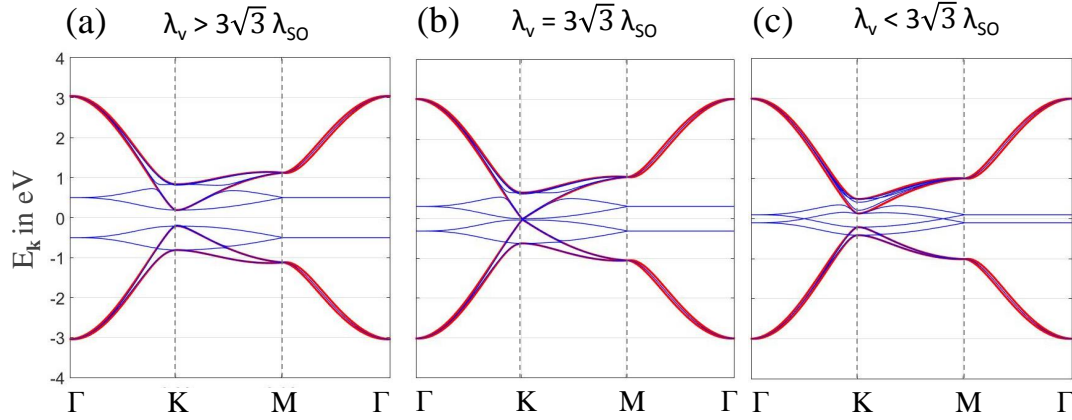


Figure 1.4: Band structure (red) and zeros of Green's function (blue) for Kane-Mele model[54] with three steps of staggered potential λ_v and spin orbit coupling strength λ_{SO} - (a) for $\lambda_v > 3\sqrt{3}\lambda_{SO}$, zeros of Green's function does not cross in the band gap region, giving a topological trivial state, (b) $\lambda_v = 3\sqrt{3}\lambda_{SO}$ is the transition point, where zeros of Green's function just cross in the band gap region, giving a topological non-trivial state, and (c) for $\lambda_v < 3\sqrt{3}\lambda_{SO}$ zeros of Green's function cross in the band gap region, giving a topological non-trivial state.

1.4.4 Green's function method to detect topological insulators

A recent study by Misawa and Yamaji showed that the Green's functions can be used to detect the topological non-trivial states in 2D and 3D.[58] Other methods mentioned above require the knowledge of the eigenvectors and are numerically expensive for large Hamiltonians. For multiband systems, the Green's function is a matrix in band basis $G_{mn}(\mathbf{k}, \omega)$, with m and n representing band index. Green's function method considers only the diagonal component of the Green's function $G_n(\mathbf{k}, \omega)$ for $m = n$. Zeros of the diagonal component of the Green's function cross each other in the band gap region for topological insulators (see Fig. 1.4(c)), and the crosses are guaranteed by the existence of gapless edgestates. Diagonal component of Green's function, expressed in terms of Bloch wavefunctions is given by

$$G_n(\mathbf{k}, \omega) = (\omega I - H(\mathbf{k}))_{nn}^{-1} = \sum_{i=1}^N \frac{|u_i^{(n)}(\mathbf{k})|^2}{\omega - E_i(\mathbf{k})}, \quad (1.4.19)$$

where $E_i(\mathbf{k})$ is the i th eigenvalue of the Hamiltonian $H(\mathbf{k})$, and $u_i^n(\mathbf{k})$ is the n th component of the i th eigenvector, and N is the rank of the Hamiltonian matrix. It can be shown that the n th

component can be written in terms of eigenvalues of the Hamiltonian and the minor matrix as

$$\begin{aligned}
 G_n(\mathbf{k}, \omega) &= \sum_{i=1}^N \frac{\det(\omega \mathbf{I}_{N-1} - M_n(\mathbf{k}))}{\det(\omega \mathbf{I}_N - H(\mathbf{k}))} \\
 &= \frac{\prod_{i=1}^N [\omega - E_i(M_n(\mathbf{k}))]}{\prod_{i=1}^N [\omega - E_i(H(\mathbf{k}))]}, \tag{1.4.20}
 \end{aligned}$$

where $E_i(A)$ denotes the i th eigenvalue of matrix A , and M_n is the minor matrix created by removing n th row and n th column from H . From the above equation, it can be seen that the zeros of Green's function can be determined from the eigenvalues of the minor matrices, and the poles of the Green's function are the eigenvalues of the Hamiltonian. The poles will give the bulk band structure, and if the zeros are plotted along with the bulk bands, there will be crossing of zeros in the band gap energy region (see Fig. 1.4) for a topological insulator. The number of crosses of zeros is gauge invariant. Further it can be shown that the m -fold degeneracy in the edge states implies m -fold degeneracy in the zeros of bulk Green's function, which crosses in the band gap region. Thus the edge states induce the crosses of zeros of the Green's function.

1.4.5 Topology in spin texture

Topology in $O(3)$ spin system in 2D can be described by a skyrmion number. The concept of skyrmions was originally proposed by Skyrme in the context of high energy physics.[59] In quantum field theory, particles are described by the excitations of the fields. Hence, the stability of particles is very difficult to explain by considering energy. According to Skyrme, the particles are stable due to topological protection, which is characterized by some topological invariant (integer number). This cannot be changed by a continuous deformation of the field. Thus, skyrmions can be viewed as a topologically stable field configuration. Apart from high energy physics, it also appears in condensed matter systems in various fields like quantum Hall system[60], liquid crystal[61], Bose condensate[62]. In 2D chiral magnets, the local magnetization can play the role of fields, and the skyrmions can be described by the spin texture of the system.[63, 64] These are called magnetic skyrmions, which will be the topic of discussion in chapter 4 of this thesis. A magnetic skyrmion can be characterized by an integer

winding number also called the skyrmion number, which is given by[65, 66]

$$Q = \int \frac{dxdy}{4\pi} \mathbf{n} \cdot \frac{\partial \mathbf{n}}{\partial x} \times \frac{\partial \mathbf{n}}{\partial y}. \quad (1.4.21)$$

Here $\mathbf{n}(x, y)$ denotes the field configuration of unit magnitude ($|\mathbf{n}(x, y)| = 1$). Depending on the values of Q , the spin texture can be categorized in different classes like bi-skyrmion ($Q = -2$), skyrmion ($Q = -1$), meron ($Q = -0.5$). Here, we assume that the magnetization or spin orientation at the core center is negative. For the same magnetization direction at the core center, there can be topological structure like antiskyrmion $Q = 1$ or antimeron $Q = 0.5$. For core magnetization with opposite direction, all the topological numbers change sign. Apart from these structures, there can also be combinations of them, e.g., a bimeron ($Q = -1$) consisting of a meron with $Q = -0.5$ and an antimeron with $Q = -0.5$.

There can be distinct skyrmion types with the same topological charge Q . Degenerate skyrmion solutions can exist with different in-plane spin-orientation. This can be distinguished with additional quantities - vorticity number Q_v , and helicity number Q_h . [66, 67] To extract these numbers, we use the polar co-ordinates $\mathbf{r} = (r \cos \phi, r \sin \phi)$. The symmetry of skyrmionic structure permits us to write $\mathbf{n}(\mathbf{r})$ in terms of polar angles as[68]

$$\mathbf{n}(\mathbf{r}) = (\cos \Phi(\phi) \sin \Theta(r), \sin \Phi(\phi) \sin \Theta(r), \cos \Theta(r)), \quad (1.4.22)$$

where Φ depends only on ϕ , and Θ depends only on r because of symmetry of skyrmionic structure. The skyrmion number can now be written as $Q = [\cos \Theta(r)]_{r=0}^{r=\infty} [\cos \Phi(\phi)]_{\phi=0}^{\phi=2\pi}$. Assuming a spin down state at the core center $r = 0$, and spin up at $r \rightarrow \infty$, we have $[\cos \Theta(r)]_{r=0}^{r=\infty} = 2$. Then vorticity Q_v can be defined by the nature of in-plane orientation of the spins, which is given by

$$Q_v = \frac{[\cos \Phi(\phi)]_{\phi=0}^{\phi=2\pi}}{2\pi}. \quad (1.4.23)$$

The helicity Q_h can be defined as a phase, as given by

$$\Phi(\phi) = Q_v \phi + Q_h. \quad (1.4.24)$$

These three numbers (Q, Q_v, Q_h) completely categorizes skyrmionic structure. There are mainly two types of skyrmion depending on the in-plane spin orientation - Bloch skyrmion ($Q_h = -\pi/2$ or $\pi/2$), and Néel skyrmion ($Q_h = 0$ or π).

Magnetic skyrmions were first observed in MnSi in the presence of an external magnetic field.[69] The observed spin structure indicates the formation of a lattice, which consists of two-dimensional skyrmions. The periodicity of skyrmionic lattice defines a new magnetic unit cell, determined by some long-ranged interactions like dipole, or by some chiral interaction like Dzyaloshinskii Moriya interaction (DMI). There have been intense theoretical and experimental studies of skyrmions in 2D lattices and thin films. Magnetic skyrmion often appears as a spin configuration allowed by classical solution of the non-linear sigma model. However, the main challenge lies in stabilizing a skyrmion solution at a saddle-point energy minimum, requiring distinct magnetic interactions and frustration. Long-range dipole-dipole interaction, in addition to easy-plane magnetic anisotropy and magnetic field, was initially proposed to mediate skyrmion solution.[70] DMI brings in the chiral spin-spin interaction required for a skyrmion solution [71, 72, 73, 74, 75, 76] and favours coplanar structure. On the other hand, the ferromagnetic exchange interaction favours spin alignment in z direction. But presence of both DMI and ferromagnetic exchange interactions makes a spatially varying magnetic texture to have a lower energy than the mean-field long-range magnetic order. Geometrical and magnetic frustration can also stabilize skyrmion structures [77, 78, 79, 80]. This is induced, for example, in a triangular lattice by the competition between a ferromagnetic nearest neighbour (NN) exchange with an antiferromagnetic next nearest neighbour (NNN) interaction. Apart from these, more recently, spin-orbit coupling[81], Kondo coupling[82], and magnetic disorder with the application of magnetic pulse [83] are shown to assist skyrmion solution. Proposals to obtain skyrmions via quantum Hall substrates[84] and optical lattices[85] are also presented.

In chapter 4, I'll return to this topic where we describe more details of skyrmions in thin films of Van der Waals (VdW) magnets and explore the formation of exotic skyrmionic phases in twisted bilayer geometry.

1.5 Moiré pattern and twisted bi-layer

Recent development has made it possible to construct bi-layer lattice. Physics in bi-layer systems sometimes are markedly different from the original 2D lattice. For example, in single layer graphene, the band dispersion shows a linear behaviour near the Dirac point in the momentum space; whereas bilayer graphene with Bernal stacking shows quadratic dispersion.[86] There are also various other possibilities to construct a bilayer depending on the stacking (AA stacking, AA_{1/3} stacking) of the lattice points between two layers, which also influence the inter-layer tunneling. Interlayer tunneling plays an important role in bilayer systems. In fact, many interesting physics can be interpreted as a result of the inter-layer tunneling. In case of magnetic bi-layer, both layers are connected by the weak Van der Waals force. Therefore, magnetic interactions between them is very weak. But even such weak magnetic interaction can change the properties of the system considerably. For example, bulk CrI₃ shows ferromagnetic behaviour whereas a bilayer (AA stacking) of CrI₃ shows the ferromagnetic spin alignment in each layers, and antiferromagnetic spin alignment between the layers.[87] Interlayer tunneling becomes even more interesting, if the stacking is position dependent; or in other words, as we move from one position to other the nature of the stacking changes. Such things happen if there is a mismatch between the two layers, and this gives rise to the Moiré pattern.

Moiré pattern in bi-layer system can arise in two different ways - by lattice mismatch δ , or by a relative twist angle θ between the layers, or by the combined effect of both.[88] Let us assume two layers of hexagonal lattice with lattice constant a^1 and a^2 (for layer 1 and layer 2[see Fig. 1.5]), and their lattice vectors are oriented in the same direction. Mismatch between a^1 and a^2 is given by $1 + \delta = a^1/a^2$, with the assumption $a^1 > a^2$. If the relative rotation between layer 1 and layer 2 is θ , then the relation between lattice vectors are given by

$$\begin{aligned} \mathbf{a}_i^1 &= M R \mathbf{a}_i^2, \\ \mathbf{a}_i^2 &= R^{-1} M^{-1} \mathbf{a}_i^1, \end{aligned} \quad (1.5.1)$$

where $M = (1 + \delta)I$, and R is the rotation matrix with angle θ , and I is the identity matrix. The displacement vectors between \mathbf{a}^1 and \mathbf{a}^2 is $\Delta(\mathbf{a}_i^1) = \mathbf{a}^1 - \mathbf{a}_i^2 = (I - R^{-1}M^{-1})\mathbf{a}_i^1$. At the Moiré lattice vector \mathbf{a}_i^m , the displacement vector must coincide with \mathbf{a}_i^2 ($\Delta(\mathbf{a}_i^m) = \mathbf{a}_i^2$) and we

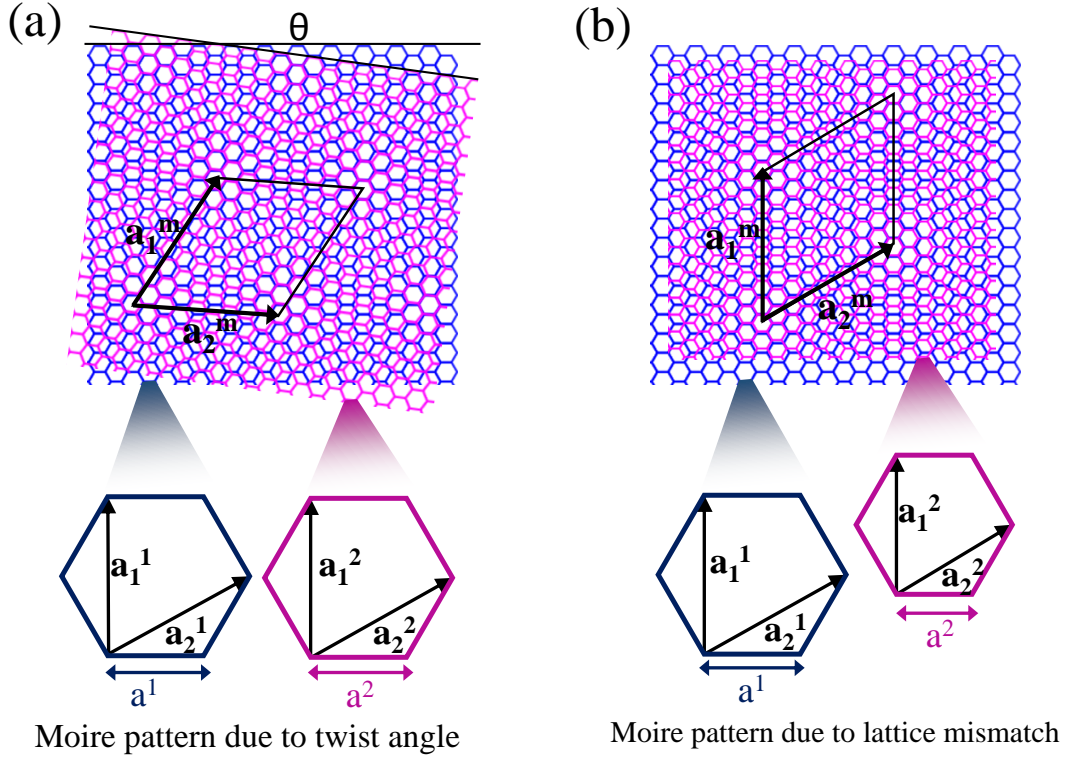


Figure 1.5: Bi-layer Moiré pattern created (a) by twist between the layers with twist angle θ , and (b) by lattice mismatch between the layers. For both cases, unit cells of single layer are shown at the bottom (blue for bottom layer, magenta for top layer).

obtain

$$\mathbf{a}_i^m = (I - R^{-1}M^{-1})^{-1}\mathbf{a}_i^2. \quad (1.5.2)$$

The reciprocal lattice vector is given by

$$\mathbf{b}_i^m = (I - M^{-1}R)\mathbf{b}_i^2, \quad (1.5.3)$$

where \mathbf{b}_i^l is the i -th reciprocal lattice vector of layer l . The length of the Moiré lattice vector $a^m = |\mathbf{a}_i^m|$ is given by

$$a^m = \frac{1 + \delta}{\sqrt{\delta^2 + 2(1 + \delta)(1 - \cos \theta)}}a^2, \quad (1.5.4)$$

and the angle between \mathbf{a}_i^2 and \mathbf{a}_i^m is given by

$$\phi = \tan^{-1} \left(\frac{-\sin \theta}{1 + \delta - \cos \theta} \right). \quad (1.5.5)$$

When there is no twist, we set $\theta = 0$ and if there is no mismatch, we set $\delta = 0$. Below we discuss both the cases separately.

If there is mismatch δ between the lattice constants a^1 and a^2 of the two layers without any twist, then the lattice constant of the Moiré pattern is given by $a^m = (1 + 1/\delta)a^2$. In defining the Moiré lattice constant this way, one must assume $\delta \ll 1$. It is evident that the Moiré lattice consists of many lattice points of the original 2D lattices, and as δ becomes smaller, a_m becomes larger, and more 2D lattice points are added, which eventually lead to the continuum limit as $\delta \rightarrow 0$.

If there is no mismatch of lattice constants (a denotes the lattice constant of the 2D lattice), for a small twist angle θ , the Moiré lattice constant is given by

$$a^m = \frac{a}{2 \sin \frac{\theta}{2}}. \quad (1.5.6)$$

There are some values of the angle θ , for which commensurancy occurs, which is given by

$$\cos \theta = \frac{3p^2 + 3pq + \frac{q^2}{2}}{3p^2 + 3pq + q^2}, \quad (1.5.7)$$

where p and q are coprime integers. Although commensurate angles appear at small as well as large angles (from 0 to $\pi/3$) the formula for a^m holds for small angles, and as θ becomes small the number of commensurate angles increases, and for $\theta \rightarrow 0$, one approaches the continuum limit.

Fig. 1.5 shows the formation of Moiré pattern in a 2D hexagonal bilayer. \mathbf{a}_1 , and \mathbf{a}_2 denote lattice vectors of the single layer hexagonal lattice. When two such layers are brought on top of each other and are given a twist of angle θ , the magnitude of the lattice vector of the Moiré superlattice is given by $a_i^m \approx a_i/\theta$, and \mathbf{a}_i^m is perpendicular to \mathbf{a}_i (see Fig. 1.5(a)). So one can

write

$$\mathbf{a}_i^m = \frac{1}{\theta} \hat{z} \times \mathbf{a}_i. \quad (1.5.8)$$

In a similar manner, we can connect the reciprocal lattice vectors of the 2D hexagonal lattice, and the reciprocal vector of the Moiré super lattice and is given by

$$\mathbf{b}_i^m = \theta \hat{z} \times \mathbf{b}_i. \quad (1.5.9)$$

Note that the prefactor here is θ instead of $1/\theta$, which indicates that a large super lattice implies a small BZ. In Fig. 1.5(a), we can see that different region of the Moiré super lattice have different stackings (AA,AB or BA). Such variations in stacking give rise to nontrivial inter-layer tunneling for electronic structure,[89] and nontrivial magnetic coupling for spin systems.[90, 91] We briefly discuss both of these aspects.

Band structure of twisted bi-layer graphene (TBG) has been studied earlier by Mcdonald and his group.[89] After the recent discovery of superconductivity in TBG,[92] the field is explored in great details, and there are many papers on various aspects in recent years.[93] One of the most interesting properties is the emergence of flat bands at some specific twist angles, called the magic angles. Flat bands imply a large density of states (DOS) at the flat band energy, because $\text{DOS} \propto 1/\nabla\epsilon_{\mathbf{k}}$. And since the band velocity $\propto \nabla\epsilon_{\mathbf{k}}$, velocity is very small. This means that electrons move slowly in a densely populated region and such electron's motion is influenced by the other ones. In other words, their motions are correlated. Such a strongly correlated physics is interesting in its own right. And in TBG, it is mostly caused by the interlayer interaction in twisted geometry because its properties are markedly different from the original graphene. The superconducting phase diagram in TBG has similarities with the famous cuprate phase diagram. In addition, tunability is very high in TBG. As a result, it is possible to tune different parameters to explore the phase diagram experimentally and thereby unravel the mysteries of superconductivity, specially unconventional superconductivity as in cuprate. There are also many studies about the phonon mediated superconductivity in twisted bi-layer systems.[94] Topological band structure is also being studied in Moiré pattern in TBG and bilayer dichalcogenides.[95]

Apart from electronic structure, spin texture is also interesting in Moiré patterns. For different nature of stacking in different region, the spin-spin interaction may vary. One DFT study indeed showed that the inter-layer coupling may be ferromagnetic or antiferromagnetic depending on AB or AA stacking in bilayer hexagonal lattice.[90] Such a position dependent exchange coupling can be expressed as $\Phi(\mathbf{x}, \mathbf{x}')$, where \mathbf{x} and \mathbf{x}' denote position vectors in the top and bottom layers respectively. However, in continuous model (small twist angle), the position vector in a Moiré unit cell can be expressed by a single variable \mathbf{x} for both the layers and the classical energy density can be written as[91]

$$\mathcal{H}_{cl} = -J'\Phi(\mathbf{x})\mathbf{M}_1 \cdot \mathbf{M}_2, \quad (1.5.10)$$

where J' is a constant, $\Phi(\mathbf{x})$ is the spatial modulation of the exchange coupling, and \mathbf{M}_1 , \mathbf{M}_2 are the order parameter (local magnetization) of the 2D layer spins. By considering the symmetry of the Moiré super lattice, $\Phi(\mathbf{x})$ can be written as

$$\Phi(\mathbf{x}) = \Phi_0 + \sum_{\mathbf{q} \neq \mathbf{0}} e^{i\mathbf{q}^m \cdot \mathbf{x}}, \quad (1.5.11)$$

where \mathbf{q}^m s are the rescaled Moiré reciprocal lattice vectors ($q^m = b^m$). For a simple case, only first harmonics are present and the space modulation part is given by

$$\Phi(\mathbf{x}) = \Phi_0 + \sum_{i=1}^3 \cos(\mathbf{b}_i^m \cdot \mathbf{x}), \quad (1.5.12)$$

where only first three reciprocal lattice vectors are present. In chapter 4, I'll discuss Ferromagnetic bilayers with such a simple interlayer coupling, which leads to many interesting spin-texture in twisted bilayer systems.

Chapter 2

Co-existence of Fermi liquid and non-Fermi liquid

2.1 Introduction

In the previous chapter, Fermi liquid (FL) and non-Fermi liquid (NFL) theories were described along with various models that give rise to non-Fermi liquid behaviors. In the cuprate materials ($\text{La}_{2-x}\text{Sr}_x\text{CuO}_4$, $\text{YBa}_2\text{Cu}_3\text{O}_{7-x}$ etc.), the development of NFL phase in the optimal doping region, as shown in Fig. 2.1, is studied extensively.[96, 97, 98, 99, 100, 101, 102] The superconducting phase diagram (see Fig. 2.1) indicates the NFL region dissects the phase diagram between an ordered phase and the FL state and the superconducting optimum transition temperature (T_c) occurs in the NFL region. Interestingly, the temperature exponent of resistivity n decreases smoothly from $n = 2$ at the FL region to $n = 1$ at the NFL region and T_c increases as n decreases. Such a change in resistivity (ρ)-temperature (T) dependence between FL and NFL system is also reflected in the frequency (ω) dependence of the imaginary part of the self-energy (Σ'') which goes as ω^2 for FL and ω for marginal Fermi liquid (MFL). Simplified picture provides a direct correspondence between the two behavior by assuming that the scattering rate (τ) for resistivity solely comes from its finite-lifetime (τ) feature as $\tau^{-1} \propto \Sigma''$. Applying the scaling analysis at low-temperatures, we find that a FL transport behavior implies long-lived, coherent quasiparticles ($\tau^{-1} \rightarrow \omega^2 \sim T^2$), while the NFL resistivity means incoherent many-body states ($\tau^{-1} \rightarrow \omega \sim T$). [103, 104, 105, 106, 107, 108, 109, 110, 111]

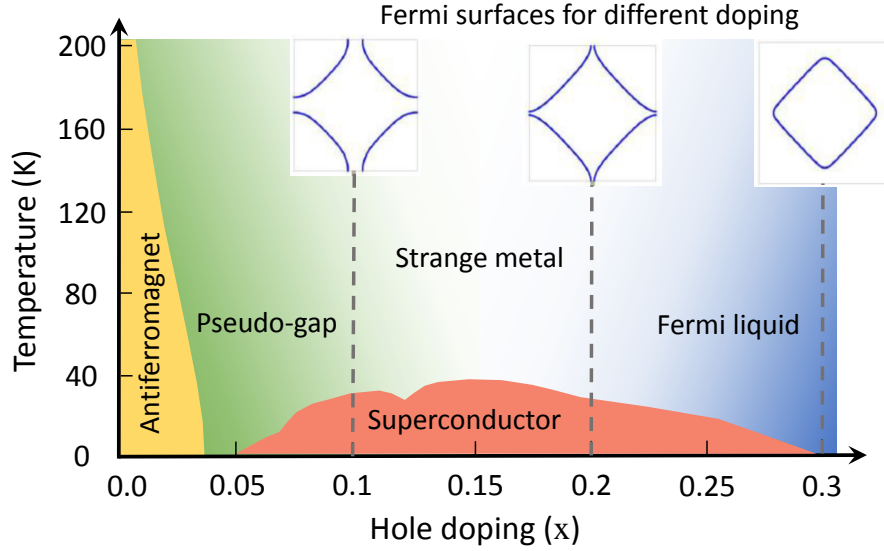


Figure 2.1: Schematic phase diagram of LSCO, showing the evolution of the Fermi surface across the NFL state and superconductivity. Around $x \sim 0.2$, the topological Fermi surface transition occurs where the VHS crosses the Fermi level, and the corresponding resistivity exponent becomes also minimum.

Such a one-to-one mapping fails to explain several experimental features in cuprates as well as in other correlated materials. For example, it is observed that the transition from the NFL to FL state is smooth, i.e., at a given temperature, the resistivity exponent n changes *continuously* from 2 to 1 or even below 1 with doping, pressure etc.[112, 113, 101, 106, 114, 115, 116, 117, 118] It also does not explain strong k -dependence of the self-energy which is observed in an angle-resolved photoemission spectroscopy (ARPES) experiment in La-based cuprate.[119] It was found that in overdoped LSCO, as we move from the nodal to antinodal region, the inverse of the quasiparticle lifetime τ^{-1} changes from ω^2 - to ω -dependence. Moreover, the linear ω -dependence, which is reminiscent of NFL self-energy, persists to the overdoped sample where the transport data suggest a simple FL behavior. Again, angle-dependent magnetoresistance (ADMR) measurements on overdoped TI-based cuprate also exhibited the similar behavior in that the scattering rate changes from T^2 to T behavior as we move from the nodal to the antinodal region at the same doping.[120, 121] In addition, it is also observed that the FS is coherent in both NFL (optimal doping) and FL (over doping) states. Recently, coexisting NFL and FL state is also observed in a heavy-fermion system.[122] Therefore, the leading questions concerning the mechanism of the NFL state near the optimal doping, the analytic behavior of

the self-energy in the entire k -space and doping, smooth crossover with a wide region of the coexistence of the NFL and FL states in both spectroscopic and transport properties have so-far remained open.

The main objective of this chapter is to answer the above questions and to explain the FL and NFL behavior in a single self-consistent theoretical framework and describe the coexistence of FL and NFL self energies at all doping in Cuprates.

2.2 Momentum anisotropy in self energy

To capture the strong momentum anisotropy in selfenergy, momentum resolved density fluctuation (MRDF) model is employed, which uses RPA and fluctuation-exchange approximation (FLEX) [123, 124, 125, 126, 127] to calculate the self energy in a self consistent manner. Details of the MRDF method is described in the next section. The momentum anisotropy arises in the present model due to charge and spin fluctuations and is different from the momentum anisotropy that arises in the AF phase. The low-energy AF fluctuations dominates near the $\mathbf{Q} = (\pi, \pi)$ where as high energy paramagnons (marginal) fluctuations dominate along the $\mathbf{q} = (\pi, 0)/(0, \pi)$ directions. In the large ordering limit ($Q > 2k_F$), Sachdev *et al.* have pointed that the paramagnons (particle-hole continuum) become decoupled from the AF fluctuations in both energy and momentum domains[128, 104] and the AF fluctuations dies off around the AF QCP near 5% hole doping, and do not survive up to the optimal dopings.[129, 130, 131] This study shows that the dominant contributions to the NFL state at the optimal doping come from the density fluctuations near $\mathbf{k} \sim (\pi, 0)/(0, \pi)$ and the VHS in cuprates is also present around these antinodal points. Therefore, density fluctuations induced self-energy dominates in the antinodal region of the BZ and have its maximum effect when the Fermi level passes through the VHS (at the Lifshitz transition). Such density fluctuations are marginal, occur in the energy range of 300 – 500meV, and survive at all dopings up to overdoped samples.[132] We emphasize that due to the self-energy correction and the momentum anisotropy, the VHS does not have a true singularity, rather a broad hump. Therefore, neither the density fluctuations, nor the spectral functions possess any non-analytic behavior at all dopings, and the complex self-energy remains analytical at all momenta, energies, and

dopings in our model.

Anisotropy in the self-energy can be conveniently encoded by a k -dependent exponent ($p_{\mathbf{k}}$) in the imaginary part of the self-energy Σ'' , as

$$\Sigma''(\mathbf{k}, \omega) = \alpha_{\mathbf{k}} |\omega|^{p_{\mathbf{k}}}. \quad (2.2.1)$$

The quasiparticle residue is defined as $Z_{\mathbf{k}} = (1 - \partial\Sigma'/\partial\omega)_{\omega=0}^{-1}$, where $\Sigma'(\mathbf{k}, \omega)$ is the real part of the self-energy. Due to analyticity of the self-energy, both the real and imaginary parts of the self-energy are related to each other by Kramers-Kronig relation at all \mathbf{k} -points. Note that exponent $p_{\mathbf{k}} \geq 1$ as we go to the limit $\omega \rightarrow 0$. So real part of self-energy does not have any singularity. In what follows, both $p_{\mathbf{k}}$ and $Z_{\mathbf{k}}$ have characteristically similar and strong \mathbf{k} -dependence in the BZ: in the antinodal region (NFL ‘hot-spots’) $p_{\mathbf{k}} \rightarrow 1$, and $Z_{\mathbf{k}}$ is minimal, giving NFL self-energy, while the remaining low-density region (‘cold-spots’) gives $p_{\mathbf{k}} \sim 2$, $Z_{\mathbf{k}}$ is maximal (see Fig. 2.6). This allows a coexistence and competition between the NFL and FL physics in the same system. It is important to note that $\Sigma''(\mathbf{k}_F, 0) = 0$ at all dopings, implying that all quasiparticles in the BZ (including in the NFL region) have well defined poles on the FS. However, due to the strong momentum dependence of $Z_{\mathbf{k}}$, the spectral weight gradually decreases in the antinodal region, giving the impression of a ‘Fermi arc’ in the spectral weight maps. Such a momentum dependence of $p_{\mathbf{k}}$ obtained in the MRDF method is in qualitative agreement with a QMC calculation of a single band Hubbard model[133].

2.3 Perturbative approach and MRDF model

Correlation strength of the studied material is crucial for the success of perturbative approach. If I start with small coupling limit (where FL theory is valid) and gradually increase the coupling strength I move away from FL behavior and hit a critical coupling strength where FL theory breaks down. Such a critical coupling usually indicates a QCP. Perturbative approach is usually valid if one approaches NFL regime from the above mentioned FL side. There exists a number of perturbative approaches of the self-energy calculation based on QCP,[107, 108, 109, 110, 111, 134, 102], along with other theories like Hertz-Millis theory of quantum phase transition,[135, 103, 104, 105, 106] nearly antiferromagnetic model,[136, 137] spin-

fluctuation model,[138, 97] large- N expansion of bosonic field,[139] ϵ -expansion of the bare dispersion,[140] dimension regularization[141] method. These methods often suggest that the self-energy becomes non-analytic at the critical point, and quasiparticles can no longer be defined. In such cases, the perturbative theory itself becomes inapt at the QCP[109, 111, 100]. On the other hand, in the strong coupling limit, one approaches the NFL limit from the other side, i.e., one basically studies how localized electrons gradually become conducting via many-body effects. A number of non-perturbative treatments, such as spin-Fermion model[142], two-fluid model,[143] slave-boson,[144] $t - J$ model,[145], fractional FL,[99, 96] hidden FL,[146] dynamical mean-field theory (DMFT)[147, 148] holographic NFL,[149] dimension-regularization method[150] are used here. In these cases, conductivity bears out from the localized states via quantum fluctuations between the localized and conducting states. Both approaches, however, indicate a commonality that in the NFL state, the low-energy conducting states are neither fully itinerant, nor fully localized but reside in a dissonant state between them. Such a dual nature of electrons is the characteristics of the intermediate coupling region where the correlation strength is of the order of its kinetic energy term. In this correlation limit, the quantum fluctuations become either *massless*, or *marginal*, and produce the imaginary part of the self-energy $\Sigma'' \propto \max(|\omega|, T)$. Hence, a marginal FL (MFL) state arises in the low- T limit.[151, 152]

The correct correlation strength of cuprates must be in intermediate regime for the perturbation theory to be applied on it. Quantum Monte-Carlo (QMC),[153] DMFT,[154, 155] and random-phase approximation (RPA) based fluctuation-exchange theory[123, 156] consistently suggest that, indeed, cuprates lie in the intermediate correlation strength, at least in the doped samples. The non-interacting band structure of cuprate can be described by a single and strongly anisotropic band passing through the Fermi level. I consider a realistic band structure including up to fourth order tight-binding hoppings ($t, t', t'',$ and t''') as

$$\begin{aligned} \xi_k = & -2t(\cos k_x + \cos k_y) - 4t' \cos k_x \cos k_y \\ & -2t''(\cos 2k_x + \cos 2k_y) - 4t''' \cos 2k_x \cos 2k_y - \xi_F. \end{aligned} \quad (2.3.1)$$

The second nearest neighbor hopping t' has a special importance in cuprates as it controls the flatness of the band near $k = (\pi, 0)$ and its equivalent points. This generates a paramount

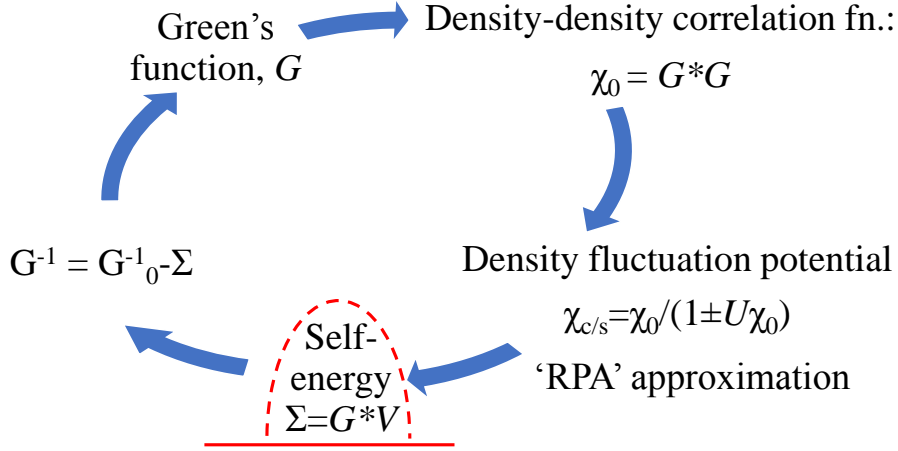


Figure 2.2: Schematic diagram showing the self consistent loop of MRDF method.

degeneracy in the DOSs, and hence VHS arises. As t' increases, the degeneracy also increases, and the system becomes more NFL like. Interestingly, an earlier Density Functional Theory (DFT) calculation demonstrated that the optimal T_c in different cuprates scales almost linearly with the corresponding t'/t ratio.[157] This produces a link between the NFL physics and T_c with a single, *ab-initio* parameter.

Table 2.1: Full tight binding parameters for LSCO. All energies are given in eV.[158]

Material	LSCO
t	0.4195
t'	-0.0375
t''	0.018
t'''	0.034
U	1.6

To add the effect of correlation I start with a single band Hubbard model and calculate the effect of the correlation by computing the full spectrum of both charge- and spin-fluctuations in a self-consistent way. The correlation part is included within the RPA approximation, by summing over the bubble diagrams (see Fig. 2.3), where the ladder diagrams are included in the Bethe-Salpeter vertex correction.[159] The higher-order Maki-Thompson (MT),[160] and Aslamasov-Larkin (AL)[161] terms, beyond the RPA diagram, are shown in 2.8.6 to scale as

U/\mathcal{W}^2 , and U^2/\mathcal{W}^6 (\mathcal{W} is the band gap and U is the onsite Hubbard interaction), respectively, and thus can be neglected in the intermediate coupling regime. The coupling between density fluctuations and electrons gives rise to a complex self-energy, which can be calculated within the Hedin's approach.[162] Here we use the self-consistent momentum-resolved density fluctuation (MRDF) method[123, 124, 125, 126] in which all quantities including single-particle Green's function, two-particle correlation functions, and the three-point vertex corrections are calculated self-consistently with the self-energy correction. In this way, the present method is an improved version of the FLEX model[134] without self-energy corrections in the two-particle term, or the single-shot GW calculation without a vertex correction.[163, 164] A schematic diagram of our self-consistent method is shown in Fig. 2.2. In the first iteration we calculate the bare Green's function $G(\mathbf{k}, \omega)$ from the tight-binding model. This Green's function is used to evaluate the bare correlator χ as

$$\chi(\mathbf{q}, \varepsilon) = \frac{1}{N} \sum_{\mathbf{k}} \int \frac{d\omega_1}{2\pi} \int \frac{d\omega_2}{2\pi} A(\mathbf{k}, \omega_1) A(\mathbf{k} + \mathbf{q}, \omega_2) \Gamma(\mathbf{k}, \mathbf{q}, \omega_1, \omega_2) \frac{f(\omega_1) - f(\omega_2)}{\varepsilon + i\delta - \omega_2 + \omega_1}. \quad (2.3.2)$$

Here $f(\omega)$ is fermionic distribution functions, $A(\mathbf{k}, \omega) = -\text{Im}G(\mathbf{k}, \omega)/\pi$ is the spectral weight and $\Gamma(\mathbf{k}, \mathbf{q}, \omega_1, \omega_2)$ is the density vertex correction. For bare Green's function $A(\mathbf{k}, \omega)$ is a Dirac delta function and $\Gamma(\mathbf{k}, \mathbf{q}, \omega_1, \omega_2) = 1$. Next I include the correlation part of the Hubbard model by computing the back-reaction potential of quasiparticle density fluctuations $V_\nu(\mathbf{q}, \varepsilon)$ which are separated into the spin ($\nu = 1$) and charge ($\nu = 2$) density channels within the RPA model as

$$V_\nu(\mathbf{q}, \varepsilon) = \frac{\eta_\nu}{2} \text{Im} \left[\frac{U^2 \chi(\mathbf{q}, \varepsilon)}{1 \mp U \chi(\mathbf{q}, \varepsilon)} \right], \quad (2.3.3)$$

where $\eta_1 = 3$, and $\eta_2 = 1$, and U is the onsite Hubbard interaction. This potential $V_\nu(\mathbf{q}, \varepsilon)$ is used to calculate the self-energy within Hedin's approach which can be written as (see A.2):

$$\begin{aligned} \Sigma_\nu(\mathbf{k}, \omega) &= \frac{1}{N} \sum_{\mathbf{q}} \int_0^\infty \frac{d\varepsilon}{2\pi} \int_{-\infty}^\infty \frac{d\omega'}{2\pi} V_\nu(\mathbf{q}, \varepsilon) \Gamma_\nu(\mathbf{k}, \mathbf{q}, \omega', \varepsilon) \\ &\times A(\mathbf{k} - \mathbf{q}, \omega') \left[\frac{1 - f(\omega') + n(\varepsilon)}{\omega + i\delta - \omega' - \varepsilon} + \frac{f(\omega') + n(\varepsilon)}{\omega + i\delta - \omega' + \varepsilon} \right], \quad (2.3.4) \end{aligned}$$

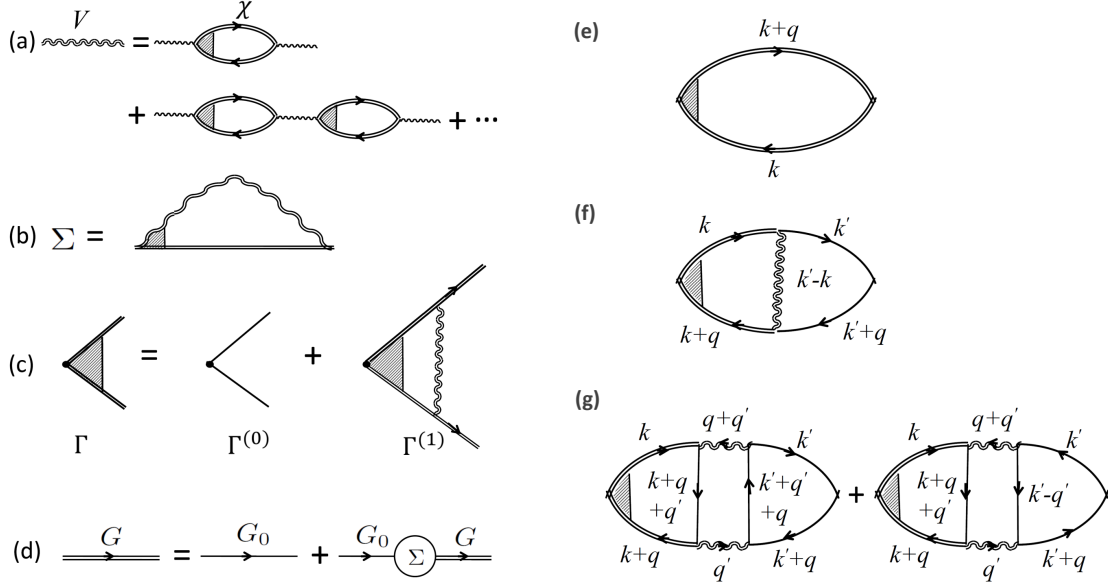


Figure 2.3: (a-d) Diagrams of various quantities of the MRDF model. (a) MRDF potential, (b) self energy, (c) Bethe-Salpeter vertex equation, (d) Dyson equation. (e-g) Diagrams of various quantities for conductivity calculation: (e) bubble diagram from Kubo formula (f) Maki-Thomson (MT) diagram, (g) Aslamasov-Larkin (AL) diagram. Double solid line represents self-energy dressed Green's function G , while single solid line is for the bare Green's function (G^0). Double wavy line represents the fluctuation-exchange potential. $\Gamma^{(0)}$, and $\Gamma^{(1)}$ are the bare and self-consistent vertex corrections (the same diagram applies to both density and current vertex corrections).

where $n(\varepsilon)$ is bosonic distribution functions and N is the total number of lattice sites. This self energy is used to calculate the self energy dressed Green's function or interacting Green's function $G(\mathbf{k}, \omega) = [\omega - \xi_{\mathbf{k}} - \Sigma(\mathbf{k}, \omega)]^{-1}$. In the next step this $G(\mathbf{k}, \omega)$ is used to calculate $\chi(\mathbf{q}, \varepsilon)$, which closes the self-consistent loop. The spectral function is now self energy dressed which is given by $A(\mathbf{k}, \omega) = -\text{Im}G(\mathbf{k}, \omega)/\pi$ and $\Gamma(\mathbf{k}, \mathbf{q}, \omega, \varepsilon)$ is the density vertex correction which is no longer equal to one. Please note that due to the strong anisotropy in the self-energy, the Migdal's approximation is not valid here, and vertex correction becomes important. Furthermore, the \mathbf{k} -dependent $\Sigma(\mathbf{k}, \omega)$ prioritizes the current-current vertex term Γ , which also affects the density vertex Γ due to conservation principles (it is customary to denote the current and density vertices by vector and scalar symbols Γ , and Γ , respectively)[165]. Since the system possesses both gauge- and spin-rotational symmetries without and with the self-energy corrections, the conservations of charge and spin densities lead to a simplified algebraic form of the vertex correction, as known by Ward's identity.[166] This identity imposes a specific

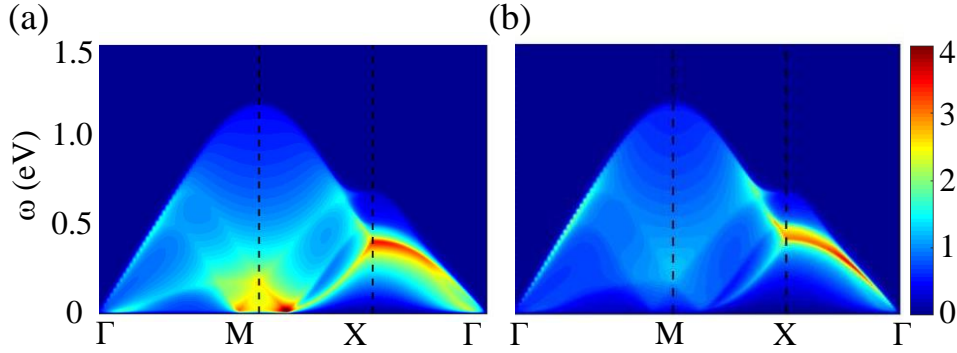


Figure 2.4: Density fluctuation spectrum for (a) spin, (b) charge channels. Here we plotted the imaginary part of the RPA susceptibilities: $\chi/(1 \mp U\chi)$ for spin and charge densities as a function of ω along three high symmetric momentum directions: $\Gamma(0,0)$ - $M(\pi, \pi)$ - $X(\pi, 0)$ - Γ for 20% hole doped LSCO. These RPA susceptibilities are directly linked to the fluctuation potential V_ν in Eq. (2.3.3) with the multiplication of the constant factor $U^2\eta_\nu/2$. The main feature of the density fluctuation is the dispersive paramagnon-like mode along the X - Γ direction. Such a mode is observed in RIXS spectrum in various cuprates.[168] This mode is responsible for the NFL state in the antinodal region.

relation between the self-energy and the density vertex correction as (see Sec. 2.8.7 for the derivation) [167]

$$\Gamma(\mathbf{k}, \mathbf{q}, \omega, \epsilon) \approx 1 - \frac{\partial \Sigma'(\mathbf{k}, \omega)}{\partial \omega} = Z_{\mathbf{k}}^{-1}(\omega). \quad (2.3.5)$$

Such a vertex correction is not only important to preserve the sum-rules, but also it helps to produce the correct frequency values ($\sim 500\text{meV}$) and the strength of the fluctuation-exchange potential V , the self-energy Σ , as well as spectral functions A , in consistence with their corresponding experimental results.[132]

In the present MRDF model, calculations are carried out in the self-consistent loop described above until the Green's function converges. This model is restricted to the intermediate coupling regime, where the value of Hubbard U is just below the self-energy renormalized bandwidth \mathcal{W} (evaluated self-consistently). This is the Brinkman-Rice criterion.[169] The value of U determines the overall strength of the NFL state, but interestingly, it does not affect much the anisotropy in the self-energy (as shown in Sec. 2.7).

While the numerical computations involve the full self-energy anisotropy, some interesting properties can be extracted if the FL ansatz of the self-energy is imposed. That means, the self-energy is approximated as $\Sigma(\mathbf{k}, \omega) = \Sigma(\mathbf{k}, 0) + (1 - Z_{\mathbf{k}}^{-1})\omega$, where $Z_{\mathbf{k}}$ is the anisotropic quasiparticle residue at the Fermi level, defined before. The dressed quasiparticle band is obtained

as $\bar{\xi}_{\mathbf{k}} = Z_{\mathbf{k}}\xi_{\mathbf{k}}$. Substituting the corresponding spectral function as $A(\mathbf{k}, \omega) = Z_{\mathbf{k}}/(\omega + i\delta - \bar{\xi}_{\mathbf{k}})$ in Eq. (2.3.2), we find that $\chi(\mathbf{q}, \varepsilon) = \Gamma Z^2 \chi_0(\mathbf{q}, \varepsilon) = Z \chi_0(\mathbf{q}, \varepsilon)$, where χ_0 is the bare Lindhard susceptibility (without a self-energy correction), and Z is the momentum averaged renormalization factor. This means, both the kinetic energy and the correlation function are renormalized in the same way, a consequence of the Ward's identity. Furthermore, the MRDF potential in Eq. (2.3.3) is also renormalized by the same value if the interaction U is also renormalized similarly, i.e., if $U = ZU_0$, where U_0 denotes the bare Hubbard interaction. This yields $V_{\nu}(\mathbf{q}, \varepsilon) = ZV_{\nu}^0(\mathbf{q}, \varepsilon)$, where $V_{\nu}^0(\mathbf{q}, \varepsilon)$ is the bare fluctuation-exchange potential consisting of bare χ_0 , and bare U_0 in Eq. (2.3.3). Since the kinetic and interaction terms scale in the same way, the system always maintains the intermediate coupling strength. Once the momentum dependence of the renormalization factor is tuned on, such a simple, analytical proof is difficult to achieve. However, the f -sum rules remained valid as shown in Sec. 2.8, and the MRDF method maintains the intermediate coupling scenario.

2.4 Self energy results

For the presentation of the self-energy results in this section, I focus on $\text{La}_{2-x}\text{Sr}_x\text{CuO}_4$ (LSCO) cuprate. Its tight-binding (TB) band parameters are obtained from the corresponding DFT band structure (see Table 2.1). The self-energy result is shown near the optimal doping ($x = 0.2$) with $U = 1$ eV (where the bandwidth is $\mathcal{W} \sim 4$ eV). The self-energy is plotted for several representative momenta in Fig. 2.5. The results can be compared with the corresponding results obtained from ARPES for the same sample. Both experiment and theory consistently exhibit a characteristic momentum dependence of the self-energy. Σ'' varies linearly with frequency in the antinodal region, while it gradually becomes quadratic as we move towards the nodal region.

The origin of the momentum dependence of the self-energy can be traced back to the momentum dependence of V_{ν} [Fig. 2.4] and the spectral weight maps [Fig. 2.6]. I focus the discussion on the two momentum regions, namely, the NFL region around $\mathbf{k}_v \sim (\pi, 0)$, and the FL regions $\mathbf{k}_h \sim \Gamma$, and (π, π) . The self-energy creates incoherent, localized states at the bottom and top of the bands at the Γ , and (π, π) point, which are reminiscences of the lower

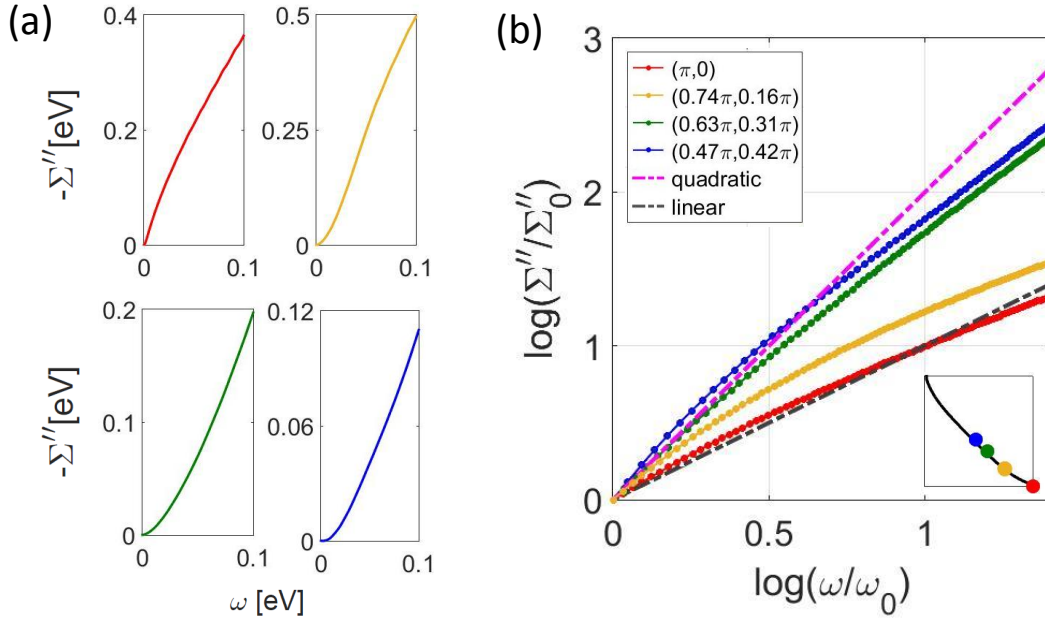


Figure 2.5: (a) Calculated $\Sigma''(\omega)$ at different k -points for 20 % hole doped LSCO. (b) Logarithmic plot of $\Sigma''(\omega)$ vs ω with $\omega_0 = 0\text{eV}$. Colors represent the same k -points in (a) and (b). Pink and black dashed lines are guide to the eyes to a quadratic and linear behavior, respectively. *Inset*: Corresponding k -points in the first quadrant of the BZ where the self-energy is plotted. Bottom-left corner is at the Γ -point, while the top-right corner is the (π, π) -point. The black line indicates the non-interacting Fermi Surface.

and upper Hubbard bands (L/UHBs), respectively. The low-energy VHS states around k_v near the Fermi level become renormalized and remain ‘itinerant’[127, 123]. These two states are separated by the so-called ‘waterfall’ energy (~ 500 meV) where the spectral weight is strongly suppressed (see Ref.[123] for details of spectral function). $V_\nu(\mathbf{q}, \epsilon)$ arises mainly from density fluctuations between the itinerant (at VHS) and localized (at the L/UHB) states in the particle-hole channel. Below the NFL-doping where the VHS lies below E_F , the density fluctuations arise between the VHS at k_v and the UHB at (π, π) . Above the NFL-doping, the VHS crosses above the Fermi level, and the corresponding fluctuation switches channels between the VHS and the LHB at the Γ -point. In both cases, the momentum conservation principle localizes V_ν at $(\mathbf{q}_v, \epsilon_{\text{sf}})$, where $\epsilon_{\text{sf}} \sim 300 - 500\text{meV}$, and $\mathbf{q}_v \sim (\pi, 0)/(0, \pi)$. The self-energy dressed density fluctuation spectrum is visualized in Fig. 2.4 for the spin and charge channels. Consequently, these fluctuations persist from underdoping to overdoping, as observed by resonant-inelastic X-ray scattering spectroscopy (RIXS)[168]. A direct comparison of the computed density fluctuations spectrum with the corresponding RIXS data for different dop-

ings have been shown in the references[170, 123]. Substituting $V_\nu(\mathbf{q}_\nu, \epsilon_{sf})$ in Eq. (2.8.1), we find that $\Sigma''_\nu(\mathbf{k}, \omega) \approx V_\nu(\mathbf{q}_\nu, \epsilon_{sf})A(\mathbf{k} - \mathbf{q}_\nu, \omega + \epsilon_{sf})$. Therefore, we can relate the NFL self-energy at \mathbf{k}_ν , i.e., $\Sigma''_\nu(\mathbf{k}_\nu, \omega)$ to depend mainly on the high-energy Hubbard states $A(\mathbf{k}_h, \epsilon_{sf} + \omega)$. In other words, the NFL self-energy arises from the ‘high-energy’ localized Hubbard bands, which transfer the localized spectral density via density-density fluctuation channels to the low-energy states at the antinodal region. On the other hand, the FL self-energies near \mathbf{k}_h -points depend mainly on the itinerant VHS spectral weights at $A(\mathbf{k}_\nu)$. Since the spectral function has isolated poles at all momenta and frequencies, both the NFL and FL self-energies are analytic functions in the present case. This way the present model is different from the prior perturbative treatments of the NFL state.[107, 108, 109, 110, 111, 100, 171]

In Fig. 2.5(a) the imaginary part of self-energy (Σ'') is plotted as a function of frequency(ω), and the corresponding log-log plot is shown in Fig. 2.5(b) (a detailed procedure is given in A.1). From the log-log plot, we can conclude that the exponent is ~ 1 in the antinodal region (NFL-state), and ~ 2 away from the antinodal region (FL-states). In addition, the fitting is not monotonic with frequency, because both the exponent p_k and the coefficient α_k in Eq. (2.2.1) are also frequency dependent. But for the low-temperature transport properties, the low-energy fitting suffices a good explanation.

Fig. 2.6 shows the momentum dependence of the exponent p_k , and compare it with that of the mass renormalization $m^*/m_b = Z_k^{-1}$ ($m_b =$ bare band mass), and the spectral weight map $A(\mathbf{k}_F, 0)$. The results are compared for three different dopings: at $x = 0.1$ (left), optimal doping $x = 0.2$ (middle), and $x = 0.3$ (right). It immediately shows a one-to-one correspondence between the three quantities at all dopings, further justifying that the self-energy is always non-singular. The spectral weight can be defined in terms of Z_k and Σ'' as

$$A(\mathbf{k}, \omega) = -\frac{1}{\pi} \frac{Z_k(\Sigma''(\mathbf{k}, \omega) + \delta)}{(\omega - \xi_k)^2 + (\Sigma''(\mathbf{k}, \omega) + \delta)^2}. \quad (2.4.1)$$

Since $\Sigma'' = 0$ at $\omega = 0$ at all \mathbf{k} , the spectral functions have a delta function-like peak at the Fermi energy. This suggests that the FS remains coherent at all momenta and dopings. The self-energy dressed FS deviates from the bare FS (black line) both in shape and spectral weight. The spectral weight renormalization on the FS is solely governed by the quasiparticle residue Z_k . The shift of the FS is dictated by $\Sigma'(\mathbf{k}, 0)$ which is also related to p_k via Kramer’s-Kronig

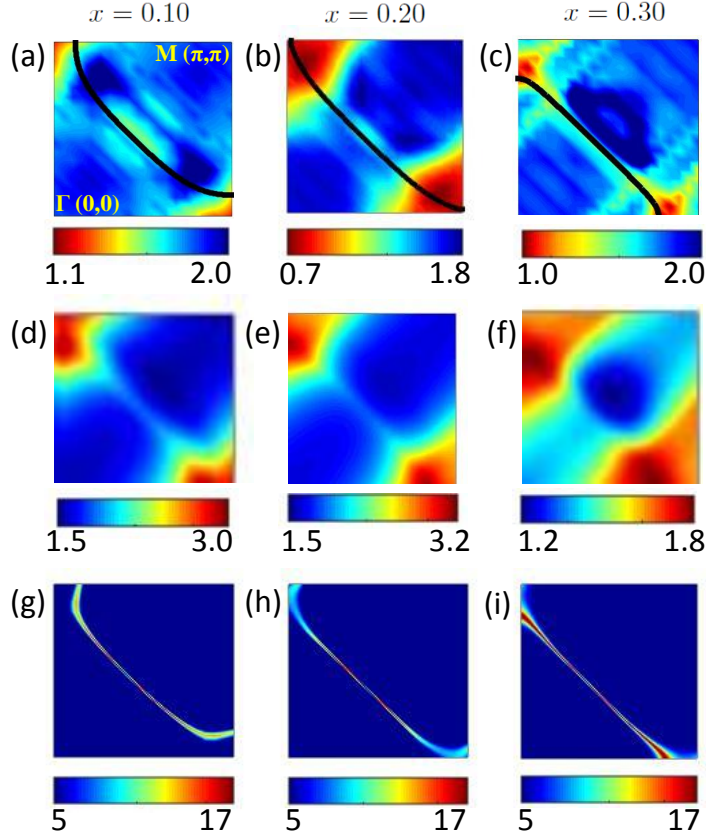


Figure 2.6: (a-c) The self-energy exponent p_k in the entire first quadrant of the BZ is shown in the underdoped, optimal doped, and the overdoped regions, respectively. Bottom-left corner is at the Γ -point, while the top-right corner is the (π, π) -point. The black lines indicate the corresponding Fermi Surface and the colorbars indicate the value of exponent p_k . (d-f) Inverse of quasiparticle weight $Z_k^{-1} = m^*/m_b$ at Fermi energy ($\omega = 0$) is plotted for the same dopings in in (a). (g-i) Spectral weight plots at the Fermi level, including the momentum dependence self-energy. Each column corresponds to the same doping.

relation:

$$\Sigma'(\mathbf{k}, 0) = \frac{1}{\pi} \int_{-\infty}^{\infty} d\omega \frac{\Sigma''(\mathbf{k}, \omega)}{\omega}. \quad (2.4.2)$$

Therefore, we observe that the renormalized Fermi momenta \mathbf{k}_F deviate more from its non-interacting values in the antinodal direction, compared to the other points. Finally, the number of electron is kept fixed by recalculating the chemical potential ξ_F with the self-energy correction. Therefore, the Luttinger theorem remains valid at all dopings.

The above analysis demonstrates that due to the analytic form of the self-energy, p_k , Z_k , and A_k all are related to each other at all \mathbf{k} -values. All three quantities are minimum at the antinodal point, suggesting that the states near this region are more strongly correlated than

the rest of the BZ. Also, from Eq. (2.4.2), it is found that $\Sigma'(\mathbf{k}, 0)$ is maximum at the antinodal point, and thus the corresponding Fermi momenta \mathbf{k}_F deviate more from its non-interacting values here. To have the Luttinger theorem valid, the Fermi momenta elsewhere must be smaller.

The overall k -dependence of p_k remains similar at all dopings: p_k attains its minimum value around the antinodal region. In the underdoped region, where the VHS is well below ξ_F , we find that the overall p_k profile is less k -sensitive. Near the optimal doping, where the VHS exactly crosses above ξ_F , the k -dependence of p_k becomes strongest, and the NFL region occupies larger BZ volume. Also at optimal doping, p_k obtains its minimum value near the antinodal region, which is the minimum possible value of p_k at all dopings and momenta for this material. [Similar trend in the resistivity-temperature exponent can be found in the next section.](#) Finally, as the VHS crosses above ε_F , again the value of p_k increases. Interestingly, in the overdoped region, where [FL-behavior is expected from transport properties](#), the antinodal regions continue to show NFL self-energy behavior, in consistent with the ARPES data on LSCO at $x = 0.23$.[\[119\]](#)

The result suggests that the quasiparticles have well-defined poles in both FL and NFL states at all \mathbf{k}_F , but owing to the \mathbf{k} -dependent $\Sigma'(\mathbf{k}, 0)$, the deviation of the poles from its non-interacting FS is not monotonic on the FS. The only source of the spectral weight renormalization on the FS is the momentum dependent Z_k . Expectedly, spectral weight gradually decreases as we move to the antinodal directions, giving the shape of a coherent ‘Fermi arc’, often observed in underdoped cuprates.[\[172\]](#)

2.5 Resistivity calculation

When the k -dependence of the self-energy is neglected, a direct link between the microscopic single-particle spectral properties and the macroscopic transport behavior ($n \approx p$) can be established. However, as the system acquires strong anisotropy in p_k , it becomes less intuitive to deduce the overall correlation landscape from transport properties. I compute the DC conductivity by using the Kubo formula. I consider a one-loop bubble diagram with the current-current vertex correction Γ . Because of the vertex correction, the higher-order MT,[\[160\]](#) and

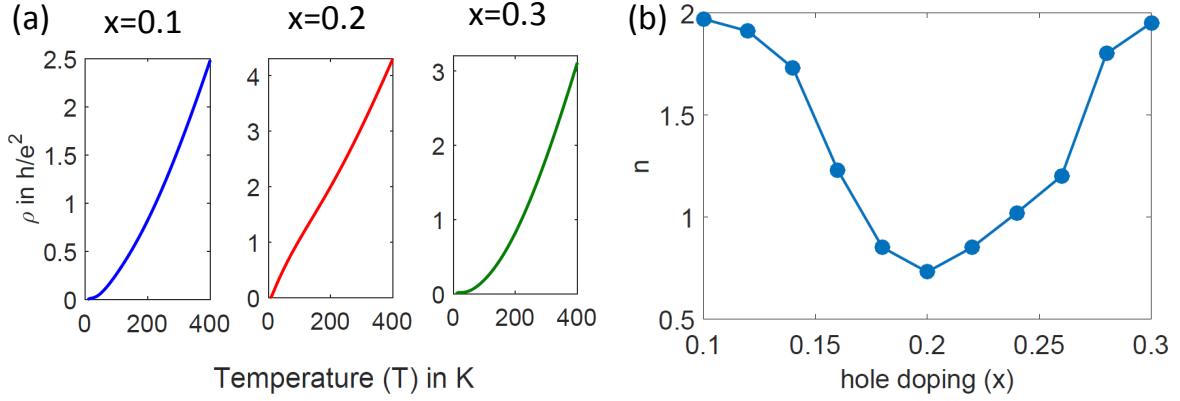


Figure 2.7: (a) Resistivity is plotted as a function of temperature for different doping for LSCO. (b) The resistivity-temperature exponent in the low- T region is plotted as a function of dopings for LSCO which exhibits minimum in exponent near the optimal dopings where the corresponding VHS passes through the Fermi level.

AL terms[161] for the current-current correlation functions give vanishingly small contributions, unless one enters into non-analytic self-energy[173] or if the self-energy has pseudogap behavior.[174] Such an one-loop Kubo formula, with and without vertex correction, is also used previously in cuprates within DMFT calculation.[154, 155, 146] The current vertex is calculated from the same Bethe-Salpeter form,[159] which is calculated self-consistently using Ward identity[166] (see Sec. 2.8.7). Within the linear response theory, in the limit of $\mathbf{q} \rightarrow 0$, we obtain:

$$\sigma = \frac{e^2}{3\hbar^2 m^2} \frac{1}{N} \sum_{\mathbf{k}} \Gamma^{(0)}(\mathbf{k}, \omega) \cdot \Gamma(\mathbf{k}, \omega) \int \frac{d\omega}{2\pi} A^2(\mathbf{k}, \omega) \left(-\frac{df(\omega)}{d\omega} \right), \quad (2.5.1)$$

where e and \hbar have the usual meanings, and $\Gamma^{(0)}(\mathbf{k}, \omega)$ and $\Gamma(\mathbf{k}, \omega)$ are the bare and full current vertices. For $\mathbf{q} \rightarrow 0$, the bare vertex reduces to $\Gamma^{(0)}(\mathbf{k}, \omega) = m\mathbf{v}(\mathbf{k})$, where $\mathbf{v}(\mathbf{k})$ is the band velocity, and the full vertex is

$$\Gamma(\mathbf{k}, \omega) = m\mathbf{v}(\mathbf{k}) + m\nabla\Sigma(\mathbf{k}, \omega) = -m\nabla G^{-1}(\mathbf{k}, \omega). \quad (2.5.2)$$

The conductivity obeys the f -sum rule as shown in Sec. 2.8. Only σ_{xx} component is considered here. In the absence of any anomalous term, the resistivity is obtained as $\rho_{xx} = 1/\sigma_{xx}$. Please note that the imaginary part of the self-energy is expected to be finite at $\omega = 0$ at finite

temperature due to thermal broadening. So the finite temperature scattering rate is neglected in this study. It is challenging to find the form of finite temperature self-energy within the present MRDF method. The resistivity results are presented in Fig. 2.7(a) for LSCO at different dopings. It is observed that the resistivity exponent becomes minimum near the optimal doping where the VHS crosses ξ_F , see Fig. 2.7(b). Here, the system acquires dominant NFL-behavior with $n \sim 1$. At the same doping, the self-energy exponent p_k in Fig. 2.6(b) not only obtains its minimum value, but also it occupies larger k -space area. However, the other parts of the BZ remain FL-like with p_k as large as ~ 1.8 . Similarly, in both under- and overdopings, where $n \rightarrow 2$, the antinodal region continues to have $p_k \sim 1$. Cautionary remarks are in order. I have extended the one-band model to the deep underdoped region without including the pseudogap and other competing orders. Therefore, our calculation does not represent the experimental results in the deep underdoped region.

ADMR technique has the ability to probe the angular variation of the resistivity by tilting the magnetic field with the sample orientation. This allows to effectively measure the scattering life-time $1/\tau \propto \rho$ as a function of Fermi surface angle $\theta = \tan^{-1}(k_y/k_x)$. An earlier ADMR study on overdoped $Tl_2Ba_2CuO_{6+x}$ found that $1/\tau$ varies as T^2 in the nodal region ($\theta = 0$) and it gradually changes to T in the antinodal region ($\theta = 45^\circ$). [120, 121] This result is consistent with my findings of quasiparticle life-time variation shown in Fig. 2.6(a-c). Note that even the angle-integrated resistivity exponent is close to 2 in the overdoped region, however, its angle-dependent data reveals that both the single-particle life-time and scattering rate consistently remain NFL-like in the antinodal region. Such kind of angle dependent technique can be used to verify my predictions in cuprates in a wide range of region near critical doping.

2.6 Materials dependence of n and its correlation with T_c

The celebrated paper by Pavarini *et al.* [157] pointed out an intriguing relationship between the t'/t ratio obtained in different materials with their T_c . t'/t triggers higher degeneracy in the DOS (see Fig. 2.10(b)), and hence it is natural to expect that the strength of the NFL state would also increase. I calculate the resistivity exponent n for different values of t'/t by fixing the VHS at the ξ_F , and the result is plotted in Fig. 2.8. Indeed, I find that with

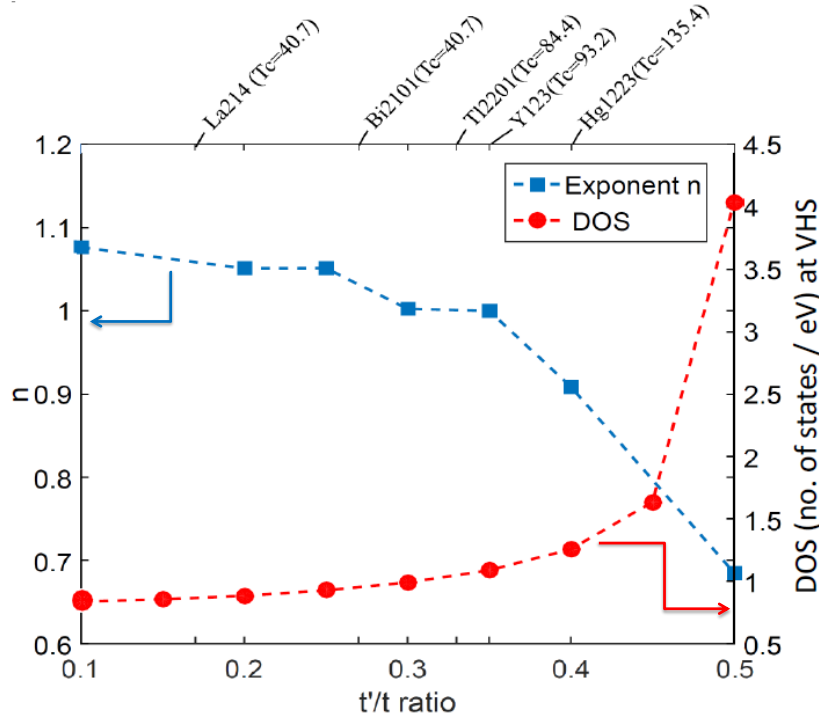


Figure 2.8: The resistivity exponent n , at the doping where the VHS passes through the Fermi level, is plotted for different values of t'/t , representing different cuprate materials.[157] This is the minimum value of n obtained across the doping range for a given t'/t since the DOS at E_F is maximum here (see the circle symbols for the DOS in the right-hand panel). At the top of the figure, we mention the corresponding cuprate materials with corresponding T_c , having different values of t'/t as obtained from the DFT calculation in Ref. [157]. Chemical compositions of cuprate materials are: La_2CuO_4 (La214), $\text{Bi}_2\text{Sr}_2\text{CuO}_6$ (Bi2101), $\text{Tl}_2\text{Ba}_2\text{CuO}_6$ (Tl2201), $\text{YBa}_2\text{Cu}_3\text{O}_7$ (Y123), $\text{HgBa}_2\text{Ca}_2\text{Cu}_3\text{O}_8$ (Hg1223).

increasing t'/t , n decreases, that means, the system becomes more NFL like. With increasing t'/t , both the DOS at VHS increases and the bandwidth decreases (see Sec. 2.7), and thus the NFL phenomena also increases. It is already known that the optimal T_c increases with increasing t'/t , [157] and with decreasing n . This phenomenon is consistently observed in various cuprates, pnictides and heavy-fermions.[101] My results thus shows that there is a microscopic connection between the NFL phenomena and T_c in the context of this empirical observation.

2.7 U dependence of various results

All results and conclusions presented above are obtained for material specific values of the Hubbard U (see Table 2.1). Here, I investigate them for different values of U and study their evolution. The following results also demonstrate the distinction between the doping dependence of the static correlation (U) and the dynamical correlation ($V(\omega)$) in Eq. 2.3.3).

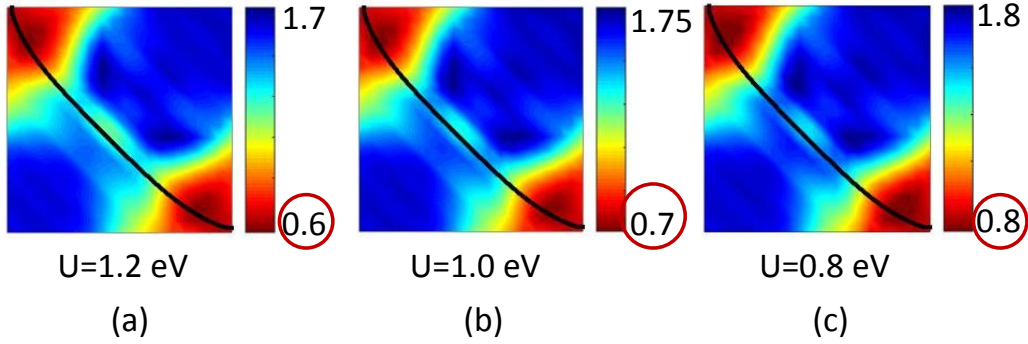


Figure 2.9: (a-c) Plots of the self-energy -frequency exponent p_k (defined in Eq. 1) for three different values of U for LSCO at $x = 0.20$. In all three cases, we notice that the overall momentum profile of p_k remains very much the same. This is expected since the anisotropy is related to the anisotropy in the electronic structure and correlation function, but not directly on the onsite U . The overall range of p_k (seen in the adjacent colorbars) however decreases with decreasing U . This means the system moves towards the FL state at a fixed doping as U decreases.

Keeping all other parameters the same, it is expected that the system would tend to transform from NFL to FL like as I decrease the values of U . This is what is observed in Fig. 2.9 where I plot the momentum profile of p_k at a fixed doping of $x = 0.20$ for LSCO for three different values of U . In all three cases, the momentum profile remains very much the same, as expected, since the momentum dependence is governed by the anisotropy in the band structure and correlation function. A characteristic change in the overall range of p_k (as highlighted by red circles in the adjacent colorbars) is observed. The result shows that both the minimum and the maximum values of p_k increases with decreasing U . In addition, it is also observed that the k -space area of the region, that deviates maximally from FL ($p_k \sim 1$), decreases with decreasing U , reflecting that the system moves towards FL as correlation weakens.

Finally I study the evolution of the t'/t vs. n plot for different values of U in Fig. 2.10. As mentioned before that n decreases as the t'/t ratio increases, keeping the corresponding

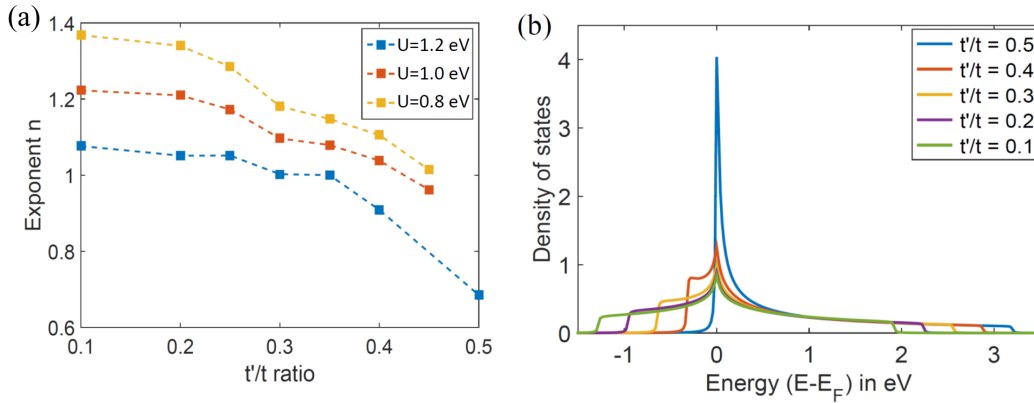


Figure 2.10: (a) Plots of t'/t vs. n for different values of U . As expected, the exponent n decreases with increasing U , but for all values of U , the t'/t dependence on n is maintained. (b) Non-interacting density of states (DOS) is shown as a function of energy for different values of the t'/t ratio. Note that the DOS at the VHS gradually increases with increasing t'/t ratio, as the flatness of the band increases at the antinodal point. The Fermi level for all cases is fixed at the VHS.

VHS fixed at the Fermi level for all cases. This is because the DOS at the VHS increases with increasing t'/t and the bandwidth simultaneously decreases. Therefore, the system becomes more NFL-like as t'/t increases. This conclusion remains intact as the values of U are tuned. For different values of U , the general trend of t'/t vs. n remains the same, however the overall range of n increases with decreasing U which is consistent with my observation in Fig. 2.9.

2.8 Discussions

2.8.1 Analytic self-energy in the NFL state

One of the important properties of the present results is that the self-energy is free from any essential singularity and non-analytic form at all momenta, energy, and doping. **Please note that here the word analytic is used in the sense that Kramers-Kronig relation is valid. In other words, the self-energy needs to be analytic in the upper half of the complex ω plane. This is achieved in the calculation by putting a small broadening $\omega \rightarrow \omega + i\delta_\omega$. This δ_ω is different from thermal broadening and appears only for numerical calculation and can be taken arbitrarily small to approach the zero limit. Introduction of this broadening removes all**

non-analyticity of imaginary part of self-energy (Eq. (2.2.1)) from the upper half complex ω plane. However, from Eq. (2.3.4), it can be deduced that the self-energy can become non-analytic when either the potential $V_\nu(\mathbf{k}, \epsilon)$ or the spectral function $A(\mathbf{k}, \omega)$, has a non-analytic form. Both these cases are discussed separately below.

(a) Near a Hertz-Millis QCP, there arises a singularity in the spin and/or charge potential V_ν at a characteristic wavelength, causing *massless* magnons or plasmons, respectively. Here we focus on the near-optimal doping region which is far away from the AF and CDW QCPs. And as discussed earlier, paramagnons remain massive at all momenta and doping, and gives no singular behavior. So, V_ν has no essential singularity in the doping range of present interest. Yet we can make few remarks. An AF QCP induced NFL model have been used earlier by Moriya *et al.*[138]. They found that the T -linear behavior in resistivity and d -wave superconductivity both arise from the strong AF fluctuations.[102] If this result holds in cuprates, one would obtain a T -linear NFL state at 5-7% doping. But the T -linear behavior is rather shifted to the optimal doping, where the AF fluctuations are negligibly small.[101, 130] The model was extended by Monthoux and Pines,[136] Millis-Monien-Pines[97] with a phenomenological model of the spin-fluctuation. Bicker *et al.* used a similar self-consistent FLEX model[134] of the spin-fluctuation mediated NFL calculations. But in all these models, the driving instability has been the the same $\mathbf{Q} = (\pi, \pi)$ AF fluctuation, and thus the realistic region of NFL state should be 5-7% doping. In a fully self-consistent scheme, the spin-fluctuation spectrum is modified by the self-energy effect, and such a renormalization effect is sometimes distinguished as the ‘mode-mode coupling’ effect.[175] In the mode-mode coupling theory, the magnetic instability is clearly modified, or sometimes removed due to the suppression of the spin-susceptibility from the self-energy correction. As a result, the long-range AF order does not occur in pure 2D systems, which means that the Mermin–Wagner theorem is satisfied here. In reality, the hole-doped cuprates exhibit an AF critical point around 5-7% doping *without* any apparent T -linear resistivity.[115, 176, 101, 98] There can be various reasons, such as finite three-dimensionality in cuprates,[158] second-order vertex correction (AL term),[173, 174] non-perturbative corrections,[100] etc., but it is not the main topic of our present work.

(b) Another possible source of singularity is the VHS in the single-particle spectral function $A(\mathbf{k}, \omega)$. An earlier DMFT calculation in a single band Hubbard model showed that as the VHS

is positioned exactly at the Fermi level, it gives rise to a non-analytical self-energy and thus one cannot treat the transport relaxation rate coming from the single-particle broadening.[171] Such a singularity is removed in our case due to multiple reasons and analytical self-energies are obtained even at the extreme NFL region. To understand this, the imaginary part of the self-energy can be written in an approximate form (from Eq. (2.3.4)) as

$$\Sigma''_{\nu}(\mathbf{k}, \omega) \propto \sum_{\mathbf{q}} \int d\epsilon V_{\nu}(\mathbf{q}, \epsilon) A(\mathbf{k} - \mathbf{q}, \omega + \epsilon). \quad (2.8.1)$$

In a local approximation where the potential is replaced with a \mathbf{q} -averaged potential, the analyticity of the self-energy is solely determined by the analyticity of the VHS. Therefore, if the VHS has the non-analytic cusp even after including the self-energy correction, the self-energy also becomes non-analytic.

When the \mathbf{k} -dependent self-energy is introduced, it can be seen in another way that the VHS is substantially weakened. Near the VHS region around $k_v = (\pi, 0)$, the first k -derivative of the bare dispersion vanishes, and thus the leading term in the band is $\xi_{\mathbf{k}} \approx k^2/m^*$, where k is measured with respect to k_v ($\hbar = 1$). Since $\xi_{\mathbf{k}}$ is a slowly varying function in momentum, one obtains a ‘flat-band’, leading to a non-analytic cusp in $d \geq 2$, and a logarithmic divergence in $d = 1$. In the \mathbf{k} -dependent self-energy correction, the renormalized band obtains an effective k -linear term from the self-energy as $\bar{\xi}_{\mathbf{k}} \approx \nabla \Sigma' \cdot \mathbf{k} + (1/m^* + \nabla^2 \Sigma')k^2$, where the k -derivatives are taken at \mathbf{k}_v . This linear-in- k term effectively destroys the essential criterion for a singularity at the VHS.

2.8.2 Sum rules and Luttinger theorem

Luttinger theory remains valid with the self-energy correction. This can be easily seen by the fact that $\Sigma''(\mathbf{k}, 0) = 0$ at all momenta. The spectral function obtains isolated poles on the FS at $\bar{\xi}_{\mathbf{k}_F} = \xi_{\mathbf{k}_F} - \bar{\mu} + \Sigma'(\mathbf{k}_F, 0)$, where $\xi_{\mathbf{k}}$ is understood to be the non-interacting dispersion without the chemical potential. Please note that the chemical potential $\bar{\mu}$ is different from that without the self-energy correction. When the self-energy is included, the chemical potential is adjusted to keep the number of electron conserved.

The f -sum rule in the spin and charge channels are also individually satisfied. This can

be proven in two ways. The vertex correction is important in the self-consistent scheme and usage of the Ward identity in the vertex correction ensures that the sum-rules remain intact. The basic principle in maintaining the sum rule is that one invokes the similar approximation in both density-, current-correlations functions as well as in the vertex function, and make sure that the Ward identity is followed. The f -sum rule for the densities[174] is

$$\frac{1}{\pi} \int d\epsilon \epsilon \Gamma_\nu(\mathbf{q}, \epsilon) V_\nu(\mathbf{q}, \epsilon) = \frac{1}{N} \sum_{\mathbf{k}} (\xi_{\mathbf{k}+\mathbf{q}} - \xi_{\mathbf{k}-\mathbf{q}} - 2\xi_{\mathbf{k}}) \langle n_\uparrow \pm n_\downarrow \rangle. \quad (2.8.2)$$

\pm signs indicate charge ($\nu = 1$) and spin ($\nu = 2$) densities. Since the spin is conserved here, $\frac{1}{\pi} \int d\epsilon \epsilon V_2(\mathbf{q}, \epsilon)$ must vanish. In the mean-field level without the self-energy correction, the potential V_ν^0 satisfy Eq. (2.8.2). Let us assume $\bar{V}_\nu(q, \epsilon)$ is the Z -renormalized potential which is obtained from Eqs. (2.3.3)-(2.3.2) by replacing the spectral function with its quasiparticle form $A(\mathbf{k}, \omega) = Z/(\omega - \bar{\xi}_{\mathbf{k}})$. This gives $V_\nu(\mathbf{q}, \epsilon) \approx Z\bar{V}_\nu(\mathbf{q}, \epsilon)$. Then we can easily show that the energy range (=bandwidth \mathcal{W}) of \bar{V} is reduced by Z (since the band is renormalized by the same Z). Since the vertex correction is $\Gamma \sim 1/Z$, we obtain $\Gamma(\mathbf{q}, \epsilon) V_\nu(\mathbf{q}, \epsilon) \approx V_\nu^0(\mathbf{q}, \epsilon)$. This is a direct consequence of the Ward identity in which the kinetic energy and the interaction potential are renormalized by the same factor Z , and thus the intermediate coupling scenario remains valid with and without including the self-energy correction.

Similarly, it can be proved that the optical sum rule also remains valid here. As mentioned in Sec. 2.5, the momentum dependent self-energy leads to a current-current vertex correction Γ which arises from the \mathbf{k} -derivative of the self-energy[167]. The current vertex is again related to the density vertex Γ via the Ward identity. The optical conductivity in terms of the Matsubara frequency, in the limit of $\mathbf{q} \rightarrow 0$, can be written as

$$\sigma(i\epsilon_m) = e^2 \frac{1}{N} \frac{1}{\beta} \sum_{\mathbf{k}, n} \mathbf{v}_k \cdot \Gamma(\mathbf{k}, i\omega_n, i\epsilon_m) G(\mathbf{k}, i\omega_n) G(\mathbf{k}, i\omega_n + i\epsilon_m). \quad (2.8.3)$$

Now from the Ward identity (see Eq. (2.8.11)), I substitute $m\mathbf{v}_k \cdot \Gamma(\mathbf{k}, i\omega_n, i\epsilon_m) = G^{-1}(\mathbf{k}, i\omega_n) -$

$G^{-1}(\mathbf{k}, i\omega_n + i\epsilon_m) + i\epsilon_n \Gamma(\mathbf{k}, i\omega_n, i\epsilon_m)$, where $\Gamma(\mathbf{k}, i\omega_n, i\epsilon_m)$ is the density vertex which gives

$$\begin{aligned} \sigma(i\epsilon_m) = & \frac{e^2}{m} \frac{1}{N} \frac{1}{\beta} \sum_{\mathbf{k}, n} [G(\mathbf{k}, i\omega_n + i\epsilon_m) - G(\mathbf{k}, i\omega_n) \\ & + i\epsilon_n \Gamma(\mathbf{k}, i\omega_n, i\epsilon_m) G(\mathbf{k}, i\omega_n) G(\mathbf{k}, i\omega_n + i\epsilon_m)]. \end{aligned} \quad (2.8.4)$$

In a homogeneous charge medium, the first two terms cancel each other. The last term

$$\frac{1}{N} \frac{1}{\beta} \sum_{\mathbf{k}, n} \Gamma(\mathbf{k}, i\omega_n, i\epsilon_m) G(\mathbf{k}, i\omega_n) G(\mathbf{k}, i\omega_n + i\epsilon_m)$$

is bare charge density susceptibility $\chi(\mathbf{q} \rightarrow 0, i\epsilon_m)$. Now the f -sum rule for density in Eq. (2.8.2) gives $\frac{1}{\beta} \sum_m i\epsilon_m \chi(\mathbf{q} \rightarrow 0, i\epsilon_m) = \pi n/2$, where n is the total charge density and this leads to $\frac{1}{\beta} \sum_m \sigma(i\epsilon_m) = \frac{\pi n e^2}{2m} = \omega_{pl}^2/8$, where ω_{pl} is the plasma frequency. The optical sum rule implies that the total absorbing power of the solid characterized by σ does not depend on the details of the interactions and is determined only by the total number of particles in the system.[177, 178] Such a sum rule is modified if the FS is partially or fully incoherent,[179] which is not the case in the model considered here.

2.8.3 Other angular-dependent self-energy calculations

Angle-dependent self-energy and NFL state have been studied earlier in a variety of approaches. Usually in cluster DMFT[180] and Dynamical Cluster Approximation (DCA)[181], the momentum dependent calculation is done in small clusters and [some of the results are in agreement with this MRDF calculation](#). However, there are other works where QCP appears near optimal doping. The disagreement may be attributed to taking only RPA corrections and neglecting higher-order diagrams in the present MRDF method. In FLEX and GW methods, which can retain the full spectrum of the correlation potential, one can account for the full-momentum dependence of the self-energy.[182, 183, 127, 126] In an earlier FLEX calculation[182], it was found that the self-energy effect is maximum at the AF ‘hot-spot’, rather than at the antinodal points. The apparent discrepancy between the FLEX and our MRDF method arises from how the spin-fluctuation potential is treated. FLEX calculation

only included the AF fluctuation, and does not include paramagnons. So, its range of validity is limited below $x < 0.10$ where the AF fluctuation is present. Also, in the context of heavy-fermion compounds, it was shown that a strongly anisotropic hybridization can generate angular dependent quasiparticle residue.[184] There are also non-perturbative calculations of the angle-dependent NFL state in the strong coupling region.[185] Their results are in general agreement with the FLEX calculation that the NFL state is stronger at the AF ‘hot-spot’. My method includes both AF and paramagnons fluctuations and show strong paramagnon dressed self-energy effect at the antinodal points in the optimal doping region. Finally, the obtained self-energy anisotropy is in qualitative agreement with a QMC calculation of a single band Hubbard band where the correlation is treated mainly for the paramagnon fluctuations.[133]

2.8.4 NFL induced Hertz-Millis QCP

As discussed above in various context, within the self-energy picture, two sources of NFL behavior are primarily discussed; through the singularities in the bosonic spectrum, or through that of the single particle spectral function. A major part of the literature discusses the origin of NFL state from the QCP physics, in which one obtains singularities in the bulk properties due to the singularities in the bosonic spectrum $V_\nu(\mathbf{q}, \epsilon)$. In another case, mass divergence of the quasiparticle spectrum $A(\mathbf{k}, \omega)$ can introduce non-analytic self-energy. A related situation arises in the case of a Pomeranchuk instability due to ‘soft’ FS, which gives strongly enhanced decay rate for single-particle excitations and NFL behavior.[186] More such cases are reviewed by Löhneysen *et al.* (in Sec. III G of Ref. [106]). Here, we obtain a different model where the dynamical itinerant-local density fluctuation causes the NFL behavior only in certain parts of the BZ, and it adiabatically connects to the FL region with analytic self-energy. So, one can ask the question: can the NFL state (without the QCP origin) give a QCP? Mermin-Wagner theorem prohibits the order induced by density fluctuations in two-dimensions. In the mode-mode coupling theory,[175, 138] it is shown that, for a AF fluctuation the self-energy reduces the spectral weight at the magnetic ‘hot-spot’ and thereby weakens the static nesting. Therefore, NFL state would oppose the formation of a QCP. According to the Hertz-Millis theory[135] both dynamical and static fluctuations are related to each other at the QCP. In my momentum dependent calculation, I find that the anisotropic self-energy is actually a

nonlocal effect (see Sec. 2.4). What I mean by this is that the dominant self-energy values at the antinodal point are mainly contributed by the incoherent, high-energy Hubbard bands at the BZ center and corner $[\Gamma, (\pi, \pi)]$. Therefore, the states away from the NFL momenta $[(\pi, 0)/(0, \pi)]$ can develop static orders if a suitable FS nesting is present. As in the case of cuprates, the NFL state at the optimal doping resides at the antinodal point, while the AF state and the d -wave superconductivity arise from the FS nesting at the magnetic ‘hot-spot’ (within a weak/intermediate coupling scenario). In fact, as the spectral weight is transferred from the antinodal to the rest of the BZ, the magnetic ‘hot-spots’ gain more spectral weight and the corresponding nesting can be enhanced. The present NFL state will however disfavor the charge density wave (CDW) which is believed to arise from the antinodal nesting.[98] My prior calculation indeed showed that the CDW nesting is shifted from the antinodal region to the tip of the ‘Fermi arc’ below the magnetic BZ, which is consistent with experiments.[172] However, such a CDW is also predicted to give a discontinuous, first-order phase transition near the optimal doping to avoid the nesting at the antinodal point.[172]

2.8.5 Pseudogap

The discussion of a pseudogap feature follows from the above section. First of all, the present calculation only deals with density-density correlation, and does not include Hartree/Fock terms. The correlation induced dynamical self-energy does not naturally give a suppression of the density of states at the Fermi level, namely a pseudogap, although it gives a ‘Fermi arc’ feature (discussed below). Therefore, the impact of any pseudogap on the NFL/FL behavior is not well captured here, and the result may depend on the specifics of the pseudogap physics one additionally invokes in the underdoped region. The present model however gives a good description of the normal state phenomena above the pseudogap temperature. Moreover, in the present model, there is a ‘Fermi arc’ due to strong suppression of the spectral weight at the antinodal points, see Fig. 2.6. However, the entire ‘Fermi arc’ remains coherent. In the angle-integrated density of states, no suppression of the spectral weight is obtained at the Fermi level. In other words, the ‘Fermi arc’ does not produce a pseudogap in the DOS. The doping dependence of the ‘Fermi arc’ is discussed in a separate work.[172] There is an increasing discussion that the pseudogap originates from some sort of a competing order, whose origin

is yet to be determined. Any competing order induced gap in the low-energy state may not affect much the NFL state. This is because the pseudogap is typically of the order of 50-80 meV, while the itinerant-local density fluctuations energy is 300-500 meV even at the optimal doping. Therefore, we expect that the pseudogap will have less influence on the NFL physics. Experimentally, the resistivity- T exponent is derived above the pseudogap temperature T^* .

2.8.6 Optical conductivity

Kubo formula works well in the weak-coupling region. Maki-Thomson (MT)[160], and later Aslamasov-Larkin (AL)[161] extended the calculations to include higher order diagrams. After deriving them, I will argue below that they can be neglected even in the intermediate coupling region of present interest. In the linear response theory, optical conductivity can be written as $\sigma_{xx}(\omega) = \frac{1}{\omega} \text{Im} \mathcal{K}_{xx}(\mathbf{q} \rightarrow 0, \omega)$, where \mathcal{K}_{xx} is the current-current correlation function. (This formula works when σ , and \mathcal{K} have no singularity). Here $\mathcal{K}_{xx}(\mathbf{q}, \tau) = i \langle T_\tau [j_x(\mathbf{q}, \tau), j_x(-\mathbf{q}, 0)] \rangle$, where $j_x(\mathbf{q}, \tau) = \sum_{\mathbf{k}, \sigma} v_x(\mathbf{k}) c_{\mathbf{k}, \sigma}^\dagger(\tau) c_{\mathbf{k}+\mathbf{q}, \sigma}(\tau)$ is the current operator. Substituting them, we get

$$\mathcal{K}_{xx}(\mathbf{q}, \tau) = \frac{C}{N} \sum_{\mathbf{k}, \mathbf{k}', \sigma, \sigma''} \langle T_\tau S(\infty) v_x(\mathbf{k}) v_x(\mathbf{k}') c_{\mathbf{k}+\mathbf{q}, \sigma}^\dagger(\tau) c_{\mathbf{k}, \sigma}(\tau) c_{\mathbf{k}'-\mathbf{q}, \sigma'}^\dagger(0) c_{\mathbf{k}', \sigma'}(0) \rangle, \quad (2.8.5)$$

where the constant factor $C = \frac{e^2}{\hbar^2}$. Onari *et al.*[165], and Bergeron *et al.*[174] have derived the explicitly the Kubo, MK and AL terms using diagram approach and the results hold for the MRDF approach. Following the same procedure as in Eqs. (A.2.4)-(A.2.6), we can arrive at the first three leading terms. The diagrams for the three terms are given in Fig. 2.3, and the

results are

$$\mathcal{K}^{\text{Kubo}}(\mathbf{q}, \epsilon_m) = \frac{C}{3N\beta} \sum_{\mathbf{k}} \mathbf{v}(\mathbf{k}) \cdot \Gamma(k, k+q) G(k) G(k+q), \quad (2.8.6)$$

$$\mathcal{K}^{\text{MT}}(\mathbf{q}, \epsilon_m) = \frac{C}{(N\beta)^2} \sum_{k, k'} \mathbf{v}(\mathbf{k}) \cdot \Gamma(k', k'+q) G(k) G(k+q) G^0(k') G^0(k'+q) V(k'-k), \quad (2.8.7)$$

$$\begin{aligned} \mathcal{K}^{\text{AL}}(\mathbf{q}, \epsilon_m) &= \frac{C}{(N\beta)^3} \sum_{k, k', q'} \mathbf{v}(\mathbf{k}) \cdot \Gamma(k', k'+q') G(k) G(k+q) G^0(k') G^0(k'+q) \\ &\times [G^0(k'+q'+q) + G^0(k'-q')] G^0(k+q'+q) V^{(2)}(q', q'+q). \end{aligned} \quad (2.8.8)$$

I continue to use the compact notation $k = (\mathbf{k}, i\omega_n)$, and $k+q = (\mathbf{k} + \mathbf{q}, i\omega_n - i\epsilon_m)$. $V = V_1 + V_2$ (spin+charge) is the total density fluctuation, and $V^{(2)}(q', q'+q) = V_1(q')V_1(q'+q) + V_2(q')V_2(q'+q)$. $\Gamma(k, k+q)$ is the current-current vertex. G^0 , and G correspond to the Green's function without and with self-energy correction, respectively. The corresponding diagrams are given in Fig.2.3. It is now easy to deduce that the MT and AL terms scale as V/\mathcal{W}^4 and V^2/\mathcal{W}^6 where V is the fluctuation potential which scales as U^2/\mathcal{W} . Therefore, as long as coupling strength $U \leq \mathcal{W}$ these terms have negligible contributions, except near the critical region where either V and/or the Green's function has a singular contribution. Since I am far away from any singular behavior, and I work in the intermediate coupling regime, I can neglect these high order terms.

Finally, using the spectral representation of the Green's function and performing the Matsubara frequency summation as in Eqs. (A.2.7)-(A.2.9), I arrive at a similar equation for the Kubo term

$$\begin{aligned} \mathcal{K}^{\text{Kubo}}(\mathbf{q}, \epsilon_m) &= \frac{C}{3N} \sum_{\mathbf{k}} \int_{-\infty}^{\infty} \int_{-\infty}^{\infty} \frac{d\omega_1}{2\pi} \frac{d\omega_2}{2\pi} A(\mathbf{k}, \omega_1) A(\mathbf{k} + \mathbf{q}, \omega_2) \\ &\times \mathbf{v}(\mathbf{k}) \cdot \Gamma(k, k+q) \frac{f(\omega_1) - f(\omega_2)}{i\epsilon_m - \omega_2 + \omega_1}. \end{aligned} \quad (2.8.9)$$

Now substituting for the bare current vertex as $\mathbf{v} = \Gamma^{(0)}$, and taking the limit of $\epsilon \rightarrow 0$, and $\mathbf{q} \rightarrow 0$, we obtain Eq. (2.5.1).

2.8.7 Vertex correction

Vertex correction is an important subject in the theories of strong correlation physics. Owing to the conservation laws, there always arise both density-density and current-current vertices in a homogeneous system. One often denotes both by the same symbol Γ , where a vector symbol Γ is used for the current vertex, and a scalar symbol Γ is used for the density vertex. In the present bubble diagrams for both density-density correlation functions χ , as well as current-current correlation function σ , the relevant vertex corrections are the three-point vertex functions, as shown by Bethe and Salpeter.[159] Thanks to the conservation laws, the density and current vertices are related to each other, as shown by Ward, and their relation is known as the Ward identity.[166]

In the following descriptions, I use four-component vertex Γ which encode the density and current vertices as $(\mathbf{\Gamma}, \Gamma)$. The Bethe-Salpeter vertex correction[159] is written by the self-consistent equations (see Fig. 2.3 for the relevant diagram)[187]:

$$\Gamma_\nu(k, k+q) = \Gamma^{(0)}(k, k+q) + \Gamma_\nu^{(1)}(k, k+q), \quad (2.8.10a)$$

$$\Gamma_\nu^{(1)}(k, k+q) = \frac{1}{\beta} \sum_{k', q'} V_\nu(k, k+q, k', k'+q) G(k') G(k'+q') \Gamma_\nu(k', k'+q), \quad (2.8.10b)$$

where $\nu = 1, 2$ are for spin and charge components, respectively. $\Gamma^{(0)}(k, k+q)$ is the four-component bare vertex, whose density component is $\Gamma^{(0)} = 1$. The current components are obtained as $\mathbf{q} \cdot \mathbf{\Gamma}^{(0)} = \xi_{k+q} - \xi_k$, where ξ_k is the bare electronic dispersion. $\Gamma_\nu^{(1)}(k, k+q)$ is the first order correction (see Fig. 2.3) to be evaluated self-consistently. Since both spin and charge densities are conserved here, one obtains the same Ward identity for them as

$$i\epsilon_m \Gamma_\nu(k, k+q) - \mathbf{q} \cdot \mathbf{\Gamma}_\nu(k, k+q) = G^{-1}(k+q) - G^{-1}(k). \quad (2.8.11)$$

Please note that in both Eqs. (2.8.10b), (2.8.11), the Green's function $G(k)$ is the full self-energy dressed Green's function, which remain the same in both spin and charge sectors. The current vertex does not directly contribute to the density-density correlation, and it is self-consistently related to the current vertex by the Ward identity. Therefore, in an ideal case,

one needs to solve Eqs. (2.8.10a), (2.8.10b), (2.8.11) inside the self-consistent cycles for the self-energy calculation.

Since vertex corrections often make the calculations computationally unmanageable, approximations are inevitable. The zeroth order rule is to make sure the the sum rule is maintained. However, the choice of a given approximation is usually determined by the type of fluctuations one is interested in as well as its region of validity. The simplest one is to neglect the vertex correction. Such an approximation is good enough for electron-phonon coupling (Midgal's theorem),[167] or in the single-shot GW method for electron-electron interactions. Omission of vertex correction can lead to violation of sum rule(s) when self-consistency is invoked.[182, 123] The next level approximation is to assume that the density and current vertices are proportional to each other, i.e., $\Gamma_\nu = \mathbf{q} \cdot \mathbf{\Gamma}_\nu / i\epsilon_m$ at all momenta and frequencies.[167] Such an approximation yields good result when the momentum dependence of the self-energy is weak as often used in DMFT calculations. However, this can lead to problems when the momentum dependence is significant, simply because the current vertex arises mainly from the momentum derivative of the self-energy.[167] A momentum and frequency dependent ratio function between the density and current vertices was introduced in the literature for the particle-hole bubble interactions[188, 187] as $\Gamma_\nu(k, k + q) = \mathbf{B}_\nu(k, k + q) \cdot \mathbf{\Gamma}_\nu(k, k + q)$. $\mathbf{B} = \mathbf{q}/i\epsilon_m$ in the above approximation. Altshuler, *et al.*[188] assumed that the current vertex along the dimension of motion is proportional to the density vertex, which means they ignored multiple scattering channels along the direction of the applied voltage. Takada[187] used the full ratio function, but assumed a local approximation for the potential V ($V(q)$ was replaced by its momentum averaged value), which is again suitable for weak k -dependent self-energy.

Eqs. (2.8.10a), (2.8.10b) are required to be solved for either the density or the current term, and then the other term can be evaluated by using the Ward identity (Eq. (2.8.11)). This is in fact the best strategy which guarantees that the conservation laws remain intact no matter what approximation is invoked in the calculations. I calculate the current vertex explicitly, and obtain the density vertex from the Ward identity.

For the susceptibility calculation, I assumed a local-field approximation. Therefore, I can make the same local-field approximation for the fluctuation-exchange potential V , i.e., I assume $V_\nu(k + q, k', k' + q) = V_\nu(k + q)\delta_{k,k'}$ (note that I invoked a local filed approximation

for both the momentum and frequency axes). Such an approximation should be relaxed when Umklapp scattering or any translational symmetry breaking field is present. From Eq. (A.2.11), I can write $V_\nu(k+q) = \frac{1}{\Gamma_\nu(k,k+q)} \frac{\delta\Sigma_\nu(k)}{\delta G(k+q)}$. Substituting this in Eq. (2.8.10b) gives

$$\Gamma_\nu^{(1)}(k, k+q) \approx G(k)\Sigma(k) \frac{\Gamma_\nu(k, k+q)}{\Gamma_\nu(k, k+q)}. \quad (2.8.12)$$

I define a function $u_\nu(k, k+q) = G(k+q)\Sigma_\nu(k)$. Then substituting this in Eq. (2.8.10a) gives

$$\Gamma_\nu^{(1)}(k, k+q) \approx \frac{u_\nu(k, k+q)/\Gamma_\nu(k, k+q)}{1 - u_\nu(k, k+q)/\Gamma_\nu(k, k+q)} \Gamma^{(0)}(k, k+q). \quad (2.8.13a)$$

$$\Gamma_\nu(k, k+q) \approx \frac{1}{1 - u_\nu(k, k+q)/\Gamma_\nu(k, k+q)} \Gamma^{(0)}(k, k+q). \quad (2.8.13b)$$

Substituting Green's function $G^{-1}(k) = i\omega_n - \xi_{\mathbf{k}} - \Sigma(k)$, in the Ward identity in Eq. (2.8.11), I obtain

$$\Gamma_\nu(k, k+q) = 1 - \frac{\Sigma(k+q) - \Sigma(k)}{i\epsilon_m} + \frac{\mathbf{q} \cdot \Gamma_\nu^{(1)}(k, p+q)}{i\epsilon_m}. \quad (2.8.14)$$

I define two symbols $m^*(k, k+q)/m_0 = 1 - (\Sigma(k+q) - \Sigma(k))/i\epsilon_m$, and $v(k, k+q) = \mathbf{q} \cdot \Gamma^{(0)}(k, p+q)/i\epsilon_m$. Then substituting Eq. (2.8.13b) in Eq. (2.8.14), I get

$$\Gamma = \frac{m^*}{m_0} + v \frac{u/\Gamma}{1 - u/\Gamma}, \quad (2.8.15)$$

where I have kept the k , and ν dependence on each term, except m_0 , implicit, for simplicity. Eq. (2.8.15) is an algebraic equation which can be solved to get

$$\Gamma = \frac{m^*/m_0 + u \pm \sqrt{(m^*/m_0 - u)^2 + 4uv}}{2}. \quad (2.8.16)$$

Eq. (2.8.16), and (2.8.11) can be solved in each self-consistent cycles to obtain both density

and current vertices.

If the self-energy is linear in frequency (FL-ansatz), and linear in momentum, I can further approximate the vertex corrections. Here I get

$$\frac{m_\nu(k, k+q)^*}{m_0} \approx Z^{-1}(k+q) - \frac{\mathbf{q}}{i\epsilon_m} \cdot \nabla_{\mathbf{k}} \Sigma(k), \quad (2.8.17)$$

and

$$\Gamma_\nu^{(1)}(k, k+q) \approx \nabla_{\mathbf{k}} \Sigma(k). \quad (2.8.18)$$

This reduces the density and current vertices as[167]

$$\Gamma_\nu(k, k+q) \approx m_\nu^*/m_0 = Z_\nu^{-1}(k+q), \quad (2.8.19a)$$

$$\begin{aligned} \Gamma_\nu^{(1)}(k, k+q) &\approx \Gamma_\nu^{(0)}(k, k+q) + \nabla_{\mathbf{k}} \Sigma(k) \\ &\approx -m_0 \nabla G^{-1}(\mathbf{k}, \omega). \end{aligned} \quad (2.8.19b)$$

2.9 Outlook and conclusions

The important message of my result is that for strongly anisotropic materials where the dynamical fluctuations have significant momentum dependence, the resistivity-temperature exponent is not a robust measure of the full correlation spectrum of the underlying quasiparticle states. I have found that even in the underdoped and overdoped regions, where resistivity exponent $n \rightarrow 2$, there are considerable amount of NFL self-energies lying in the antinodal regions. Similarly, in the extreme NFL region near the optimal doping regime (determined by $n \sim 1$), the nodal quasiparticles continue to behave FL-like (with $\Sigma'' \propto |\omega|^2$). Both as a function of temperature and doping (and other tunings), the spectral weight is transferred between the NFL and FL regions and the system adiabatically transforms from a dominant NFL to a FL-like state, as seen in experiments. This work suggests that the microscopic and macroscopic landscapes of the NFL behavior can be characteristically different and that a direct correspondence between k -resolved spectroscopy (such as ARPES, and quasiparticle interference (QPI) pattern) and the transport, and thermodynamical properties are necessary to deduce the global

and local NFL behavior of a given system.

Chapter 3

Wannier pairs in superconducting twisted bilayer graphene and related systems

3.1 Introduction

In this chapter, I look into the unconventional superconductivity in strongly correlated systems, which appears as a result of Moiré pattern formation. Unconventional superconductivity is well-studied in the context of cuprates, pnictides and heavy fermions. But, superconductivity in bilayer Moiré systems makes the field equally interesting. Most of the important characteristics of bilayer Moiré system come from interlayer interactions. And with increasing tunability of interlayer tunneling with twist angle, all the strongly correlated phenomena, including superconductivity, can be probed experimentally and can be studied theoretically with great variety. This may lead to a new understanding and discovery in the field of unconventional superconductivity. Here I study the spin fluctuation mediated superconductivity in single-layer graphene (SLG) and in Moiré pattern created by graphene on hexagonal Boron Nitride (GBN) and in twisted bilayer graphene (TBG). In GBN and TBG the superconducting pairing becomes complicated due to involvement of many lattice sites in a Moiré unit cell. This complexity is simplified by restricting within the flatbands and by considering the Wannier orbitals of the flat bands, which are localized at the Moiré lattice points. Thus in this study of superconductivity in Moiré systems, I propose an unconventional pairing between Wannier orbitals and predict the nature of pairing symmetries arising from such pairings.

Strongly correlated quantum phases and superconductivity have long been predicted in single-layer graphene (SLG) at the van-Hove singularity (VHS).[189] However, their experimental realization has so far remained elusive. Recently, both correlated insulating gap[190] and superconductivity [92] have been observed in a twisted bilayer graphene (TBG) at a narrow range of twist angles, namely the ‘magic’ angles $\sim 1^\circ$. In this region, the single-particle density of states (DOS) acquires a sharp peak near the Fermi level, with an effective bandwidth reducing to ~ 5 meV.[89, 191] The emergence of this flat band is intrinsic to the physics of Moiré pattern, formed in TBG as well as in graphene on hexagonal Boron Nitride (GBN).[89, 191, 192] The Moiré superlattice produces ‘cloned’ Dirac cones at the Moiré zone boundaries, in addition to the primary Dirac cone at the Moiré zone center. The band dispersion between the primary and cloned Dirac cones passes through saddle-points or VHSs, and hence yields a flat band. It is tempting to assume that the ‘magic’ angle creates a similar VHS-like state as in SLG and/or GBN, and thus the predicted correlated physics of SLG/GBN are also at play in TBG. However, a closer look at the electronic instabilities at the VHS and their characteristic localizations into unique Wannier states in the direct lattice reveals stark differences between them (see Fig. 3.1). This leads to an essential question: How do such Wannier states, enveloping many graphene unit cells, condensate into Cooper pairs?

The relationships between the k -space electronic structure and direct lattice localized Wannier states of the SLG, GBN, and TBG are delineated in Fig. 3.1. [I should caution the reader that Fig. 3.1 is only schematic and it denotes the localization of the flat bands in case of TBG and GBN. Although Wannier orbitals are not exactly same as local density of states \(LDOS\), still the LDOS gives an idea of the wave function localization. A more detailed description of the localization of the flat bands from ab initio calculation can be found in the Ref. \[192\].](#) The effective bandwidth of the VHS/flat band decreases from ~ 1 eV in SLG to ~ 100 meV in GBN to $\sim 3-5$ meV in TBG, making the latter more prone to correlation. Fermi surface (FS) of SLG, GBN, and TBG are compared in Fig. 3.1 at their corresponding VHS position. The FS of SLG is most flat (producing large nesting), while that for GBN is most circular (weak nesting), and TBG lies in between. In addition, we observe a systematic transition from six-fold to three-fold rotational symmetry in going from SLG to GBN to TBG, rearranging the corresponding Wannier states accordingly in the direct lattice. The three-fold symmetric FS of TBG is for

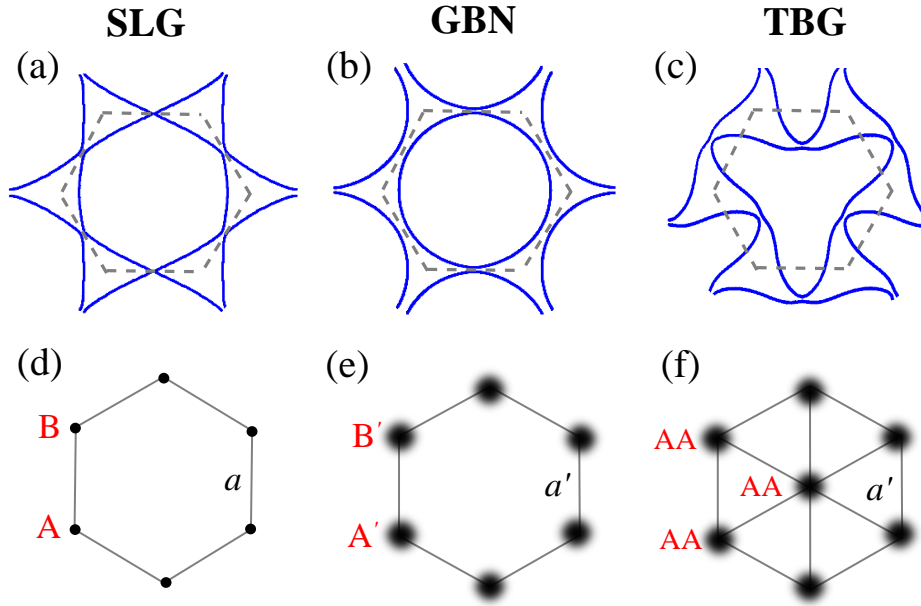


Figure 3.1: (a-c) Computed FSs of SLG, GBN, and TBG, respectively at their corresponding VHS energies (dashed line depicts the 1st BZ). (d-f) Corresponding positions of the Wannier states of the VHS/flat band in the direct lattice. For SLG [(a) and (d)], the VHS's Wannier states are localized on the 'A', and 'B' sublattices in the primitive unit cell. In GBN [(b) and (e)], the Wannier states are localized on the corners of the hexagonal Moiré-supercell. In TBG [(c) and (f)], the Wannier states show a fully formed triangular lattice at the flat band for *each valley*, where 'A' sublattices of the original two graphene lattices merge on top of each other (defined as 'AA' site). The Wannier states in both Moiré-lattices spread over several graphene unit cell. $a = 2.46\text{\AA}$ is the graphene's lattice constant, while a' is the Moiré lattice constant.

a given valley band, while the other valley band has the complementary three-fold symmetry so that the FS becomes six-fold symmetric when both valley bands are included.[193, 194] This *three-fold* symmetric FS makes TBG distinct from other hexagonal[189] and triangular lattices[195] with six-fold symmetric FS and plays an important role in stabilizing a distinct pairing symmetry here.

One of the most striking differences emerges when the corresponding Wannier states of individual flat band in the direct lattice are investigated, see Fig. 3.1(lower panel). In the flat region of the VHS in SLG near the \mathbf{K} -point, the states are localized on the 'A' sublattices, while the states near the \mathbf{K}' point are localized on the 'B'-sublattice and vice versa. In GBN and TBG, the situation changes drastically due to Moiré-supercell formation.* In the low-

*For SLG, the three nearest-neighbor (NN) distances for the pairings are[196] $\delta_{1,2} = (1, \pm\sqrt{3})a/2$, and $\delta_3 = (-1, 0)a$, where $a = 2.46\text{\AA}$ is the lattice constant. For GBN, the next nearest neighbor (NNN) sites are involved in pairing with odd-parity (as shown in Fig. 3.3), where the NNN positions (on both sides) are $\delta'_{1,2} =$

energy model of the GBN Moiré-lattice, the band structure can be described by that of a SLG under an effective supercell potential due to BN substrate with the supercell periodicity being much larger than the graphene unit cell. The corresponding Wannier states are maximally localized only on the corners of the hexagonal Moiré-supercell (enclosing several ‘A’ and ‘B’ sublattices of the original graphene unit cell),[191] see Fig. 3.1(e). On the contrary, in TBG the Wannier states of a given valley band are maximally localized on the ‘AA’ lattice sites (where ‘A’ sublattices of both graphene layers become aligned on top of each other) at all Moiré-supercell corners, as well as at the center, forming a full triangular symmetry,[190, 92, 197] see Fig. 3.1(f). The other valley band is also localized on the same ‘AA’ sites, forming a unit cell with *two Wannier orbitals per site*, with different orbitals possessing complementary rotational symmetry.[89, 191, 193, 194]

The pairing symmetry calculation is performed using materials specific, multiband Hubbard model. Hubbard model has a SC solution arising from the repulsive many-body pairing interaction which mediates unconventional, sign-reversal pairing symmetry.[198] Such a mechanism, often known as spin-fluctuation mediated unconventional superconductivity, basically depends on strong FS nesting instability at a preferred wavevector, say \mathbf{Q} . The nesting can promote a SC solution with a momentum-dependent pairing symmetry $\Delta_{\mathbf{k}}$ such that the pairing symmetry changes sign on the FS as: $\text{sgn}[\Delta_{\mathbf{k}}] = -\text{sgn}[\Delta_{\mathbf{k}+\mathbf{Q}}]$. This sign reversal is required to compensate for the positive (repulsive) pairing potential. This theory of spin-fluctuation driven superconductivity consistently links between the observed pairing symmetry and FS topology in many different unconventional superconductors.[199, 200, 201, 202] A \mathbf{k} -dependent pairing symmetry incipiently requires that pairing occurs between different atomic sites in the direct lattice. In what follows, the characteristic momentum structure of the pairing symmetry is intimately related to the underlying pairing mechanism, FS topology, and its contributing Wannier sites.

For each material, the non-interacting, low-energy band structures are obtained by tight-binding model in the unit cell or Moiré cell, as appropriate. Next I solve the pairing eigenvalue (SC coupling constant) and eigenfunction (pairing symmetry) solution of the linearized

($3, \pm\sqrt{3}$) $a'/2$, and $\delta'_3 = (0, -\sqrt{3})a'$, with $a' \sim 40a$ is the Moiré-lattice constant. For TBG, the triangular lattice sites have the NN distances (on both sides) as: $\delta_1 = (-1, 0)a'$, $\delta_{2,3} = (\pm 1, \sqrt{3})a'/2$, where the corresponding Moiré-lattice constant $a' \sim 40a$ near the magic angles

Eliashberg equation, where the pairing potential stems from many-body spin- and charge fluctuations.[199, 200, 201, 202] The obtained eigenfunction for the largest eigenvalue gives the pairing symmetry in the momentum space. The real-space mapping of the pairing symmetry is obtained by inverse Fourier transform. This illuminates the Cooper pairs between the nearest neighbor Wannier orbitals with corresponding phase factor.

In SLG, the computed pairing eigenfunction agrees with a $d + id$ -wave symmetry, which arises from inter-sublattice pairing between the ‘A’ and ‘B’ Wannier sites in a hexagonal primitive lattice. In GBN, the pairing solution changes to a $p + ip$ -symmetry where the inter-sublattice pairing occurs between the nearest neighbor (NN) Wannier orbitals with odd-parity phases. On the other hand, in TBG, we find an extended s - pairing with even parity phases between the same Wannier orbitals in NN sites. Note that the extended s -wave solution can produce accidental nodes when the FS is large near the VHS doping.

3.2 Model Hamiltonians for different systems

3.2.1 SLG

A tight-binding (TB) model is used for SLG taking into account nearest neighbour (NN) and the next nearest neighbour (NNN) hoppings. I start by describing the graphene lattice in terms of sublattices A and B with three NN translation vectors connecting sublattice A to three NN-sublattices B as $\delta_1 = (\frac{1}{2}, \frac{\sqrt{3}}{2})a_0$, $\delta_2 = (\frac{1}{2}, -\frac{\sqrt{3}}{2})a_0$, $\delta_3 = (-\frac{1}{2}, 0)a_0$ with a_0 denoting the carbon-carbon distance in graphene lattice. Six NNN translation lattice vectors can be written as $\mathbf{a}_1 = \pm(\delta_1 - \delta_2)$, $\mathbf{a}_2 = \pm(\delta_2 - \delta_3)$, $\mathbf{a}_3 = \pm(\delta_3 - \delta_1)$. We can write the Hamiltonian as

$$H_{\text{SLG}} = H_{\text{on-site}} + H_{\text{NN}} + H_{\text{NNN}} \quad (3.2.1)$$

where,

$$H_{\text{on-site}} = \sum_{i,\sigma} \epsilon_a a_{i,\sigma}^\dagger a_{i,\sigma} + \sum_{j,\sigma} \epsilon_b b_{j,\sigma}^\dagger b_{j,\sigma} \quad (3.2.2)$$

$$H_{\text{NN}} = -t \sum_{\langle i,j \rangle, \sigma} \left(a_{i,\sigma}^\dagger b_{j,\sigma} + h.c. \right) \quad (3.2.3)$$

$$H_{\text{NNN}} = -t' \sum_{\langle\langle i,j \rangle\rangle, \sigma} \left(a_{i,\sigma}^\dagger a_{j,\sigma} + b_{i,\sigma}^\dagger b_{j,\sigma} + h.c. \right) \quad (3.2.4)$$

with ϵ_a and ϵ_b are sublattice energies for sublattice A and B respectively, t and t' are nearest neighbour and next nearest neighbour hopping amplitude respectively, a^\dagger and b^\dagger are creation operators on sublattices A and B respectively. Next I Fourier transform the creation and annihilation operators to get the band dispersion as

$$H_{\text{on-site}} = \sum_{\mathbf{k}, \sigma} \left(\epsilon_a a_{\mathbf{k}, \sigma}^\dagger a_{\mathbf{k}, \sigma} + \epsilon_b b_{\mathbf{k}, \sigma}^\dagger b_{\mathbf{k}, \sigma} \right) \quad (3.2.5)$$

$$H_{\text{NN}} = \sum_{\mathbf{k}, \sigma} \left(\epsilon_{\mathbf{k}}^{\text{NN}} a_{\mathbf{k}, \sigma}^\dagger b_{\mathbf{k}, \sigma} + h.c. \right) \quad (3.2.6)$$

$$H_{\text{NNN}} = \sum_{\mathbf{k}, \sigma} \left(\epsilon_{\mathbf{k}}^{\text{NNN}} a_{\mathbf{k}, \sigma}^\dagger a_{\mathbf{k}, \sigma} + h.c. \right) \quad (3.2.7)$$

with

$$\epsilon_{\mathbf{k}}^{\text{NN}} = -t \sum_{i=1,2,3} e^{i\mathbf{k} \cdot \delta_i} \quad (3.2.8)$$

$$\epsilon_{\mathbf{k}}^{\text{NNN}} = -t \sum_{i,j(i \neq j)} e^{i\mathbf{k} \cdot (\delta_i - \delta_j)} \quad (3.2.9)$$

The model with more tight-binding parameters and their values is given in Ref. [203].

3.2.2 GBN

The low energy model for graphene on hBN is constructed by following Ref. [191]. The four-band model in terms of 2×2 blocks is given by

$$H_{\text{GBN}} = \begin{bmatrix} H_{\text{BN}} & T_{\text{BN,SLG}} \\ T_{\text{SLG,BN}} & H_{\text{SLG}} \end{bmatrix}, \quad (3.2.10)$$

where H_{BN} and H_{SLG} are Hamiltonians for Boron Nitride and SLG layers, respectively. $T_{\text{SLG,BN}}$, $T_{\text{BN,SLG}}$ are corresponding tunneling matrices in sublattice basis. The effective simplified model for this case is obtained by integrating out the boron nitride orbitals as $H = H_{\text{SLG}} - T_{\text{SLG,BN}}H_{\text{BN}}^{-1}T_{\text{BN,SLG}}$. Now the sublattice dependent terms in the Hamiltonian can be written as

$$H_{ss'} = H_{ss'}^0 + H_{ss'}^{\text{MB}}, \quad (3.2.11)$$

where $H_{ss'}^0$ is the Hamiltonian that describes Dirac cones and $H_{ss'}^{\text{MB}}$ gives the Moiré band modulation as

$$H_{ss'}^0 = H_{ss'}^0(\mathbf{k}, \mathbf{G} = 0)\delta_{\mathbf{k},\mathbf{k}'}, \quad (3.2.12)$$

$$H_{ss'}^{\text{MB}} = \sum_{\mathbf{G} \neq 0} H_{ss'}^{\text{MB}}(\mathbf{k}, \mathbf{G})\delta_{\mathbf{k}'-\mathbf{k}-\mathbf{G}}. \quad (3.2.13)$$

All the terms of the effective Hamiltonian now can be determined by the following equations

$$H_0 = C_0 e^{i\phi_0}, \quad H_z = C_z e^{i\phi_z}, \quad (3.2.14)$$

$$H_{\text{AA}} = H_0 + H_z, \quad H_{\text{BB}} = H_0 - H_z, \quad (3.2.15)$$

$$H_{\text{AB},\mathbf{G}_1} = H_{\text{AB},\mathbf{G}_4}^* = C_{\text{AB}} e^{i(2\pi/3-\phi_{\text{AB}})}, \quad (3.2.16)$$

$$H_{\text{AB},\mathbf{G}_3} = H_{\text{AB},\mathbf{G}_2}^* = C_{\text{AB}} e^{-i\phi_{\text{AB}}}, \quad (3.2.17)$$

$$H_{\text{AB},\mathbf{G}_5} = H_{\text{AB},\mathbf{G}_6}^* = C_{\text{AB}} e^{i(-2\pi/3-\phi_{\text{AB}})}. \quad (3.2.18)$$

In Ref. [191], it is shown that this effective model can be completely specified by six numbers $C_0 = -10.13$ meV, $\phi_0 = 86.53^\circ$, $C_z = -9.01$ meV, $\phi_z = 8.43^\circ$, $C_{\text{AB}} = -11.34$ meV, $\phi_{\text{AB}} = 19.60^\circ$.

3.2.3 TBG

The Hamiltonian for the TBG is constructed by following the work of Bistritzer and MacDonald [89]. The low-energy Hamiltonian can be written by considering two SLGs which were rotated by an angle θ with respect to each other and tunneling between the SLG layers (see

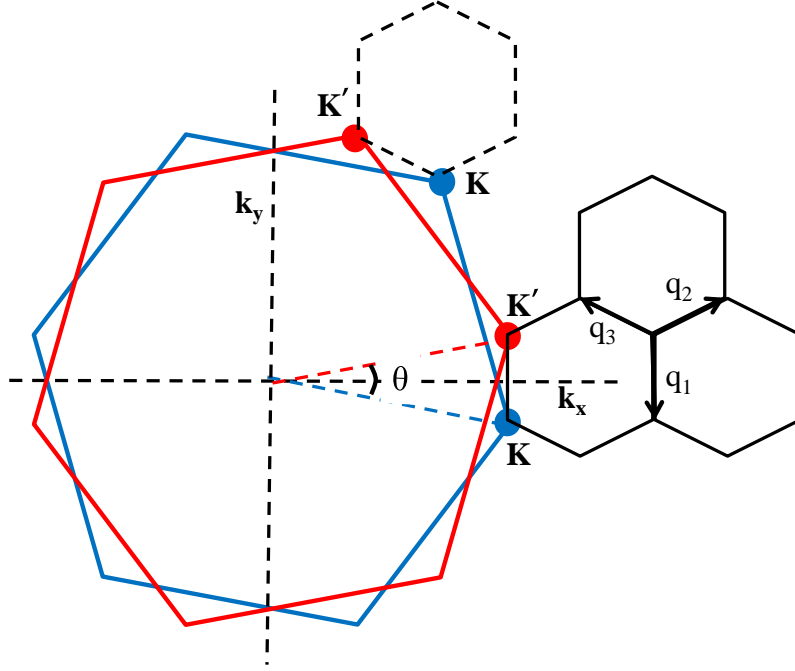


Figure 3.2: Momentum-space formulation of TBG Moiré pattern. Red and blue BZ of SLG denotes the upper and lower layer, respectively. The upper layer is rotated by an angle $\theta/2$ and lower layer by $-\theta/2$ with respect to the k_x, k_y axis shown in the figure. Smaller (solid black) hexagons represent the Moiré BZ of the TBG for a given valley state. Dashed black hexagon represents the Moiré BZ for the other valley state.

Fig. 3.2). Low-energy continuum model Hamiltonian for SLG can be written in a 2×2 matrix as

$$h_{\mathbf{k}}(\theta) = -vk \begin{bmatrix} 0 & e^{i(\phi_{\mathbf{k}} - \theta)} \\ e^{i(\phi_{\mathbf{k}} - \theta)} & 0 \end{bmatrix}, \quad (3.2.19)$$

where $v = 3.2 \text{ eV}\text{\AA}^{-1}$ is the Dirac velocity, \mathbf{k} is the momentum measured from Dirac point, and $\phi_{\mathbf{k}} = \tan(k_y/k_x)$, and θ is twist angle [see Fig. 3.2]. Next we consider the inter-layer hopping integrals, which can be accurately described by three distinct tunnelings with three distinct wavevectors \mathbf{q}_j ($j = 1, 2, 3$) [see Fig. 3.2], whose directions are given by $(0, -1)$ for $j = 1$, $(\sqrt{3}/2, 1/2)$ for $j = 2$, and $(-\sqrt{3}/2, 1/2)$ for $j = 3$. The magnitude is $|\mathbf{q}_j| = 2k_D \sin(\theta/2)$ where k_D is the magnitude of BZ corner wavevector for a SLG. Corresponding tunneling

matrices T_j are given by

$$T_1 = c \begin{bmatrix} 1 & 1 \\ 1 & 1 \end{bmatrix}, \quad T_2 = c \begin{bmatrix} e^{-i\zeta} & 1 \\ e^{i\zeta} & e^{-i\zeta} \end{bmatrix}, \quad T_3 = c \begin{bmatrix} e^{i\zeta} & 1 \\ e^{-i\zeta} & e^{i\zeta} \end{bmatrix}, \quad (3.2.20)$$

where $\zeta = 2\pi/3$ and $c = 0.9$ eV is the inter-layer tunneling amplitude. The \mathbf{k} -cutoff is chosen in the first Moiré pattern BZ given by reciprocal lattice vectors $G_1 = |\mathbf{q}_j|(\sqrt{3}, 0)$ and $G_2 = |\mathbf{q}_j|(-\sqrt{3}/2, 3/2)$. Now the Hamiltonian for TBG is a 8×8 matrix given by

$$H_{\mathbf{k}} = \begin{bmatrix} h_{\mathbf{k}}(\theta/2) & T_1 & T_2 & T_3 \\ T_1^\dagger & h_{\mathbf{q}_1}(-\theta/2) & 0 & 0 \\ T_2^\dagger & 0 & h_{\mathbf{q}_2}(-\theta/2) & 0 \\ T_3^\dagger & 0 & 0 & h_{\mathbf{q}_3}(-\theta/2) \end{bmatrix}. \quad (3.2.21)$$

In this calculation \mathbf{k} -points beyond the first shell approximation is considered, which results in a 400×400 matrix. After diagonalizing this matrix, I downfold the eigenvalues to the two (four) low-energy flat bands for a single valley (both valleys) that are near the FS, and all the subsequent calculations are performed considering only these bands.

3.3 Electronic structure and FS nestings

As presented in the last section, I use a typical two band tight-binding (TB) model [196, 203] for SLG. And for the Moiré-lattices in GBN and TBG, I directly use the low energy model. In Fig. 3.1 (top panel), I show the computed FS topology for the three systems under study with the chemical potential placed at the VHS/flat band. In the corresponding lower-panel of Fig. 3.1, I show the Wannier states for the Fermi momenta on the flat band.

To estimate the FS nesting features, and the corresponding pairing potential, the multiband

Lindhard susceptibility $\chi_{\alpha\beta}(\mathbf{q}, \omega)$ is computed as:

$$\chi_{\alpha\beta}(\omega, \mathbf{q}) = - \sum_{\mathbf{k}} F_{\nu\nu'}^{\alpha\beta}(\mathbf{k}, \mathbf{q}) \frac{f(\epsilon_{\mathbf{k}}^{\nu}) - f(\epsilon_{\mathbf{k}+\mathbf{q}}^{\nu'})}{\omega + i\delta - \epsilon_{\mathbf{k}}^{\nu} + \epsilon_{\mathbf{k}+\mathbf{q}}^{\nu'}}, \quad (3.3.1)$$

where $\xi_{\mathbf{k}}^{\nu}$ is the ν^{th} band, and $f(\xi_{\mathbf{k}}^{\nu})$ is the corresponding fermion occupation number. α, β give the orbital indices, and \mathbf{q} and ω are the momentum and frequency transfer, respectively. $F_{\mathbf{k},\mathbf{q}}$ as form factor arising from the eigenvectors as

$$F_{\nu\nu'}^{\alpha\beta}(\mathbf{k}, \mathbf{q}) = u_{\alpha}^{\nu\dagger}(\mathbf{k}) u_{\beta}^{\nu}(\mathbf{k}) u_{\beta}^{\nu'\dagger}(\mathbf{k} + \mathbf{q}) u_{\alpha}^{\nu'}(\mathbf{k} + \mathbf{q}), \quad (3.3.2)$$

where u_{α}^{ν} represents the eigenvector for the ν^{th} -band projected to the α^{th} basis (Wannier orbitals). The form-factor is evaluated numerically.*

The 2D profile of the susceptibility (total $\chi = \sum_{\alpha\beta} \chi_{\alpha\beta}$) for $\omega \rightarrow 0$ is presented in Fig. 3.3 (top panel) for all three systems. I find stark differences in the nesting features. In SLG, the FS is extremely flat, causing paramount FS nesting at $\mathbf{Q} \sim (2/3, 1/3)$ r.l.u., and its equivalent points. The nesting is considerably weak in GBN since here the FS is quite circular, with some residual nesting occurring at small wavevectors. For TBG, the nesting is strong at $\mathbf{Q} \sim (1/3, 0)$ r.l.u.. Such a FS nesting drives translation symmetry breaking into various density-wave orders in the particle-hole channels and/or unconventional pairing instability. The FS nesting driven superconductivity stabilizes a characteristic symmetry which changes sign on the FS.

3.4 Pairing potential calculation

I start with an extended Hubbard model with both the valleys:

$$\begin{aligned} H_{\text{int}} &= \sum_{\alpha\beta, \sigma\sigma', \mathbf{q}} U_{\alpha\beta} n_{\alpha\sigma}(\mathbf{q}) n_{\beta\sigma'}(-\mathbf{q}) \\ &= U \sum_{\alpha, \mathbf{k}, \mathbf{k}', \mathbf{q}} c_{\mathbf{k}\alpha\uparrow}^{\dagger} c_{\mathbf{k}+\mathbf{q}\alpha\uparrow} c_{\mathbf{k}'\alpha\downarrow}^{\dagger} c_{\mathbf{k}'-\mathbf{q}\alpha\downarrow} + V \sum_{\alpha \neq \beta, \mathbf{k}, \mathbf{k}', \mathbf{q}, \sigma, \sigma'} c_{\mathbf{k}\alpha\sigma}^{\dagger} c_{\mathbf{k}+\mathbf{q}\alpha\sigma} c_{\mathbf{k}'\beta\sigma'}^{\dagger} c_{\mathbf{k}'-\mathbf{q}\beta\sigma'}, \end{aligned} \quad (3.4.1)$$

*For simple two-band tight-binding model of SLG, F can be evaluated analytically by substituting the analytical form of the eigenvectors, yielding $F_{\nu\nu'}^{\alpha\beta}(\mathbf{k}, \mathbf{q}) = (1 + \nu\nu' \cos \theta)$, where $\nu, \nu' = \pm 1$ for the two bands, and θ is the angle between \mathbf{k} , and $\mathbf{k} + \mathbf{q}$. [204, 205]

where α and β are valley indices, taking values of 1 and 2 for two valleys in TBG. c^\dagger and c are creation and annihilation operators, respectively. U and V are intra-valley and inter-valley coupling strength respectively. In Eq. 3.4.1 first term is the intra-valley interaction and second term is inter-valley interaction. By expanding Eq. 3.4.1 to include multiple-interaction channels, we obtain the effective pairing potential $\Gamma_{\alpha\beta}(\mathbf{k} - \mathbf{k}')$ for the singlet and triplet states. The corresponding pairing Hamiltonian is

$$H_{\text{int}} \approx \sum_{\alpha\beta, \mathbf{k}, \mathbf{k}', \sigma, \sigma'} \Gamma_{\alpha\beta}(\mathbf{k} - \mathbf{k}') c_{\mathbf{k}\alpha\sigma}^\dagger c_{-\mathbf{k}\alpha\sigma'}^\dagger c_{-\mathbf{k}'\beta\sigma'} c_{\mathbf{k}'\beta\sigma}. \quad (3.4.2)$$

The pairing potentials are

$$\tilde{\Gamma}_{\alpha\beta}^s(\mathbf{q}) = \frac{1}{2} \text{Re} [3\tilde{U}^s \tilde{\chi}_{\alpha\beta}^s(\mathbf{q}) \tilde{U}^s - \tilde{U}^c \tilde{\chi}_{\alpha\beta}^c(\mathbf{q}) \tilde{U}^c + \tilde{U}^s + \tilde{U}^c], \quad (3.4.3)$$

$$\tilde{\Gamma}_{\alpha\beta}^t(\mathbf{q}) = -\frac{1}{2} \text{Re} [\tilde{U}^s \tilde{\chi}_{\alpha\beta}^s(\mathbf{q}) \tilde{U}^s + \tilde{U}^c \tilde{\chi}_{\alpha\beta}^c(\mathbf{q}) \tilde{U}^c - \tilde{U}^s - \tilde{U}^c]. \quad (3.4.4)$$

Here $U^{s/c} = U$ for $\alpha = \beta$ and $U^{s/c} = V$ for $\alpha \neq \beta$. From the superconducting Hamiltonian Eq. 3.4.2, we can construct the superconducting gap (SC) equation as

$$\Delta_{n,\mathbf{k}}^\alpha = - \sum_{\beta, \mathbf{k}'} \Gamma_{\alpha\beta}^n(\mathbf{k} - \mathbf{k}') \langle c_{-\mathbf{k}'\beta\sigma} c_{\mathbf{k}'\beta\sigma'} \rangle \quad (3.4.5)$$

Here $n = s, t$ for singlet and triplet pairing channels where $\sigma' = \mp\sigma$, respectively. In the limit $T \rightarrow T_c$ we have $\langle c_{-\mathbf{k}'\beta\sigma} c_{\mathbf{k}'\beta\sigma'} \rangle \rightarrow \lambda_n \Delta_{n,\mathbf{k}'}^\beta$ which makes the above equation an eigenvalue equation

$$\Delta_{n\mathbf{k}}^\alpha = -\lambda \sum_{\beta, \mathbf{k}'} \Gamma_{\alpha\beta}^n(\mathbf{k} - \mathbf{k}') \Delta_{n,\mathbf{k}'}^\beta. \quad (3.4.6)$$

The eigenvalue problem is solved separately for the singlet and triplet channels. The following equations remain the same for both these pairing channels and thus the index 'n' is omitted for simplicity. To obtain the pairing symmetry, I focus on the k-points only on the FS. This is justified since at low temperature quasiparticles near the FS contribute to the formation of Cooper pairs. Then this is an eigenvalue equation for the k-points on the Fermi surface ($\Delta_{\mathbf{k}_F}^\alpha$). For this purpose the matrix can be constructed as

$$\Gamma(\mathbf{k}_F - \mathbf{k}'_F) = \begin{bmatrix} \Gamma_{\mathbf{k}_F \mathbf{k}'_F}^{11} & \Gamma_{\mathbf{k}_F \mathbf{k}'_F}^{12} & \cdots \\ \Gamma_{\mathbf{k}_F \mathbf{k}'_F}^{21} & \Gamma_{\mathbf{k}_F \mathbf{k}'_F}^{22} & \cdots \\ \vdots & \vdots & \ddots \end{bmatrix}, \quad (3.4.7)$$

where 1 and 2 refer to the band and valley indices, and $\mathbf{q} = \mathbf{k}_F - \mathbf{k}'_F$ the Fermi surface nesting vector and $\Gamma_{\mathbf{k}_F \mathbf{k}'_F}^{\alpha\beta}$ refers to $N \times N$ matrix if N number of points on the Fermi surface is considered for each valley. Now if I denote $\Delta_{\mathbf{k}_F} = [\Delta_{\mathbf{k}_F}^1 \quad \Delta_{\mathbf{k}_F}^2]^T$ then I can write the matrix equation and solve for its eigenvalues and eigenvectors as

$$\Delta_{\mathbf{k}_F} = -\lambda \sum_{\mathbf{k}'_F} \Gamma(\mathbf{k}_F - \mathbf{k}'_F) \Delta_{\mathbf{k}'_F}. \quad (3.4.8)$$

By writing the SC gap function as $\Delta_{\mathbf{k}} = \Delta_0 g_{\mathbf{k}}$, where Δ_0 is the gap amplitude and $g_{\mathbf{k}}$ is the gap anisotropy, momentum variation of the pairing symmetry ($g_{\mathbf{k}}$) can be obtained in the form of Eq. (3.5.5).

3.5 Pairing symmetry calculations

Next I compute the pairing symmetry and pairing strength arising from the density-density fluctuations. It should be noted that although the bandwidth is lower near the magic angles, the FS becomes large at the VHS point. This enhances screening, and hence the effective Coulomb interaction is reduced.[206] The largest insulating gap obtained near half-filling in TBG is ~ 0.3 meV $<$ bandwidth, rendering an effective weak or intermediate coupling regime for correlation. For such a correlation strength, the many-body density-density (spin and charge) correlation functions are computed from multiband Hubbard model. Since the doping range

is restricted to only within individual flat bands, the corresponding intra-band Hubbard U dominate the correlation spectrum. The multiband Hubbard interaction reads as

$$H_{int} = \frac{1}{\Omega_{\text{BZ}}} \sum_{\alpha\alpha'} U_{\alpha\beta} \sum_{\mathbf{q}, \sigma\sigma'} n_{\alpha\sigma}(\mathbf{q}) n_{\beta\sigma'}(-\mathbf{q}), \quad (3.5.1)$$

where $n_{\alpha\sigma}(\mathbf{q})$ is the density operator for the α^{th} -band with $\sigma = \uparrow, \downarrow$ spins, and $U_{\alpha\beta}$ is the Hubbard U between the two bands. Based on this Hubbard model, the pairing potential is computed from the bubble and ladder diagrams to obtain for singlet and triplet channels as[199, 200, 201, 202]

$$\tilde{\Gamma}^s(\mathbf{q}) = \frac{1}{2} \text{Re} [3\tilde{U}_s \tilde{\chi}^s(\mathbf{q}) \tilde{U}_s - \tilde{U}^c \tilde{\chi}^c(\mathbf{q}) \tilde{U}_c + \tilde{U}_s + \tilde{U}_c], \quad (3.5.2)$$

$$\tilde{\Gamma}^t(\mathbf{q}) = -\frac{1}{2} \text{Re} [\tilde{U}_s \tilde{\chi}^s(\mathbf{q}) \tilde{U}_s + \tilde{U}_c \tilde{\chi}^c(\mathbf{q}) \tilde{U}_c - \tilde{U}_s - \tilde{U}_c]. \quad (3.5.3)$$

Here I introduce ‘tilde’ to symbolize a quantity to be a matrix of dimension $N \times N$, with N being the total number of bands. Superscript ‘s’, and ‘c’ denote many-body spin and charge susceptibilities $\tilde{\chi}^{s/c}(\mathbf{q})$ matrix whose components are defined as

$$\chi_{\alpha\beta}^{s/c} = \chi_{\alpha\beta} (1 \mp U_{\alpha\beta}^{s/c} \chi_{\alpha\beta})^{-1}. \quad (3.5.4)$$

Here $\chi_{\alpha\beta}$ is the bare susceptibility defined in Eq. (3.3.1) above. The many-body susceptibilities are obtained within the random phase approximation (RPA). $U_{s/c}$ are the Hubbard U matrix for spin-flip and non spin-flip interactions, respectively (Eq. (3.5.1)). Here $U_{\alpha\beta}^{s/c} = U$ for $\alpha = \beta$ and $U_{\alpha\beta}^{s/c} = V$ for $\alpha \neq \beta$. **The valley indices are not explicitly mentioned in Eq. (3.5.2) for simplicity. One can construct the valley dependent $\Gamma_{\alpha\beta}$ by considering valley dependent $U_{\alpha\beta}$ and U differs in different systems.*** Clearly, larger U increases (decreases) spin (charge) susceptibility. Essentially in moderate coupling regime, spin-fluctuation dominates while charge sector acts as pair-breaker for the spin-singlet pairing (Γ^s in Eq. (3.5.2)).

A triplet pairing channel Γ^t increases when the onsite interaction dominates over spin and

*The onsite Hubbard interaction becomes materials dependent due to varying screening effects, as evident in Fig. 3.3, and also shown in Ref.[206]. We use materials dependent Hubbard U (same for all bands): $U = 1$ eV for SLG, 100 meV for GBN, and 3 meV for TBG. For TBG the insulating gap is $\sim 0.3\text{meV} < U$. This can be reconciled for a dispersive Hubbard band within the Mott picture or for the Slater picture where the gap is U times order parameter.

charge fluctuations, as in the case of GBN (see below). In both singlet and triplet cases, it is evident that the pairing potentials have strong peaks at the momenta where the underlying susceptibility itself obtains peaks, i.e., pairing potentials $\Gamma^{s/t}(\mathbf{q})$ also diverge at the FS nesting wavevectors, and hence stabilize a characteristic pairing symmetry in a given system.

Based on the above pairing potential, we solve the linearized multiband SC gap equation, which is the pairing eigenvalue equation, as given by (see the previous section for details)

$$\lambda_\nu g_\nu(\mathbf{k}_\alpha) = -\frac{1}{\Omega_{\text{FS}}} \sum_{\beta, \mathbf{k}'_\beta} \Gamma_{\alpha\beta}^\nu(\mathbf{k}_\alpha - \mathbf{k}'_\beta) g_\nu(\mathbf{k}'_\beta), \quad (3.5.5)$$

where \mathbf{k}_α is the Fermi momentum for the α^{th} band. The eigenvalue calculation is performed over the entire 2D FS to estimate the dominant eigenvalue λ (which measures the SC coupling constant), and the corresponding eigenvector gives the leading pairing symmetry $g(\mathbf{k})$. The same eigenvalue equation is solved for both singlet ($\nu \equiv s$) and triplet ($\nu \equiv t$) channels. Since the pairing potentials $\Gamma^{s/t}$ scale with the Hubbard U , SC coupling constant λ also increases with increasing U . Within the first-order approximation, the pairing symmetry $g(\mathbf{k})$ does not scale with U (in the weak to moderate coupling regime). Therefore, the general conclusions about the pairing symmetry, and the phase diagram are dictated by the nesting strength, and remain valid for different values of U in this coupling regime.

For a repulsive interaction $\Gamma^\nu > 0$, according to Eq.(3.5.5), a positive eigenvalue λ can commence with the corresponding eigenfunction $g(\mathbf{k})$ changing sign as $\text{sgn}[g(\mathbf{k})] = -\text{sgn}[g(\mathbf{k}')]$ mediated by strong peak(s) in Γ^ν at $\mathbf{Q} = \mathbf{k} - \mathbf{k}'$. Looking into the origin of Γ^ν in Eqs. (3.5.2), (3.5.3) reveals that Γ^ν inherits strong peaks from that in $\chi^{s/c}$.

3.6 Results

Here I discuss the results of the pairing eigenstates for three systems under considerations at their VHS dopings. The computed results of $g(\mathbf{k})$ for the largest eigenvalue of Eq. (3.5.5) are shown in the middle panel in Fig. 3.3. The momentum space symmetry of the eigenfunction $g(\mathbf{k})$ is obtained by comparing with the orbital symmetry of the spherical harmonics. After

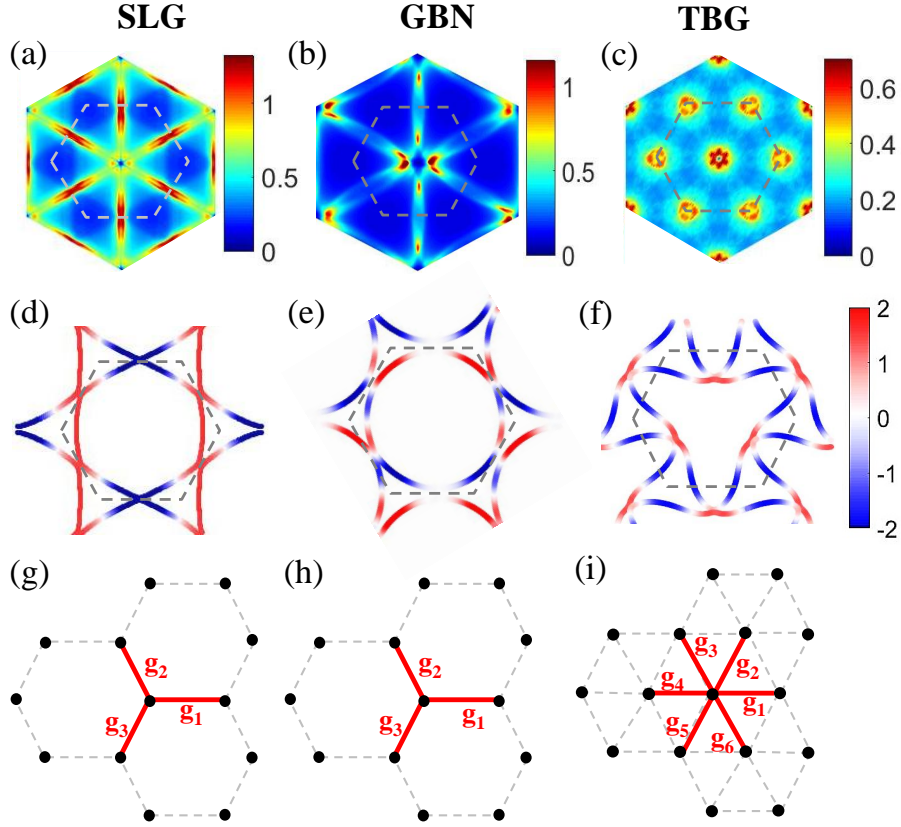


Figure 3.3: (a-c) Spin susceptibility within RPA approximation for (a) SLG, (b) GBN and (c) TBG. (d-f) Computed pairing eigenfunctions for the highest eigenvalue of Eq. (3.5.5) for (d) SLG, (e) GBN and (f) TBG at their VHS dopings are plotted on the FS in a blue (negative) to white (nodes) to red (positive) colormap. The pairing structure is consistent with a $d + id$ -wave and $p + ip$ -wave symmetry in SLG, and GBN, respectively. On the other hand for TBG in (f) we find a rotationally invariant extended s -wave symmetry. (g-i) The real space picture of the pairing for (g) SLG, (h) GBN and (i) TBG systems. g_j denote the pairing strength between nearest sites which is obtained from Fourier transformation of corresponding pairing functions [Eq. (3.6.1)].

that I inverse Fourier transform the $g(\mathbf{k})$ to the unit cell/Moire supercell as

$$g_j = \frac{1}{\Omega_{\text{BZ}}} \sum_{\mathbf{k}} g(\mathbf{k}) e^{-i(\mathbf{k} \cdot \delta_j - \phi_{\mathbf{k}})}, \quad (3.6.1)$$

where g_j gives the pairing amplitude between two Wannier sites separated by a distance δ_j , see Fig. 3.3(g-i). $\phi_{\mathbf{k}} = \text{Arg}[\sum_j e^{-i\mathbf{k} \cdot \delta_j}]$ is an additional phase factor arising in the hexagonal lattice possessing two Wannier basis per unit cell.[207] I discuss below each system separately.

3.6.1 SLG

For SLG, numerous calculations predicted that an exotic $d_{x^2-y^2} + id_{xy}$ ($d + id$) - wave symmetry is the dominant pairing channel, constrained by the FS nesting at the VHS.[189] I also find here that the two highest eigenvalues are the same with $\lambda = 0.26$ with the corresponding degenerate eigenfunctions being

$$\begin{aligned} g^{d_{x^2-y^2}}(\mathbf{k}) &= \cos(k_y - \phi_{\mathbf{k}}) + \cos\left(\frac{k_y}{2} + \phi_{\mathbf{k}}\right) \cos\left(\frac{\sqrt{3}k_x}{2}\right), \\ g^{d_{xy}}(\mathbf{k}) &= \sin\left(\frac{k_y}{2} + \phi_{\mathbf{k}}\right) \sin\left(\frac{\sqrt{3}k_x}{2}\right). \end{aligned} \quad (3.6.2)$$

These two eigenfunctions, respectively, represent $d_{x^2-y^2}$ and d_{xy} symmetries in the hexagonal BZ. Pairing symmetry can be deduced by looking at the irreducible representations of the symmetry group of the normal-state Hamiltonian. Here, the hexagonal group D_{6h} can be expanded with the E_{2g} irreducible representation ($d_{x^2-y^2}$ and d_{xy} solutions). In general, any linear combination gives a valid solution because of the degeneracy. However, the quasiparticle energy $E(\mathbf{k}) = \sqrt{\epsilon(\mathbf{k})^2 + |\Delta(\mathbf{k})|^2}$ favours $\Delta(\mathbf{k})$ to have as few nodes as possible on the normal-state Fermi surface $\epsilon(\mathbf{k}) = 0$ because it is energetically favoured. It can be shown that a complex combination of the basis functions ($d_{x^2-y^2}$ and d_{xy} solutions) are usually favoured as it fully gaps the quasiparticle spectrum on the Fermi surface and thus minimizes the free energy.[207] This gives a $d + id$ -pairing symmetry in SLG.[208] (I repeat the calculation with different U , the absolute value of the eigenvalue changes, but the eigenfunctions remain the same). Fig. 3.3(d) shows the $d_{x^2-y^2}$ eigenfunction, overlaid on the corresponding FS a color-gradient scale. Using Eq. (3.6.1), I obtain pairing amplitude between three nearest-neighbors to be $g_{1,2,3} = (2, -1, -1)$ for $d_{x^2-y^2}$ case, and $g_{1,2,3} = (0, 1, -1)$ for the d_{xy} pairing state (as shown in Fig. 3.3(g)). The result establishes that the $d + id$ -pairing state in SLG at the VHS occurs between the NN sublattices with characteristic phases, which accommodate the FS nesting features and corresponding sign-reversal in the gap structure.

3.6.2 GBN

In GBN, the circular FS allows small-angle nestings, and hence triplet pairing channel gains dominance, as in Sr_2RuO_4 [209] and UPt_3 [210]. With similar argument given in the previous section, an odd-parity $p + ip$ wave pairing is favoured as shown in Fig. 3.3(e). The symmetry belongs to the E_1 representation with two degenerate eigenfunctions[208]:

$$\begin{aligned} g^{p_x}(\mathbf{k}) &= \sin(k_y - \phi_{\mathbf{k}}) + \sin\left(\frac{k_y}{2} + \phi_{\mathbf{k}}\right) \cos\left(\frac{\sqrt{3}k_x}{2}\right), \\ g^{p_y}(\mathbf{k}) &= \cos\left(\frac{k_y}{2} + \phi_{\mathbf{k}}\right) \sin\left(\frac{\sqrt{3}k_x}{2}\right). \end{aligned} \quad (3.6.3)$$

Compared to the other two compounds, a considerably lower value of $\lambda = 0.03$ is found in GBN. This is expected since this system does not have a strong nesting at a single wavevector, rather small-angle scattering wavevectors with lower strength. The inverse Fourier transformation of the pairing state yields $g_{1,2,3} = (2i, -i, -i)$ for the p_y state and $g_{1,2,3} = (0, i, -i)$ for the p_x state for the three NN Wannier sites (as shown in Fig. 3.3(h)). Both $d + id$ - symmetry in SLG and $p + ip$ - wave pairing in GBN break time-reversal symmetry, and are chiral and nodeless in nature.

3.6.3 TBG

There have already been several proposals for unconventional pairing symmetries, and pairing mechanisms in TBG, such as $d + id$ [211, 194] as in SLG, odd-parity $p + ip$ [212], and others[213]. The FS topology is quite different in TBG, exhibiting a three-fold symmetry for each valley. The three-fold symmetric FS is different from other triangular lattices with six-fold symmetric FS.[195] This FS topological change plays an important role in governing a distinct pairing symmetry in TBG. Here an extended s -wave pairing is obtained as shown in Fig. 3.3(f), with its functional form given by

$$g^{\text{ext-s}}(\mathbf{k}) = 2 \cos(\sqrt{3}k_x/2) \cos(k_y/2) + \cos(k_y). \quad (3.6.4)$$

The pairing function is rotationally symmetric and changes sign between the Moiré-zone center and corners, governing a symmetry that is consistent with the A_{2g} -group and hence called

extended s -wave pairing. For the large FS at the VHS doping, the tip of the FS crosses through the nodal lines and thus gapless SC quasiparticle are obtained in this pairing state. This is a purely *real* gap function. In the direct Moiré-lattice, this pairing symmetry stems from a nearest neighbor pairing between the Wannier sites in a triangular lattice given by $g_{1-6} = 1$ for all components, see Fig. 3.3(i).

Please note that the computed pairing symmetry in TBG is different from that of the other triangular lattices, such as $\text{Na}_x\text{CoO}_2 \cdot y\text{H}_2\text{O}$ (NCOHO).[195] This is because the FS of NCOHO has the six-fold symmetry, while the FS for a given valley in TBG has three-fold symmetry.

Valley dependent pairing symmetry in TBG

I repeat the calculation for the pairing eigenvalue and eigenfunctions by including both valley states for TBG. The FS for the two valleys are mutually rotated to each other by π . This changes the symmetry of the TBG lattice from triangular to hexagonal, as seen from the FS in Fig. 3.4(d-f). This opens up two competing nesting wavevectors – intra-band and inter-band nestings – as captured in the susceptibility result, see Fig. 3.4(a-c). The details of the pairing symmetry are analyzed in the three limiting cases of (i) intra-valley interaction $U = 3.5$ meV, inter-valley $V \rightarrow 0$, (ii) $U \rightarrow 0$, $V = 3.5$ meV, and (iii) $U = V = 3.5$ meV. In the three cases, extended s -, s^\pm - and $p + ip$ -wave pairings are obtained, respectively. Below I discuss in details all three pairing states.

(i) First I consider the case for only intra-valley nesting in the limit of $U \gg V$. Here the results are similar to the single-valley calculations discussed above. Consistently, an extended- s wave symmetry is found for both valleys, where there is a sign reversal between center and corner of the BZ, with a circular nodal line (Fig. 3.4(d)). Inside the circle pairing value is positive and outside it is negative. It is called extended- s , because of the full rotational symmetry of the pairing function over the entire BZ.

(ii) Next I consider the case for only inter-valley nesting alone in the limit of $V \gg U$. A completely different pairing symmetry is obtained. Here I find an *onsite*, s -wave pairing for each valley state, but the sign of the pairing is completely reversed between the two valleys, and hence called s^\pm -pairing state. The result is shown in Fig. 3.4(e). It is evident that the pairing symmetry does not have any k -dependence and arises solely from the onsite pairing of

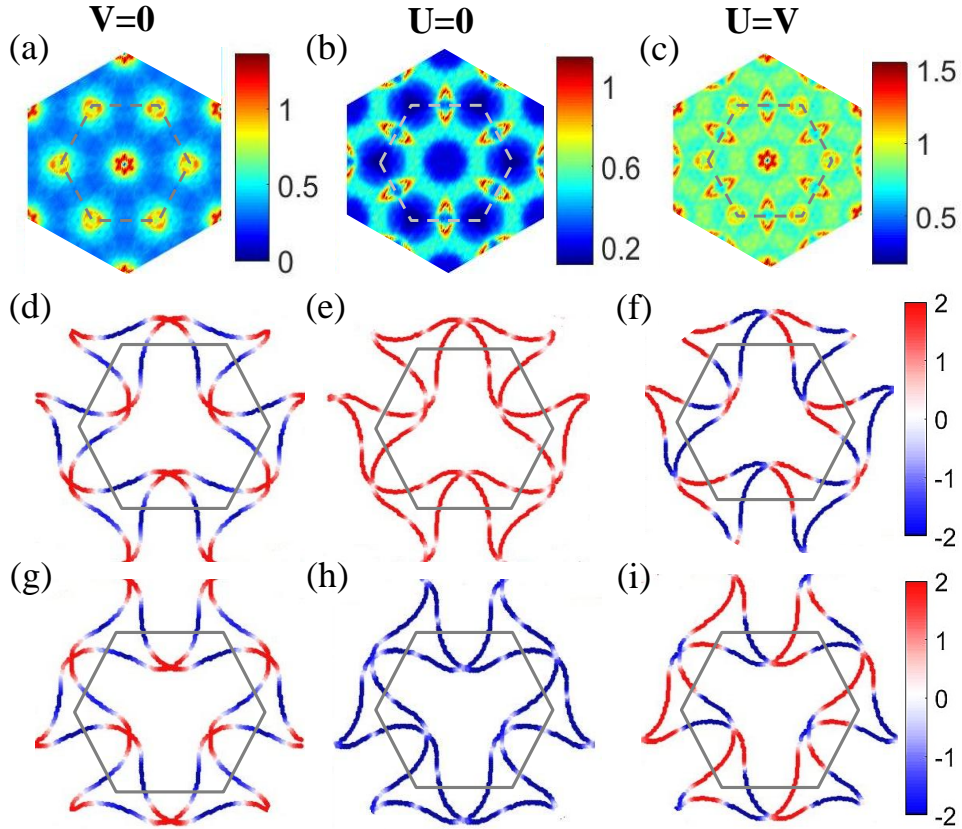


Figure 3.4: (a-c) Spin susceptibility when (a) only intra-valley interaction (U) included with $V = 0$, (b) only inter-valley interaction V is included with $U = 0$, and (c) both intra- and inter-valley interactions are included with $U = V$. (d-i) Computed pairing eigenfunctions for the highest eigenvalue of Eq. 4 in the main text for the corresponding cases in the upper panel. TBG at their VHS dopings are plotted on the FS in a blue (negative) to white (nodes) to red (positive) colormap. We separately plot the two valley result in different rows for easy visualization. (d-f) for one valley and (g-i) for the other valley.

the Wannier orbitals, with different Wannier orbitals on the same site possess opposite phases. This pairing state is quite interesting in that while onsite pairing is often considered in the context of conventional, electron-phonon coupling cases, here one obtains an equivalent condition with an unconventional, electron-electron interaction, mechanism. Note that although the pairing interaction is obtained from the many-body electronic interaction, the strong onsite Coulomb repulsion potential is also present. Therefore, the onsite repulsion overturns the this onsite pairing strength, and such a onsite s^\pm is disfavored.

(iii) Lastly I study the case of having both intra- and inter-valley nestings. The pairing eigenfunction map, plotted in Fig. 3.4(f) shows an approximate $p + ip$ -pairing in a hexagonal

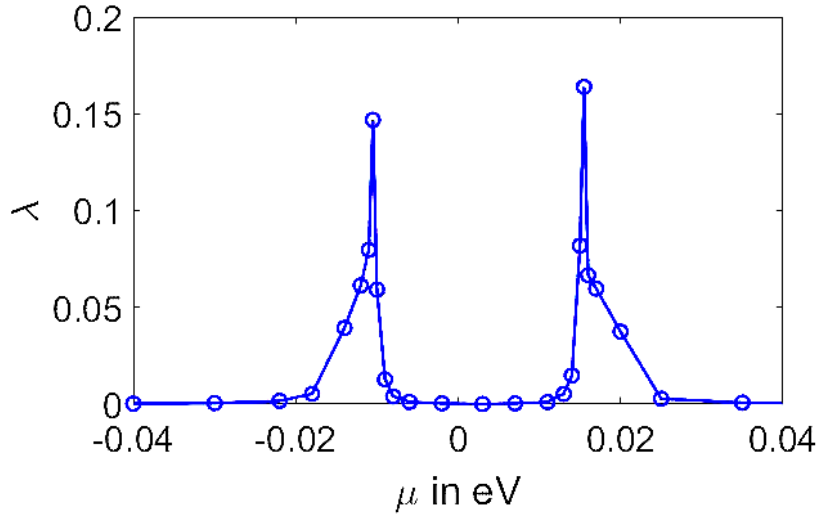


Figure 3.5: Maximum pairing eigenvalue (SC coupling constant) λ as a function of chemical potential shift μ for TBG. Note that the peaks in pairing eigenvalues occur when a flat band passes through the Fermi level.

lattice. The pairing symmetry can be identified by looking at the corresponding nodal lines [see Fig. 3.4(d)] and by performing a reflection operation on any point of the FS. However, unlike previous cases, this symmetry contains higher harmonics of the p -wave symmetries as can be anticipated from complicated colormap of the pairing function on the FS. The pairing eigenvalue of this state is however much lower than the extended- s wave pairing symmetry discussed above.

Doping dependent pairing strength for TBG

Finally, I study the doping dependence of the pairing eigenvalue λ , the SC coupling constant, in TBG, and the result is shown in Fig. 3.5. I find that λ attains maxima at the positions of the maxima of the density of states of the flatbands (roughly at half-fillings in both electron and hole doped sides). The present calculation does not include a correlated Mott gap. Mott gap opposes superconductivity and this will shift the SC maximum away from the half-filling. For future extension of this study, one may pursue to reproduce the experimental phase diagram by including the Mott gap correctly with more sophisticated theory (non perturbative theory like DMFT).

3.7 Discussions and conclusions

All the complex $d + id$, and $p + ip$ pairing symmetries do not possess SC gap nodes on the FS and thus their detection usually requires phase sensitive measurements. The extended s -wave one in TBG possess accidental nodes on both sides of the saddle-point near the VHS doping, and thus the SC gap is very anisotropic. The k -space mapping of the pairing symmetry can be measured via various modern techniques, such as angle-dependent photoemission spectroscopy, scanning tunneling probes via quasiparticle interference (QPI) pattern, field-angle dependence study of thermal conductivity, and so on. The nodal SC quasiparticle also leads to a power-law temperature dependence in many thermodynamical and transport properties which makes it easier to distinguish from conventional pairing. The sign reversal of the pairing symmetry leads to a magnetic spin-resonance at energy $< 2\Delta$ (Δ is SC gap amplitude),[214] magnetic field dependence of QPI peaks,[215] impurity resonance[216] which all can be measured in future experiments for the verification of the underlying pairing symmetry.

In a typical unconventional superconductor, the Wannier states of the Fermi momenta are localized on each lattice site, and hence the correspondence between the reciprocal and direct lattice pairing is trivial. In the Moiré lattice, the location of the Wannier states corresponding to the flat band in TBG depends on energy, twist angle, and inter-layer coupling. In GBN, the Wannier states are localized on a hexagonal lattice. In TBG, they form a triangular lattice for each valley, where the hexagonal symmetry is restored when both valleys are included. Because of these materials specific peculiarities, the pairing symmetry of these materials turn out to be characteristically unique. The present paper spares several open questions for future studies. Superconductivity appears at a considerably low-carrier density ($\sim 10^{12}\text{cm}^{-2}$), which may require adjustments in the theory. The competition between superconductivity and the correlated insulator gap is another interesting theme of research which will be perused in the future.

Chapter 4

Spin topology in twisted bi-layer Moiré pattern

4.1 Introduction

In this chapter, I address the formation of topological spin structure in twisted bilayer hexagonal lattice. Motivated by recent development in 2D magnetic layer systems, I try to incorporate a simple theoretical description for spin-spin interaction in twisted bilayers. And by performing a Monte Carlo simulation I attempt to unravel the nature of the spin structure that emerges at different interaction parameters. Different skyrmion phases as well as some topologically trivial but interesting phases are found in different regions of the phase diagram.

Magnetic order in one and two dimensions has revolutionized the area of 2D spintronics. While Mermin-Wagner theorem prevents a long-range magnetic order in one or two dimensional isotropic systems at non-zero temperature, rare exceptions can happen when introduction of anisotropy gaps out the low energy excitations. Layered Van der Waals (vdW) materials, where the adjacent layers are held together via weak vdW forces, provide an excellent ground to search for such magnetic order in low dimensions. Obtaining skyrmion solutions in low dimensional 2D systems will give new opportunities for science and applications. Recently, long-range magnetic order has been observed in 2D Van der Waals (VdW) chalcogenides, halides, and related materials. Intrinsic antiferromagnetic order is observed in monolayer FePS_3 , [217, 218], and in MPX_3 ($M=\text{Mn,Fe,Co,Ni}$; $X=\text{S,Se}$) [219,

220]. Later on, many VdW materials such as Fe_3GeTe_2 [221, 222], MnX_2 ($X=\text{S,Se}$)[223, 224], VX_2 ($X=\text{S,Se,Te}$)[225, 226, 227] were found to be intrinsic ferromagnet. Another exciting family of 2D vdW magnets is the Cr based materials CrX_3 ($X=\text{I,Br,Cl}$)[228, 229], which are ferromagnets in monolayer, but antiferromagnets in bilayer structure, and the two orderings are externally tunable.[230, 231] Theoretical and experimental efforts to obtain skyrmions in 2D systems are present. Continuum theory of magnetization field in the non-linear sigma model and Landau-Lifshitz-Gilbert model in monolayer and bilayer Moiré systems show the existence of Néel type skyrmions.[90, 91, 232, 233, 234] Recently, a skyrmion phase is observed in 2D Fe_3GeTe_2 on $(\text{Co/Pd})_n$ superlattice[235] and $\text{Fe}_3\text{GeTe}_2/h\text{-BN}$ heterostructure[236] due to their sizable DMI strength.

Skyrmion is a particle dual to a topological configuration of the $O(3)$ fields (read spin) in a 2+1 dimension[237, 71, 238, 239]. Such a spin configuration is an allowed classical solution of the non-linear sigma model. A brief description for different interactions leading to a skyrmion phase was given in chapter 1. Apart from those theoretical understanding, there have been several materials realizations of the skyrmions, mainly in systems with DMI, such as Bloch-type skyrmions in MnSi [240], $\text{Co}_{0.5}\text{Fe}_{0.5}\text{Si}$,[241, 242, 243] Cu_2OSeO_3 ,[244] CoZnMn ,[245] and FeGe [246], and Néel-type skyrmions in ferromagnetic heavy-metals[247], Kagome lattice Fe_3Sn_2 [248], magnetic films,[249], and antiskyrmions in Mn_2RhSn [250, 251]. Experimental abilities to breed,[243, 252] mobilize,[253] rotate[254] skyrmions are also demonstrated recently.[255, 249] Owing to the topological robustness, skyrmions have numerous potential applications in quantum information,[256] racetrack memory [257, 258], which demand enhanced materials flexibilities and tunabilities.

To strategize a new mechanism of the skyrmion, it is worth revisiting it's key ingredients. Firstly, topological skyrmion configurations in 2+1 dimension generally belong to the homotopy group $\pi_2(\mathbb{S}^2) \cong \mathbb{Z}$. The homotopy mapping is exact when both the coordinate space and the target (spin) space are compact \mathbb{S}^2 . **The constraint that all spins \mathbf{S} are aligned at the infinity makes it possible to project the spin space into a Bloch sphere and thus compactifying the spin space.** When a spin configuration has a one-to-one correspondence with the spatial dimensions, this in turn compactifies the position space $\mathbb{R}^2 \rightarrow \mathbb{S}^2$. The resulting one-to-one mapping guarantees the spin configuration to be topological with its skyrmion charge $Q \in \mathbb{Z}$ —

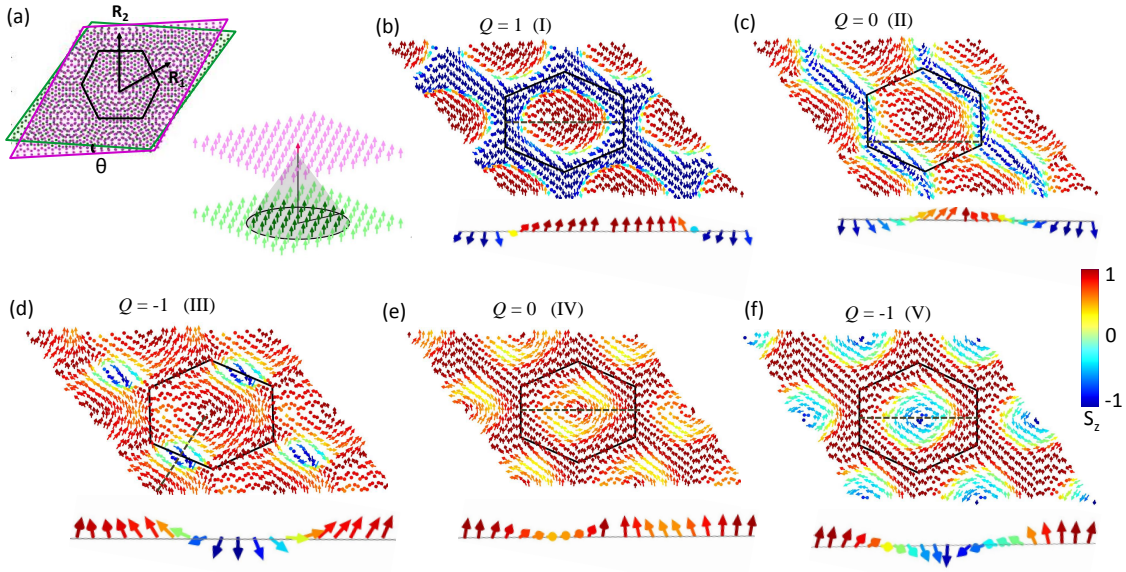


Figure 4.1: Twisted bilayer setup and five distinct topological spin configurations in real space. (a) Schematic diagram of twisted bilayer honeycomb ($\theta =$ twist angle) lattice with a Moiré pattern is shown along with two lattice translation vectors $\mathbf{R}_{1,2}$. A 3D illustration is shown on the lower right corner, in which a single spin of the upper layer (bright magenta color) interacts with bottom-layer spins within a circular region (dark green color) of radius r_{cut} . (b-f) Five distinct spin textures (enumerated by Phase-I to Phase-V) obtained in the $J_{\perp} - J_{\text{D}}$ parameter space (see Fig. 4.3). Arrows denote the spin \mathbf{s} vector, while red to green color-gradient denotes $s_z = 1$ to -1 values. Dashed thin line in each panel indicates the direction along which a 2D spin projection is shown in the corresponding inset. (b),(d),(f) We show three skyrmion structures with distinct charge density (shown in Fig. 4.4) and integer topological charge Q . (c) Phase-II corresponds to a novel higher-order topological phase with streamlines of down spins, and topological dipole moments of antiskyrmions pairs (see Fig. 4.5). (e) This is a trivial topological phase with finite noncollinear ferromagnetic moment.

an integer winding number. The above reasoning can be reversed for a bottom-up approach. If the effective magnetic field $\mathbf{B}(\mathbf{r})$, experienced by a local spin due to the surrounding spins and extrinsic fields, lives on a Bloch sphere \mathbb{S}^2 , then within the minimal Zeeman-like coupling, the field would lay the ground for a topological configuration for the spins. The second essential requirement is that the local field configuration must concomitantly promote a saddle-point energy minimum to stabilize a skyrmion structure.

Guided by these principles, and with the recent discoveries of 2D magnets, I lay a blueprint for novel and multifaceted skyrmions (and antiskyrmions) in twisted magnetic bilayers. I construct a Moiré superlattice of spins formed in twisted bilayer of VdW magnetic layers with ferromagnetic order at the bottom and $O(3)$ spin dynamics on the top layer. The setup is il-

illustrated in Fig. 4.1(a). I include Heisenberg exchange terms J_{\parallel} (for intra-layer) and J_{\perp} (for inter-layer) interactions, and the inter-layer dipole interaction J_D as shown in DFT calculations to be dominant in such setup.[90] Monte Carlo simulation is carried out to determine the microscopic ground state spin configurations at low-temperature, and the entire J_{\perp}/J_{\parallel} and J_D/J_{\parallel} parameter space is swept to create the phase diagram. Three distinct skyrmion phases are identified with topological charges $Q = \pm 1$, whose topological charge distributions reveal a previously unknown hierarchy of point-, rod-, and ring - shape in different topological phases. A novel topological spin configuration is predicted in the vicinity of the $J_{\perp}/J_D \sim -0.4$. I find that near the Moiré lattice sites, a pair of spatially separated and oppositely charged anti-skyrmions is formed and govern a topological (‘electric’) dipole moment. More interestingly, such dipoles are found to align anti-ferroelectrically between the nearest-neighbor sites of the Moiré lattice, and produce a Néel like order for the topological electric dipole moment. These results are explained with a dual electromagnetic theory, demonstrating the ‘electric field’ lines for all topological charge distributions. I also study the ‘x-ray diffraction’ (XRD) pattern of the topological charges (topological charge-charge correlation function) as well as the spin-spin correlation functions to elucidate the crystallization and phase transitions of the topological charge centers and dipoles. These results expand the list of possible skyrmion and magnetic phases (Néel and Bloch phase) obtained in continuum models to a hierarchy of skyrmions and its higher order topological phase.[259, 91]

4.2 Theoretical model for twisted bi-layer spins

I consider a single layer honeycomb magnet (magenta color) placed on a single layer magnetic substrate (green color) of the same lattice structure and lattice constant, as shown in Fig. 4.1(a). The distance between the layers d is taken to be same as the lattice constant of the honeycomb lattice. The spin in the substrate layer is fixed to be a collinear ferromagnetic state. This can be achieved with a strong bulk ferromagnetic material as studied in the literature[233]. I primarily focus on small relative twist angles θ which give the commensurate Moiré superlattices. The twist angle is taken as $\theta = 1.61^\circ$, which gives a hexagonal Moiré lattice with $a = 35.6a_0$, where a_0 is the lattice constant of the single layer system. A critical number of

atoms in a Moiré supercell, determined by the twist angle, is important to stabilize a skyrmion. Above this critical value, the obtained topological phase diagram remains essentially invariant to twist angles and number of atoms, except that the skyrmion radius grows with the Moiré cell dimension. So, there is an upper critical value of the twist angle ($\sim 2^\circ$) above which the Moiré unit cell becomes small enough and the magnetic unit cell is no longer commensurate with the Moiré unit cell.

4.2.1 Hamiltonian formulation

The full Hamiltonian is divided into two parts: $H = H_1 + H_2$, where H_1 and H_2 are the intra-layer, and inter-layer parts. The spin variables for the top and bottom (substrate) layers are labeled by \mathbf{s} , and \mathbf{S} , respectively. The intra-layer Hamiltonian consists of a nearest-neighbor Heisenberg exchange and a spin asymmetry term, for both layers. The inter-layer term consists of many neighbors Heisenberg exchange term and the dipole-dipole interaction term. The bottom layer's spins are then integrated out to obtain an effective Hamiltonian for the top layer as $H_{\text{top}} \sim H_1 + \mathbf{B} \cdot \mathbf{s}$, where \mathbf{B} is the effective magnetic field exerted from the bottom layer on the top layers spin \mathbf{s} . The Moiré periodicity is imposed by expanding these terms in the plane wave basis of the Moiré supercell. Hamiltonian for top layer H_{top} is solved within the Monte Carlo simulation.

I now give the details of the model. The 2D VdW systems in single and bilayer setups are observed to show an in-plane ferromagnetic (and out-of-plane ferro- or anti-ferromagnetic) order with the spin quantization axis to be out-of-plane (z -direction).[87, 260] Such a magnetic ground state is reproduced by the model:

$$H_1(\mathbf{s}) = -J_{\parallel} \sum_{\langle ij \rangle} \mathbf{s}_i \cdot \mathbf{s}_j - K \sum_i (s_{iz})^2, \quad (4.2.1)$$

where i, j are lattice sites within a Moiré supercell. The first term is the nearest neighbor Heisenberg interaction with coupling constant $J_{\parallel} > 0$ for a ferromagnetic phase, and K gives the z -axis asymmetry, breaking the $O(3)$ spin degeneracy. $H_1(\mathbf{S})$ term gives the corresponding Hamiltonian for the bottom layer, with J_{\parallel} and K kept fixed.

The inter-layer interaction H_2 is the crucial part. Depending on the twist angle, espe-

cially at small twist angles, a spin at the top layer interacts with several neighboring bottom layer spins, and hence the inter-layer interaction involves terms beyond the nearest-neighbor exchange interaction. The inter-layer interaction is mainly dominated by several nearest-neighbor exchange interaction H_{ex} and dipole-dipole interaction (H_{D}) as $H_2(\mathbf{S}, \mathbf{s}) = H_{\text{ex}} + H_{\text{D}}$ where

$$H_{\text{ex}} = - \sum_{ij} J_{\perp}(\mathbf{r}_{ij}) \mathbf{S}_i \cdot \mathbf{s}_j, \quad (4.2.2)$$

$$H_{\text{D}} = J_{\text{D}} \sum_{ij} \frac{1}{r_{ij}^3} [\mathbf{S}_i \cdot \mathbf{s}_j - 3(\mathbf{S}_i \cdot \hat{\mathbf{r}}_{ij}) \cdot (\mathbf{s}_j \cdot \hat{\mathbf{r}}_{ij})]. \quad (4.2.3)$$

i, j are the site indices in the bottom and top layer, respectively. $\mathbf{r}_{ij} = \mathbf{r}_i - \mathbf{r}_j$ with $\hat{\mathbf{r}}_{ij}$ being the corresponding unit vector. Since both interactions are long-ranged, we need to set a cutoff radius r_{cut} , see Fig. 4.1(a) (inset). Due to higher power of r_{ij} in the denominator, the result converges quickly by $r_{\text{cut}} < 20a_0$ which is much smaller than the Moiré lattice size $\sim 35a_0$. For realistic VdW materials, the dipole coupling strength is small ($J_{\text{D}} \sim 0.1J_{\perp}$) and the interlayer exchange is also small compared to intralayer exchange ($J_{\perp} \sim 0.3J_{\parallel}$). So intralayer dipole would be 100 orders of magnitude smaller than J_{\parallel} . This small magnitude will not change the spin orientation coming from the strong intralayer ferromagnetic alignment considered here. But, if intralayer dipole is large enough, the effect can be non-trivial and the spins would tend to align themselves more in the planner direction. Inclusion of intralayer dipole interaction on the top layer makes the problem harder since the spins on the top layer changes at each Monte Carlo step. New technique needs to be implemented to find the exact spin configuration for larger intralayer dipole-dipole interaction.

Next, the bottom layer's spins are integrated out \mathbf{S} , and an effective magnetic field is defined at the top layer at \mathbf{r}_i as $\mathbf{B}(\mathbf{r}_i) = \mathbf{B}_{\text{ex}}(\mathbf{r}_i) + \mathbf{B}_{\text{D}}(\mathbf{r}_i)$, where \mathbf{B}_{ex} , and \mathbf{B}_{D} distinguish the contributions from the exchange and dipole-dipole interaction terms as $\mathbf{B}_{\text{ex}}(\mathbf{r}_i) = -\frac{\partial H_{\text{ex}}}{\partial \mathbf{s}_i} = \frac{J_{\perp}}{2} \sum_a e^{i\mathbf{G}_a \cdot \mathbf{r}_i}$, and $\mathbf{B}_{\text{D}}(\mathbf{r}_i) = -\frac{\partial H_{\text{D}}}{\partial \mathbf{s}_i}$. We set $\mathbf{S}_j = \hat{z}$ for all unit spins at the bottom layer. This may be achieved by considering the Moiré bilayer at the interface of two bulk materials, where the lower layer comes from a material which has very high ferromagnetic exchange. This can force spins of one layer to align in z direction. $\mathbf{G}_a (a = 1 - 6)$ are the six minimal reciprocal lattice vectors of the Moiré superlattice. The six possible smallest reciprocal lattice vectors

are included in the Moiré lattice and the results do not change with the inclusion of negligibly small contribution of higher reciprocal lattice vectors. Dipole interaction is known to be an useful ingredient for (generally bubble-type) skyrmions and antiskyrmions,[70, 238, 251] but are significantly weaker in strength in real materials. In twisted bilayer system, however, the intra-layer dipole interaction is considerably enhanced, and is found here to be detrimental to the bubble or Bloch skyrmion phases (see below), while promoting novel and distinct skyrmion phases.

In this manner, the bottom layer's effects can be cast into a Zeeman-like term at the top layer. The full Hamiltonian hence takes the form

$$H = H_1 - \sum_i \mathbf{B}(\mathbf{r}_i) \cdot \mathbf{s}_i. \quad (4.2.4)$$

In this way, the total Hamiltonian simplifies to the form used in the introduction for discussing how the in-plane spin is enforced to lie on a topological compact space \mathbb{S}^2 by tailoring the 'long-range' Zeeman coupling.

4.2.2 Effective inter-layer magnetic field

The effect of H_{ex} and H_D can be described by effective magnetic field $\mathbf{B}(\mathbf{r}_i)$ coming from exchange ($\mathbf{B}_{ex}(\mathbf{r}_i)$) and dipole ($\mathbf{B}_D(\mathbf{r}_i)$). Taking all the bottom layer's spin \mathbf{S} to be along the $+z$ -direction, The field components can be written explicitly as

$$\mathbf{B}_{ex}(\mathbf{r}_i) = J_{\perp} \sum_{a=1,2,3} \cos(\mathbf{G}_a \cdot \mathbf{r}_i) \hat{\mathbf{z}}, \quad (4.2.5)$$

$$\mathbf{B}_D(\mathbf{r}_i) = \sum_j \frac{J_D}{r_{ij}^3} \left[1 - \frac{3d^2}{r_{ij}^2} \right] \hat{\mathbf{z}} - \frac{3J_D d}{r_{ij}^5} [(x_i - x_j) \hat{\mathbf{x}} + (y_i - y_j) \hat{\mathbf{y}}]. \quad (4.2.6)$$

The index i denotes a top layer spin. The sum over j denotes a sum over bottom layer spins and is restricted up to $r_{cut} = N_{cut} a_0$. Due to the higher power of r_{ij} in the denominator, it is easy to check that the summation converges very rapidly ($\sim N_{cut} < 20$), much before the Moire supercell lattice vector $R_{1,2} \sim 35a_0$. \mathbf{G}_a denotes three lowest Moiré reciprocal lattice vectors, d is the inter-layer distance, and x_i, y_i are x and y coordinates of i^{th} spin. \mathbf{B}_{ex} is plotted in fig. 4.2(a) and (c) for $J_{\perp} < 0$ (ferromagnetic) and $J_{\perp} > 0$ (antiferromagnetic)

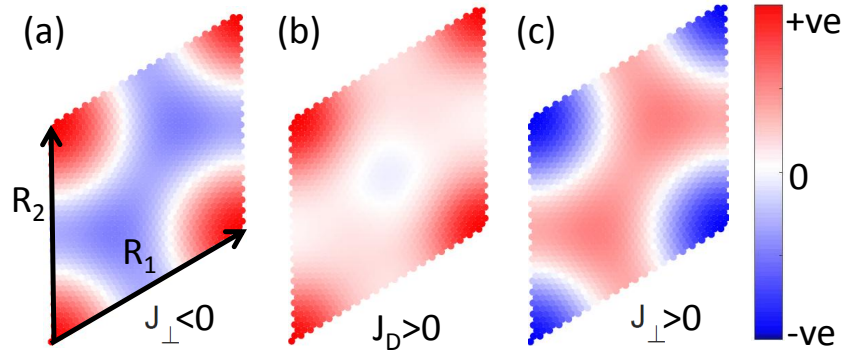


Figure 4.2: Effective magnetic fields along the z -direction in the Moiré unit cell. (a) Field due to the inter-layer exchange interaction (B_{ex}) for $J_{\perp} < 0$ and (c) for $J_{\perp} > 0$. (b) Field due to the inter-layer dipole interaction (B_D) for $J_D > 0$. \mathbf{R}_1 and \mathbf{R}_2 denote the two translation lattice vectors.

respectively. Please note that \mathbf{B}_{ex} changes sign in the Moiré unit cell creating a local effective field landscape when combined with \mathbf{B}_D (shown in fig. 4.2(b)). This is responsible for various spin pattern seen in different phases. Also note that for $J_{\perp} < 0$ and $J_D > 0$, \mathbf{B}_{ex} and \mathbf{B}_D have the same sign at the corners, and create a narrow domain wall in Phase I. But for both $J_{\perp} > 0$ and $J_D > 0$, \mathbf{B}_{ex} and \mathbf{B}_D compete at the corner, and thereby create a wide domain wall, and consequently produce a stable skyrmion in Phase V.

Here, I should distinguish the effects of the dipole-dipole interaction H_D of the present study versus the previous ones. In earlier studies,[70] such an interaction is involved for the same intra-layer spin (between s and s variables) which tend to give magnetic bubble phases.[238] On the other hand, here the dipole interaction is between inter-layer (s and S), and is detrimental to the bubble or Bloch skyrmion phases, while promote the streamline flow of the polarity density.

4.3 Monte Carlo method

In the Monte Carlo simulation, the local Hamiltonian is minimized for a single spin with temperature annealing as well as parameter annealing, the total energy of the system is also converged in each case. In all the calculations performed here, the minimization of the local Hamiltonian corresponds to minimization of the total energy. Next I discuss the details of the Monte Carlo simulation.

As mentioned in the previous section, the Hamiltonian for the top layer can be written as

$$H = H_1 + \sum_i \mathbf{B}(\mathbf{r}_i) \cdot \mathbf{s}_i. \quad (4.3.1)$$

Here H_1 is the intra-layer Hamiltonian and $\mathbf{B}(\mathbf{r}_i)$ is the effective magnetic field due to inter-layer interaction. The lattice site \mathbf{r}_i spans the Moiré unit cell. In this calculation at the commensurate angle 1.61° there are 2522 basis site per unit cell. All the classical spins are set to have unit length ($S_i = 1$) so that all the spins can be specified with two parameters S_z and ϕ where ϕ is the angle that the component of spin on the xy -plane (s^{xy}) makes with the x axis. From these two parameters, all the three components of the spins can be extracted as

$$\begin{aligned} s_i^{xy} &= \sqrt{1 - (s_i^z)^2}, \\ s^x &= s^{xy} \cos(\phi), \\ s^y &= s^{xy} \sin(\phi). \end{aligned} \quad (4.3.2)$$

The simulation is initialized with all spins pointing upward i.e., $S_i^z = 1$, and then the next spin is chosen randomly from all the lattice points. The update algorithm for that spin is given by

$$\begin{aligned} s_i^z &= s_i^z + \gamma ds^z, \\ \phi_i &= \phi_i + \gamma d\phi. \end{aligned} \quad (4.3.3)$$

And if $|s_i^z| > 1$ then

$$\begin{aligned} s_i^z &= 2 \mp (s_i^z + \gamma ds^z), \\ \phi_i &= \phi_i + \gamma d\phi + \pi. \end{aligned} \quad (4.3.4)$$

Here the \pm signs are for $s_i^z > 1$ and $s_i^z < -1$, respectively. γ is a random number between 1 and -1, and ds^z and $d\phi$ are ranges of s^z and ϕ .

At each Monte Carlo step the local Hamiltonian is calculated as

$$H(\mathbf{r}_i)_{loc} = H_1(\mathbf{r}_i) - \sum_i \mathbf{B}(\mathbf{r}_i) \cdot \mathbf{s}_i, \quad (4.3.5)$$

$$H_1(\mathbf{r}_i) = \sum_{\langle i,j \rangle} J_{||} \mathbf{s}_i \cdot \mathbf{s}_j. \quad (4.3.6)$$

and each configuration is accepted with a Boltzmann probability $e^{[H(\mathbf{r}_i)_{loc}^{new} - H(\mathbf{r}_i)_{loc}^{old}]/k_B T}$ at temperature T . To find the low temperature Monte Carlo ground state temperature annealing as well as parameter annealing were performed, and convergence of the total ground state energy was verified. At low temperature the value of $ds^z (= 0.1)$ and $d\phi (= 0.1\pi)$ was decreased (from $ds^z = 0.4$ and $d\phi = 0.4\pi$) to increase the acceptance ratio in Monte Carlo steps. The system is equilibrated with 10^8 steps and low energy configuration is taken after another 10^8 steps.

4.4 Results

4.4.1 Phase diagram

The Monte Carlo simulation yields a plethora of quantum and topological phases; five such distinct configurations are identified in Figs. 4.1(b)-(f). The corresponding phase diagram is presented in Fig. 4.3 for $J_{\perp}/J_{||}$ and $J_D/J_{||}$ with $J_{||} > 0$. In the phase diagram, the red and blue shaded areas denote distinct skyrmion phases with topological invariant $Q = \pm 1$, respectively. The white regions represent a higher-order dipolar antiskyrmion phase (Phase-II), and a trivial phase (Phase-IV). From Figs. 4.1(b),(d), and (f), it is evident that the three skyrmion phases, denoted by Phase-I, III, and V, are characteristically exclusive, which will be distinguished below in multiple ways. Phase-II has zero net topological charge, but possess higher-order topological dipole moment and its antiferroelectric ordering. The Phase-IV bears no topological or exotic quantum order (except finite magnetization due to a collinear spin ordering).

The particle dual of the skyrmion is a topological charge denoted by $Q = \int d^2\mathbf{r} \rho(\mathbf{r})$, where $\rho(\mathbf{r})$ is the topological charge density. With its corresponding current density $\mathcal{J}_{x,y}$, the three-

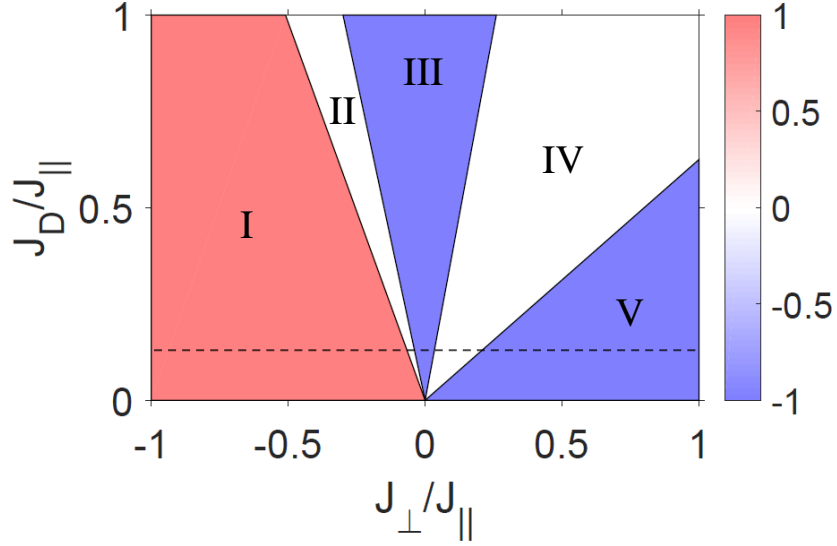


Figure 4.3: Phase diagram of five distinct topological phases. The inter-layer exchange coupling J_{\perp} and dipole interaction J_D are varied with respect to the in-plane exchange coupling J_{\parallel} . $J_D < 0$ is an unphysical value, however, mathematically it leaves the phase diagram symmetric when the sign of J_{\perp} is also reversed. Red and blue color distinguishes skyrmion charges of $Q = \pm 1$. Phase-II, although features a net $Q = 0$, exhibits a novel topological dipole moment of antiskyrmions which produces an antiferroelectric order state. The horizontal dashed line indicates the realistic parameter range as deduced in a DFT calculation.[90]

component density operators $\mathcal{J}_{\mu} = (\rho, \mathcal{J}_x, \mathcal{J}_y)$ can concisely be defined as

$$\mathcal{J}_{\mu}(\mathbf{r}) = \frac{\epsilon_{\mu\nu\tau}}{8\pi} \mathbf{n} \cdot \partial_{\nu} \mathbf{n} \times \partial_{\tau} \mathbf{n}, \quad (4.4.1)$$

where $\mu, \nu, \tau = 0, x, y$ are time-space indices, and the \mathbf{r} dependence on the unit vector field $\mathbf{n} = \mathbf{s}/|\mathbf{s}|$ is implied. The vortex density is defined as $\mathbf{v}(\mathbf{r}) = \epsilon_{\nu\tau} \partial_{\nu} \mathbf{n} \times \partial_{\tau} \mathbf{n}$. In this layered geometry and with the z -axis asymmetry, it is natural to expect that the vorticity of the spin-texture commences in the xy -plane, i.e. v_z dominates. Then the corresponding polarity density is simply governed by $n_z(\mathbf{r})$. The z -components of the polarity density $n_z(\mathbf{r})$, the vortex density $v_z(\mathbf{r})$ and the charge density $\rho(\mathbf{r})$ are investigated in Fig. 4.4 in three different rows for the five distinct phases (different columns).

The mechanism of skyrmions and antiskyrmions is retrieved as follows. It is known from the topological band theory[261] that the polarity field (equivalent to the Dirac mass for fermion fields) forms a nodal (closed) contour, across which $n_z(\mathbf{r})$ changes sign – this is

called the domain wall (see top row in Fig. 4.4). The vorticity field $v_z(\mathbf{r})$ inside the domain wall acquires singularity – either point- or rod-, or ring- shaped singularity – and cannot be removed with a trivial gauge transformation (see middle row in Fig. 4.4). Hence the topological charge density $\rho(\mathbf{r})$ becomes confined within the domain wall (see bottom row in Fig. 4.4). The homotopy mapping of the $\mathbf{n}(\mathbf{r})$ field on \mathbb{S}^2 in the \mathbf{r} -space quantizes the topological charge $Q \in \mathbb{Z}$, where the integration of \mathbf{r} is performed within a single domain wall of the polarity density [see black solid lines in Fig. 4.4(f-o)].

4.4.2 Skyrmion Hierarchy

Phase-I is a topological phase with $Q = -1$, and is present in most of the $J_\perp/J_\parallel < 0$ region. It is destabilized at smaller values of J_\perp by stronger dipole interaction J_D . The distributions of n_z , v_z , and ρ for Phase-I are shown in the left-most column in Fig. 4.4. The polarity density map $n_z(\mathbf{r})$ demarcates a sharp and circular domain wall boundary, which reminds of a magnetic bubble observed in astronomical space, as well in magnetic systems.[262] The vorticity and charge densities of this phase, however, reveal much richer structures unknown before. Fig. 4.4(f) shows that the nodal ring of the polarity density (black line) encloses a circular vortex density $v_z(\mathbf{r})$ structure. In fact, $v_z(\mathbf{r})$ is positive (negative) outside (inside) the domain wall, and share the same nodal ring as that of $n_z(\mathbf{r})$. In what follows, the charge density $\rho(\mathbf{r})$ also acquires a singular ring geometry, confined by the domain wall boundary, see Fig. 4.4(k). This phase is also topologically equivalent to the Dirac nodal ring state[263] in the electronic structure in which the topology is defined via Berry gauge connection.

As $J_\perp \rightarrow -J_\perp$, keeping all other interactions fixed, a characteristically distinct skyrmion texture (denoted by Phase-V) is obtained with opposite charges $Q = \pm 1$. Unlike the sharp domain wall in Phase-I, n_z varies smoothly with r , and forms a (nearly) elliptical domain wall in Phase-V. Moreover, the Phase-V has a point-like topological charge center sitting at the Moiré supercell center. Hence as opposed to ring-singularity in Phase-I, Phase-V acquires point (pole) singularity. The asymmetry between the Phase-I and Phase-V at $\pm J_\perp$ for fixed J_D , results from the competition between J_\perp and J_D . The phase diagram is reversal between $\pm J_\perp$ for $J_D \rightarrow -J_D$.

The skyrmion Phase-III occurs in the vicinity of $J_\perp \sim 0$, and is mainly stabilized by the

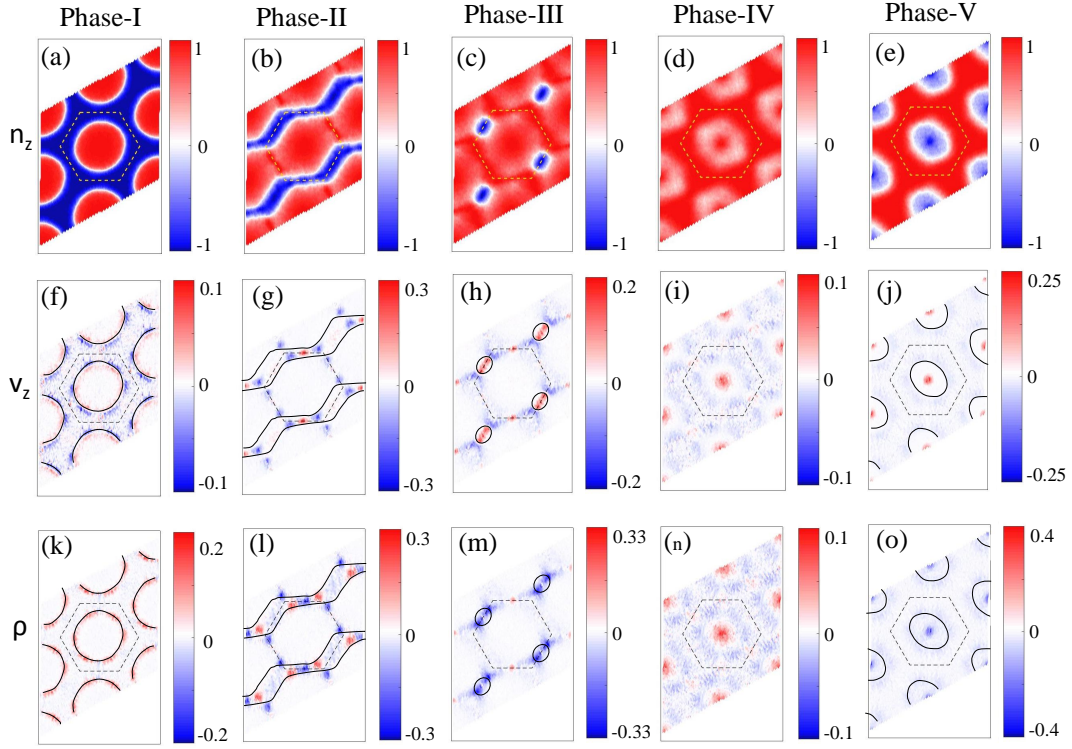


Figure 4.4: Local variation of polarity, vorticity, and topological charge densities in the five different topological phases. (a-e) The z -component of the polarity density $n_z(\mathbf{r})$ (see main text) is plotted in blue to red colormap, denoting down to up spin components of s_z . (f-j) We plot the vorticity density $v_z(\mathbf{r})$ with blue to red colormap. The black solid line marks the $n_z = 0$ domain wall boundary. (k-o) Corresponding topological charge density $\rho(\mathbf{r})$ is plotted here. In Phase-II, IV, although charge centers are formed but the net charge $Q = 0$. In Phase-II, fractional charge centers are confined by streamline domain wall, giving a novel topological dipole moment. There is no domain wall of n_z in Phase-IV and hence its a trivial phase. (Different color scales are for the five phases in the middle and bottom panels.)

long-range (out-of-plane) dipole-dipole interaction J_D . The magnetic domains are elliptical in shape, and concentrated at two sides of the Moiré supercell. As seen in Fig. 4.4(h) and (m), the n_z nodal contour confines a fixed-sign vorticity field (positive), and hence the topological charge distribution (negative since $n_z < 0$) becomes quantized. The topological charge density is distributed inside the elliptical domain wall and gives a rod-like singularity. Such a rod-like topological charge distribution repeats periodically [see Fig. 4.4(m)] and give a nematic or smectic crystal.

In all three skyrmion phases, each Moiré supercell contains a single skyrmion configuration. Therefore, a suitable characteristic length scale associated with different skyrmions can

be defined by the domain wall contour \mathbf{r}_d where $n_z(\mathbf{r}_d) = 0$. This condition is very much satisfied where the effective magnetic field due to the bottom layer along the z -direction vanishes, i.e., $B_{ex}^z(\mathbf{r}_d) + B_D^z(\mathbf{r}_d) = 0$. From the expression for B_{ex} , and B_D given in the Sec. 4.2.2, it can be seen that \mathbf{r}_d depends on the ratio J_\perp/J_D , and the inter-layer distance d for a given Moiré lattice. Depending on the ratio J_\perp/J_D , the condition can turn into an equation of a circle or an ellipse, as also seen from numerical calculations. In Phase-III, the domain wall takes an elliptic shape in Fig. 4.4(h) and the two topological charge centers found here in Fig. 4.4(m) sits at the two focal points.

It is then easy to grasp that a skyrmion phase transition occurs when domain wall radius r_d either shrinks to zero or expands to the Moiré cell boundary $\mathbf{R}_{1,2}$. The phase transition between Phase-I to Phase-II occurs when $r_d = \mathbf{R}_1$ or \mathbf{R}_2 . The rotational symmetry breaking renders a small domain wall to form in Phase-III with opposite polarity at one of the Moiré supercell's site for small values of J_\perp , as seen in Fig. 4.4(c). This small domain wall then shrinks to zero with the sign reversal of J_\perp which disfavors the domain wall of negative polarity. Curiously, there still exists a finite vortex structure and a finite charge density in the trivial Phase-IV. But owing to the absence of a compact domain wall of the polarity density, the net topological winding number vanishes. Hence, the Phase-IV corresponds to a quasi-uniform ferromagnetic phase (or antiferromagnetic phase if $J_\parallel < 0$) as seen in the untwisted CrI_3 bilayer samples.[90] Finally, large J_\perp creates another compact domain wall at the center of the Moiré supercell in which the topological charge is $Q = -1$.

4.4.3 Topological antiferroelectric phase

Phase-II is very intriguing and novel, and requires separate discussions. The naive spin-texture of this phase (Fig. 4.1(c)) is reminiscent of a spin spiral phase. However, unlike in the other trivial spiral phases, here several new type of topological charge centers are formed as shown in Fig. 4.4(l) and 4.5(a). Firstly, the polarity density has a streamline flow diagram with 1D domain wall, see Fig. 4.4(b). But it fails to commence a compact geometry to produce full skyrmion charge centers. However, there exists five sharp charge centers (three inside the $n_z = -1$ (blue) region and two outside). This structure periodically repeats in a smectic pattern. These charge centers have different origin from the previous three skyrmion phases

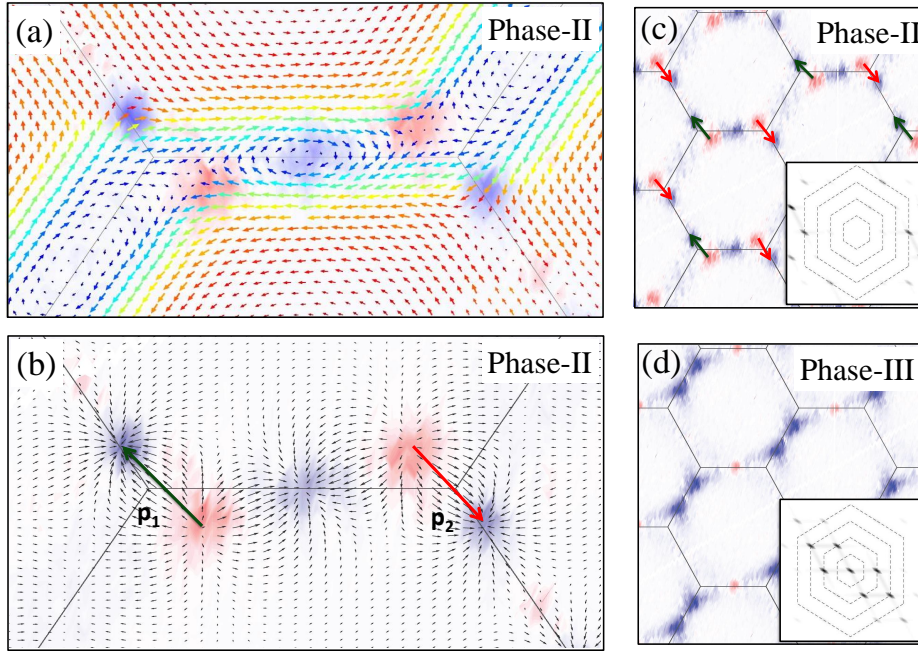


Figure 4.5: Antiferroelectric Phase-II. (a-b) Zoomed-in view of the topological charge density in blue to red color map is plotted in the background, with arrows denoting spins s in (a), and emergent electric field \mathbf{E} vector in (b). The spin texture clarifies the formation of topological charge at the Moiré lattice side, and a pair of antiskyrmions with opposite charge centers near the Moiré lattice corners. The electric field lines in (b) confirm the formation of topological dipole moment (long arrows) between the antiskyrmion pairs. (c-d) Real space view of the topological charges in many Moiré unit cells for Phase-II and Phase-III, respectively. (c) We clearly observe the Néel analog of the ordering of the topological dipole moments, giving an antiferroelectric phase. (d) As we move from Phase-II to Phase-III, the antiskyrmion pairs are annihilated and integer topological charges become confined by a compact domain wall on different lattice sides. *Inset*: The structure factor of the corresponding topological charge density, showing no charge ordering in Phase-II, as opposed to Bragg peaks in Phase-III.

with compact polarity density, and result from splitting of the vorticity by streamline flow of polarity density.

A zoomed-in view of the spin texture on top of the topological charge density, as shown in Fig. 4.5(a), unravels the mechanism of these charge centers. The charge center at the middle (blue-colored charge density) is a ‘meron’-like structure, but with a fractional charge of $Q \sim 2/9 \pm 0.025$. The other four charge centers form in pairs with opposite sign of charges at the Moiré zone corners. The corresponding spin textures reveal that they are *antiskyrmions*, [251, 250] with fractional charges $Q \sim \pm 2/9 \pm 0.025$. We note that although there are five distinct meron like charge centers with $\pm 2/9$, they are shared between neighboring Moiré supercells.

Apart from these concentrated point charges, another $+2/9$ (red) is spread over the Moiré cell which is not clearly visible in the colormap of Fig. 4.5(a),(b). Hence, the total charge (point-charge and background-charge) within a given Moire supercell vanishes.

Each pair of oppositely charged antiskyrmions acts as a topological electric dipole, sitting at each lattice site of the Moiré lattice. The dipole moment is estimated to be $(0.05 \pm 0.005)a$, where a is the Moiré lattice constant. More interestingly, the dipoles are aligned *anti-ferroelectrically* between the nearest neighbors. This gives a Néel-like ordering of the topological dipole moments, in close analogy to the Néel order of magnetic moments in a honeycomb lattice.

Comparisons of the spin-textures between Phase-II (anti-ferroelectric) and Phase-III (skyrmions) throw light on the phase transition between them. The phase transition occurs when the anti-skyrmion pairs coalesce. This also results in the closing of the streamline flow of the polarity density to form a compact domain wall (see Fig. 4.4(c)). Hence a topological winding number description becomes appropriate in Phase-III.

4.4.4 Conditions for phase transition

Clearly, a compact domain wall forms at the nodal contour of $s_z(\mathbf{r})$ where the total magnetic field roughly vanishes, i.e., $B_z(\mathbf{r}_d) = 0$. (This approximation works better where the in-plane spin exchange $J_{||} \ll |B|$, so that the second term in Eq. (4.2.4) dominates). Then the condition simplifies to

$$\frac{J_{\perp}}{J_D} \beta_{ex}(\mathbf{r}_d) + \beta_D(\mathbf{r}_d) = 0. \quad (4.4.2)$$

where \mathbf{r}_d is the locii of the domain wall boundary and β_{ex} and β_D are given by

$$\beta_{ex}(\mathbf{r}_d) = \sum_a \cos(\mathbf{G}_a \cdot \mathbf{r}_d) \quad (4.4.3)$$

$$\beta_D(\mathbf{r}_d) = \sum_j \frac{1}{|\mathbf{r}_d - \mathbf{r}_j|^3} \left[1 - \frac{3d^2}{|\mathbf{r}_d - \mathbf{r}_j|^2} \right]. \quad (4.4.4)$$

It is not easy to find an analytical expression for this nodal contour from Eqs. (4.2.5), and (4.2.6). But it's clear that the value of \mathbf{r}_d depends on the J_{\perp}/J_D ratio and the bilayer thickness d for a given Moiré lattice denoted by \mathbf{G} . The equation of the nodal line can be a circle or

an ellipse depending on these parameters. As seen from the numerical simulation, the domain wall is circular for large values of J_{\perp} , while it takes an elliptical form in Phase-III for small values of J_{\perp} .

Again in the limit of $J_{\parallel} \ll |B|$, a phase transition is defined at $J_{\perp}/J_D = -\beta_D(\mathbf{r}_d)/\beta_{ex}(\mathbf{r}_d)$ (from Eq. (4.4.2)) for different values of \mathbf{r}_d . In phase I, the radius of circular patch increases as $J_{\perp} \rightarrow 0$, and at the transition point to phase II two circular regions merge together at $\mathbf{r}_d = \mathbf{R}_1/2$. On the other hand, \mathbf{r}_d decreases in phase V as $J_{\perp} \rightarrow 0$, which implies $\mathbf{r}_d = 0$ at the transition from the phase V to phase IV. Similarly transitions from phase II to III and III to IV are given by $\mathbf{r}_d = \mathbf{R}_2/2$ and $\mathbf{r}_d = (\mathbf{R}_1 + \mathbf{R}_2)/2$ respectively. By numerically evaluating β_{ex} and β_D at various \mathbf{r}_d , the approximate critical values of the ratio J_{\perp}/J_D for different transitions are extracted which are listed in the table 4.1 A direct comparison of transition from

Table 4.1: Critical values of \mathbf{r}_d and J_{\perp}/J_D at different phase transition points.

Transitions	\mathbf{r}_d	J_{\perp}/J_D
Phase I to phase II	$\mathbf{R}_1/2$	-0.57
Phase II to phase III	$\mathbf{R}_2/2$	-0.4
Phase III to phase IV	$(\mathbf{R}_1 + \mathbf{R}_2)/2$	0.3
Phase IV to phase V	$\mathbf{0}$	1.6

phase ‘I to II’ and phase ‘IV to V’ reveals that $|J_{\perp}/J_D|$ is larger on the positive side (1.6 on positive side and -0.57 on negative side). This can be understood from Fig. 4.2. At the corner of the Moiré supercell B_{ex} and B_D have the same sign in the $J_{\perp} < 0$ region. So their effects add up. This is also responsible for a thin domain wall of magnetic bubbles in phase I. In the positive J_{\perp} region, however, B_{ex} and B_D have opposite sign. So a larger value of J_{\perp} is needed to overcome the effect J_D in positive side. This leads to a wider domain wall in phase V.

4.4.5 Electromagnetic duality

To visualize the formation of the dipole moment in Phase-II, I write down a gauge-dual theory, and calculate the topological electric field lines. In an electronic quantum Hall analog, a physical charge is attached to a magnetic flux via the Chern-Simons coupling – also known as the Stréda formula.[264] Using this analogy, I affix an emergent gauge field $a_{\mu} = (\phi, \mathbf{a})$

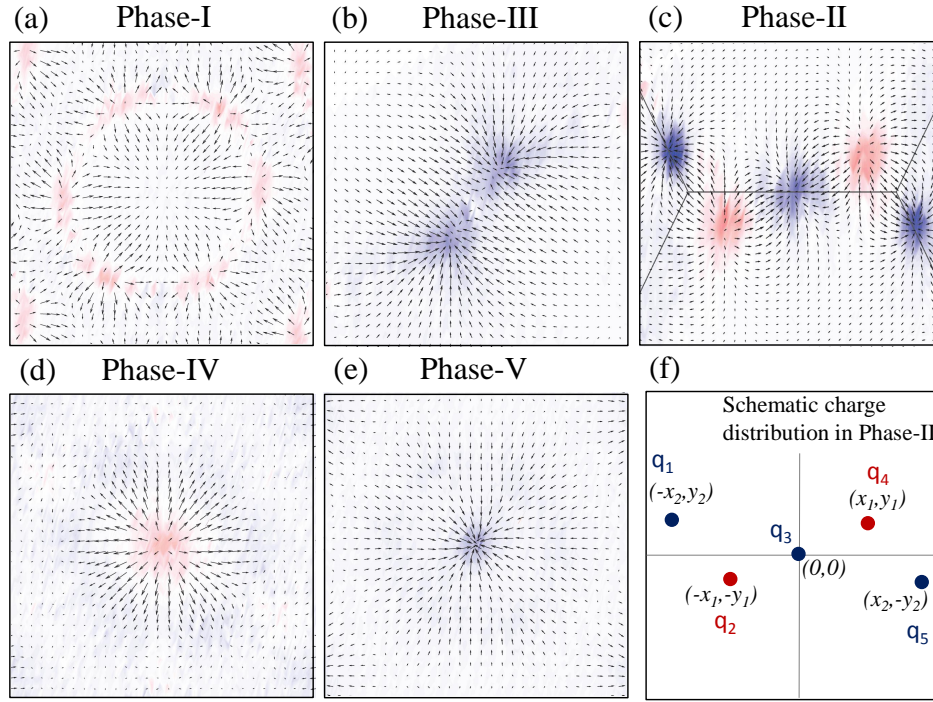


Figure 4.6: (a-e) The emergent topological electric field lines on top of the topological charge density in the vicinity of the charge centers (see Fig. B.2 for larger view) in all five phases. In (f) the schematic distribution of point charges for Phase II is shown with origin of the coordinates at the charge q_3 .

with the topological charge density ρ as $\mathcal{J}_\mu = \epsilon_{\mu\nu\tau} \mathcal{F}_{\nu\tau}$. Here $\mathcal{F}_{\nu\tau} = \partial_\nu a_\tau - \partial_\tau a_\nu$ is the corresponding curvature field tensor (an emergent electro-magnetic field, but not the same \mathbf{B} field seen by local spins). The emergent ‘electric field’ is read as $\mathbf{E} = -\nabla\phi - \partial_t \mathbf{a}$. This ‘electric field’ follows the Gauss’ law, and acquires distinct spatial dependence according to the topological charge distributions. Using the Gauss law, the electric field lines can be found numerically from $\int \mathbf{E} \cdot d\mathbf{S} = \rho$. The electric field lines shown by black arrows in Fig. 4.5(b) confirm the existence of the dipole moment and their antiferroelectric ordering. The calculations of electric field lines are extended to all the other phases, and it is found that the field line configurations are consistent with the ring-, rod-, and point-like charge centers as obtained in Phase-I, Phase-II, and Phase-V, respectively (see Fig. 4.6).

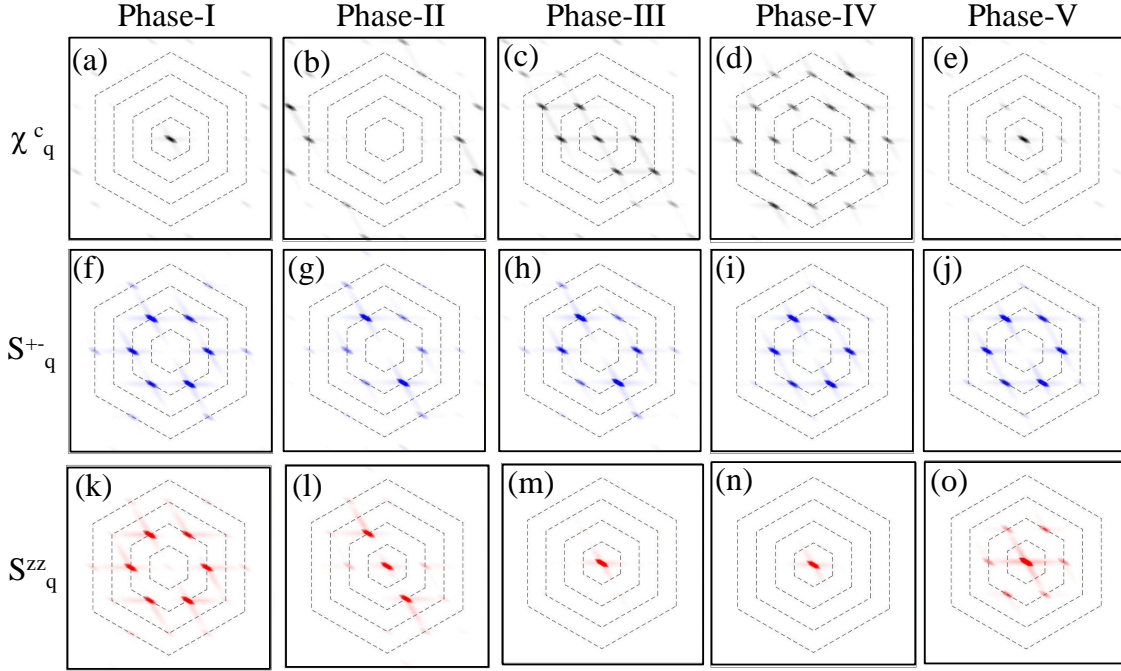


Figure 4.7: Structure factors. (Left) Left row gives the structure factor of the topological charge density (Fourier transformation of the charge-charge correlation function). (Middle) Transverse spin-spin correlation functions. (Right) Longitudinal correlation function in the momentum space. In all three cases, we give various quadrants of the Brillouin zone with dashed lines.

4.4.6 Topological correlation functions and structure factors

From Fig. 4.4, it is evident that there are finite topological charge distributions even in the trivial topological phases where the polarity density n_z fails to create domain walls. **Therefore, to obtain a microscopic nature of how the interplay of dipole and exchange interaction makes it possible to form a topological configurations in Phase-I, III and V, the following correlation functions are investigated:** Topological charge susceptibility

$$\chi_c(\mathbf{r}) = \int d^2\mathbf{r}' \rho(\mathbf{r}') \rho(\mathbf{r} + \mathbf{r}'). \quad (4.4.5)$$

The spin-non-flip (or skyrmion polarity) and spin-flip correlation functions

$$\begin{aligned} \chi_s^{zz}(\mathbf{r}) &= \int d^2\mathbf{r}' n_z(\mathbf{r}') n_z(\mathbf{r} + \mathbf{r}'), \\ \chi_s^{\pm}(\mathbf{r}) &= \int d^2\mathbf{r}' n_{+}(\mathbf{r}') n_{-}(\mathbf{r} + \mathbf{r}'), \end{aligned} \quad (4.4.6)$$

where $n_{\pm} = n_x \pm i n_y$. The Fourier transformation of the correlation function gives the structure factor $S_{c/s}(\mathbf{q})$. For the topological charge density, the topological structure factor mimics the XRD or TEM maps, except that this is not directly measurable and indirectly it can be mapped by Lorentz TEM.[242] The two spin structure factors are however measurable via small-angle neutron scattering (SANS) experiments.

First it is observed that in the non-trivial phases, the topological structure factor shows distinct Bragg peaks at $\mathbf{q} \rightarrow 0$, signifying the transnational symmetry breaking and formation of skyrmion lattice. (When the dynamics is added, this peak will disperse away from $\mathbf{q} = 0$ point as a typical acoustic Goldstone mode). In the trivial phase (Phase-II and Phase-IV), there is no Bragg peaks, but some weak intensity at higher Brillouin zone of the original Moiré supercell) which are often observed in dilute gas or liquid phases.

The spin-non-flip and spin slip components of the spin-structure factors have the usual behavior in a skyrmions structure, while the stark difference between the Phase-I and Phase-IV for the χ_s^{zz} should be noted. In the case of a ring charge (Phase-I) there is no $\mathbf{q} \rightarrow 0$ mode for the polarity density since here there is a sharp domain wall boundary between the up and down spin states. For all other cases, the $\mathbf{q} \rightarrow 0$ mode exists, suggesting a finite value of the magnetic moment in these cases on the top layer. On the other, in Phase-II, the total magnetization vanishes in a Moiré unit cell, however, if one defines Néel magnetization between the up spin domain and down-spin domain, there is an antiferromagnetic like domain wall ordering. In all cases, the spin-flip structure factor is similar, while an additional spatial rotational symmetry breaking is observed in Phases II and III as expected. It is found that that all the peaks are present in the second Brillouin zone which is due to the fact that the Moire cell here forms an honeycomb lattice which has two sublattices. The structure factors for topological charge are plotted in the Figs. 4.7(b) and 4.7(c). As expected, Bragg-like peaks are observed in Phase-III as the topological charges form a triangular lattice. The lattice also features a broken spatial rotation symmetry, and gives a smectic-like skyrmion lattice. In phase-II the charge centers do not exhibit any Bragg-like peak up to third Brillouin zone. As the appearance of the new Bragg-like peaks at the antiferromagnetic wavevector in the spin-spin correlation function indicate antiferromagnetic order, similar Bragg-like peaks in the dipole-dipole correlation function indicate an antiferroelectric ordering of the topological

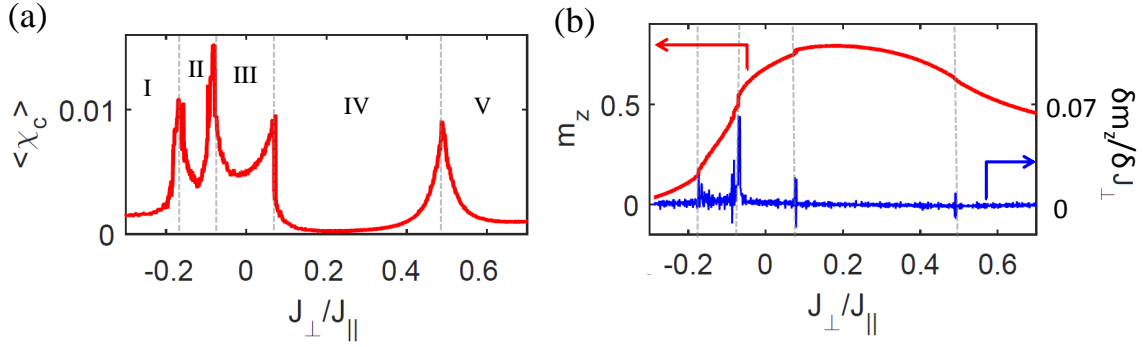


Figure 4.8: plot of (a) Average χ_c and (b) average magnetization (m_z) and derivative of m_z as a function of interlayer exchange (J_{\perp}/J_{\parallel}) at a fixed $J_D = 0.3J_{\parallel}$. Discontinuity in m_z at the phase transition can be seen from the jumps in derivative of m_z (blue curve in (b))

dipole moment.

To further elucidate the phase transition, I analyze the topological correlation function at a fixed distance ($r_i - r_j = \text{constant}$):

$$\chi_c = \frac{1}{N} \sum_{\langle i,j \rangle} \rho(\mathbf{r}_i) \rho(\mathbf{r}_j). \quad (4.4.7)$$

The result is plotted as a function of inter-layer exchange (J_{\perp}) in Fig. 4.8(a). This gives the short-range correlation of the topological charge density.

As shown in Fig. 4.8(a), the correlation has peaks at the phase transition points. This result is consistent with jumps in the effective magnetic field $M_z = \langle (1/N) \sum_i S_i^z \rangle$ along J_{\perp} , as shown in Fig. 4.8(b). Near the phase transition points, the landscape of effective magnetic field changes over the Moiré unit cell. As a result near the domain wall in each phase (except Phase IV where there is no domain wall) B field becomes small over a large area. Therefore, the Hamiltonian is mostly dominated by strong in-plane ferromagnetic exchange (J_{\parallel}), and produces a strong nearest neighbour correlation.

I further calculate scalar chirality (not shown) $\chi_{sc} = \frac{1}{N} \langle \sum_{\langle i,j,k \rangle} \mathbf{S}_i \cdot (\mathbf{S}_j \times \mathbf{S}_k) \rangle$, where $\langle i, j, k \rangle$ denotes three spins forming the smallest triangle in the honeycomb lattice. I find that the scalar chirality vanishes in Phase II and Phase IV, where the magnetization has a sharp jump at their phase boundary (Fig. 4.8(b)).

4.5 Discussions and Conclusions

So far, my discussions were primarily devoted to delineate the mechanism of skyrmion charges and antiskyrmion dipoles. Although not my primary focus here, it is worthwhile to outline few possible mechanism to destroy topological configurations, and the corresponding phase transitions. I discussed that the size of the compact domain wall (r_d) as it reduces to zero or expands all the way to the Moiré lattice vector as a function of J_{\perp}/J_D and the bilayer thickness d , it destroys the skyrmion configuration. Moreover, energetic makes another dominant factor to destabilizing the saddle-point minima of skyrmions. Once fluctuations are included, the topological charge centers oscillate, creating ‘phonon’ like excitations, which melt the skyrmion crystals.[265] I have studied the short range (nearest-neighbor) topological charge correlation function, and find that it exhibits a similar divergence behavior at all phase transition points (see Sec. 4.4.6). In addition, it is observed that the phase transition from Phase-II to Phase-III occurs via the coalescence of the antiskyrmion pairs and vanishing dipole moment. This is reminiscence of the Kosterlitz-Thouless (KT) like transition, but generalized to the $O(3)$ field.

Can one probe the topological electric field, dipole moment and the KT transition of the topological charge of the skyrmions? The electric field is the mediator of the force between two charge particles. Since a skyrmion charge is a topological charge, it cannot be destroyed without deforming all the spins in a skyrmion. This prohibits two skyrmions of the same charge to come close to each other – as if they experience a Coulomb repulsion between them. This phenomenon can be associated with an electric field. Much like how an electric field is measured by adding a test charge, here one can think of adding a test skyrmion in a skyrmion background, and study its dynamics. It will be found that the test skyrmion of same (opposite) charge will be repelled (attracted) from the skyrmion background. Similarly, when two skyrmions/antiskyrmions of opposite charges are spatially separated as in Phase-II, one can associate a dipole moment in the usual way. With tuning, the two opposite charges can either annihilate each other or the two charges can become unbound from each other. The second phenomena is analogous to the KT transition as seen in the vortex case. In the case of the KT transition in vortices, pairs of vortices of opposite charges are energetically favorable at low-temperature, which forms dipole moment and the material behaves as a dielectric. With increasing temperature, the vortex pairs split and the vortex charges become unbound, giving

a plasma like phase. The phase transition between them is denoted by the KT transition. In the present case, it can be speculated that a similar splitting of the dipole may occur with increasing temperature in Phase-II, giving us a unique opportunity to explore a possible KT transition of skyrmions.

Finally, the spin-spin correlation also plays an important role. I have calculated the transverse and longitudinal spin-spin correlation functions in the static limit. The transverse component does not have any $q \sim 0$ mode, and remains nearly unchanged across all the phases. The longitudinal susceptibility shows Bragg-like peaks in four phases, but not in Phase-I. Because, Phase-I is non magnetic.

One may wonder how sensitive is the the phase diagram to DMI and SOC terms. I have checked that DMI brings in very little change to the spin configurations, and their topological properties are robust as long as the DMI strength is considerably weaker than J_{\perp} (DMI coupling $J_{DMI} \sim 0.1J_D$). However, larger DMI interaction may have non-trivial effect since DMI can be highly non-perturbative. This can be taken as a new project for future studies. With an eye to synthesize twisted bilayers of VdW magnets,[87, 260] is it known that the spins are local in nature, and the materials are charge insulators. Thus the SOC does not play an important role to the skyrmion configurations.

Chapter 5

Conclusions and outlook

In this concluding chapter of the thesis, I briefly summarise the findings of my various studies, and their impact on the ongoing research in these fields. I also describe some extension and follow-up researches, which would be interesting topics for future studies.

One of my main projects was the study of coexistence of Fermi liquid (FL) and non-Fermi liquid (NFL) behaviour in hole-doped cuprates. My objective was to show that NFL state can emerge from spin fluctuation and thus, NFL and FL behavior can be described in a single self-consistent theoretical framework. By using a single-band tight-binding model with Hubbard interaction on a 2D square lattice, with parameters relevant for cuprates band structure, I calculated self-energy in a self-consistent manner by using a momentum-dependent density-fluctuation (MRDF) method. The computed self-energy exhibits a marginal-FL (MFL)-like frequency dependence only in the antinodal region, and FL-like behavior elsewhere at all dopings. I also calculated the DC conductivity by including the full momentum dependent self-energy which gives the resistivity-temperature exponent $n = 1$ near the optimal doping, indicating a NFL state. In the extreme NFL state (near the optimal doping in cuprates), MFL-like self-energy occupies the largest volume in momentum space but the nodal region still contains FL-like self-energies. Similarly, in the FL state (in overdoped region), not all quasiparticles are necessarily long-lived and the antinodal region remains NFL-like. These results highlight the non-local correlation physics in cuprates and in other similar intermediately correlated materials, where a direct link between the microscopic single-particle spectral properties and the macroscopic transport behavior cannot be well established. Thus, our study

shows that microscopic spectral landscape gives more complete picture of the underlying FL or NFL behavior which cannot be seen from the bulk macroscopic property like resistivity.

The present study, while predicts correct behavior in over-doped cuprates, does not include the effect of pseudogap in the under-doped region. Including the effect of pseudogap and study how the momentum anisotropy effects that region can be an interesting topic. Apart from cuprates, this study can be extended to other anisotropic material like transition metal oxides. That demands the present method to be extended to multiband models. Studying anisotropic correlations and its effect on the physical phenomena like topological order, entanglement entropy and related topics can be future prospects of the present study.

In the next part of the thesis, I studied various aspects like superconductivity, topology in twisted bilayer systems. We started with the unconventional superconductivity arising from spin fluctuation mechanism in twisted bilayer graphene (TBG) and compare the results with single layer graphene (SLG) and graphene on hexagonal boron nitride (GBN). Unlike SLG, TBG and GBN have formation of Moiré pattern. For these two systems I use the wave functions of the low energy bands, which leads to the Wannier functions localised in the Moiré unit cell. I propose the Wannier pairings in TBG and GBN and study the pairing symmetry and find *d*-wave pairing for SLG, *p*-wave pairing for GBN and extended *s*-wave pairing for TBG as the dominant pairing symmetry. This study also showed the emergence of superconductivity in TBG at the magic angle. A number of recent studies have shown similarities between superconducting phase diagrams of cuprates and TBG. So, the NFL behavior studied earlier in the context of cuprates can be extended for TBG. One can explore the role of twisted geometry and non-trivial interlayer coupling to give a NFL state.

In this thesis, I mainly focused on the superconductivity from electron-electron repulsive interactions. There are superconductors in which superconducting critical temperature T_c is dramatically enhanced when the material is rest on the SrTiO₃ substrate. In another example, there are experimental results of a thermal Hall effect in the correlated insulating phase in several materials. These results seem to hint towards a strong interplay between electron-electron as well as electron-phonon couplings in many correlated materials. One can extend the present spin fluctuation method to incorporate the electron-electron interaction and electron-phonon coupling to study those materials. The method will then be able to explain many recent experi-

mental puzzles as mentioned above. The method can further be extended to superconductivity due to plasmon and polaron, etc as well.

Apart from superconductivity, I studied spin textures in twisted bilayer geometry of 2D VdW magnets with Monte Carlo simulation. By including long ranged exchange and dipole-dipole interactions for interlayer coupling, I found a number of distinct skyrmion phases with point-, rod-, and ring-like topological charge distributions. A novel topological antiferroelectric phase is also found, where oppositely charged antiskyrmion pairs are formed, and the corresponding topological charge distribution shows a dipole formation in the Moire supercell. The dipoles become ordered in a Néel-like state. This work can be extended to explore various spin structure and spin topology in twisted bilayers of different lattice like hexagonal, triangular, square, Kagome etc. One can also think of two such bilayers with different skyrmionic structure and by bringing them together and study the interactions between skyrmions.

Topological aspects in electronic structure can also be explored in twisted bilayer hexagonal lattice. With an effective low-energy model to describe the electronic structure of twisted bi-layers of hexagonal and square lattice, one can look for topological electronic structure properties. One can also study the effect of intrinsic spin orbit coupling (SOC) and Rashba SOC in twisted bilayers. Such systems may give rise to time reversal invariant Z_2 topological insulators. The recently developed Green's function method described in chapter 1 can be useful in finding topological invariant in such systems due to the large system size.

References

- [1] L. D. Landau, The theory of a Fermi liquid, *J. Exptl. Theoret. Phys. (USSR)* **3**, 920-925 (1957).
- [2] L. D. Landau, On the theory of the Fermi liquid, *Sov. Phys. JETP* **8.1**, 70 (1959).
- [3] Piers Coleman, *Introduction to many-body physics*, Cambridge University Press (2015).
- [4] A. A. Abrikosov and I. M. Khalatnikov, The theory of a fermi liquid (the properties of liquid ^3He at low temperatures), *Reports on Progress in Physics*, **22**, 329 (1959).
- [5] P. Nozières and D. Pines, *The theory of quantum liquids*, W. A. Benjamin (1966).
- [6] G. Baym and C. Pethick, *Landau Fermi-Liquid Theory: concepts and applications*, J. Wiley (1991).
- [7] D. Pines, *Theory of Quantum Liquids: Normal Fermi Liquids*, CRC Press (2018).
- [8] I. I. Pomeranchuk, *Sov. Phys. JETP* **8**, 361 (1958).
- [9] [1] N. F. Mott, *Proc. Phys. Soc. (London)* **A62**, 416 (1949).
- [10] E. Thuneberg, *Introduction to Landau's Fermi Liquid Theory*, Dept. of Physical Sciences, University of Oulu (2009).
- [11] E. C. Stoner, *Proc. Roy. Soc. London* **A165**, 372 (1938).
- [12] V. M. Galitskii, *Soviet. Phys.-JETP*. **7**, 104 (1958).
- [13] P. Nozieres and J. Luttinger, *Phys. Rev.*, **127**, 1423 (1962).
- [14] J. M. Luttinger and P. Nozieres, *Phys. Rev.* **127**, 1431 (1962).

-
- [15] P. Nozières and A. Blandin, *J. Phys. France* **41**, 193 (1980).
- [16] N. Andrei and C. Destri, *Phys. Rev. Lett.* **52**, 364 (1984).
- [17] A. M. Tselik and P. B. Wiegmann, *Z. Phys. B: Condens. Matter* **54**, 201 (1984).
- [18] P. Schlottmann and P. D. Sacramento, *Adv. Phys.* **42**, 641 (1993).
- [19] V. Dobrosavljevic, T. R. Kirkpatrick and G. Kotliar, *Phys. Rev. Lett.* **69**, 1113 (1992).
- [20] R. N. Bhatt and D. S. Fisher, *Phys. Rev. Lett.* **68**, 3072 (1992).
- [21] M. A. Paalanen and R. N. Bhatt, *Physica B* **169**, 223 (1991).
- [22] M. A. Paalanen, S. Sachdev, R. N. Bhatt and A. E. Ruckenstein, *Phys. Rev. Lett.* **57**, 2061 (1986).
- [23] M. Lakner, H. v. Löhneysen, A. Langenfeld and P. Wölfle, *Phys. Rev. B* **50**, 17064 (1994).
- [24] G. R. Stewart, *Rev. Mod. Phys.* **73**, 797 (2001).
- [25] G. R. Stewart, *Rev. Mod. Phys.* **78**, 743 (2006).
- [26] A. Rosch, *Phys. Rev. Lett.* **82**, 4280 (1999).
- [27] A. H. Castro Neto, G. Castilla and B. A. Jones, *Phys. Rev. Lett.* **81**, 3531 (1998).
- [28] N. Rivier and K. Adkins, *J. Phys. F: Met. Phys.* **5**, 1745 (1975).
- [29] S. Sachdev, *Quantum Phase Transitions* (Cambridge University Press, Cambridge, England, 1999).
- [30] H. v. Löhneysen, A. Rosch, M. Vojta and P. Wölfle *Rev. Mod. Phys.* **79**, 1015 (2007).
- [31] J. A. Hertz, *Phys. Rev. B* **14**, 1165 (1976).
- [32] A. J. Millis, *Phys. Rev. B* **48**, 7183 (1993).
- [33] T. Moriya and T. Takimoto, *J. Phys. Soc. Jpn.* **64**, 960 (1995).
- [34] T. Moriya and A. Kawabata, *J. Phys. Soc. Jpn.* **34**, 639 (1973).

- [35] H. Hasegawa and T. Moriya, *J. Phys. Soc. Jpn.* **36**, 1542 (1974).
- [36] A. E. Ruckenstein and C. M. Varma, *Physica C: Superconductivity* **185–189**, Part 1, 134-140 (1991).
- [37] Chandra M. Varma, (Colloquium) *Rev. Mod. Phys.* **92**, 031001 (2020).
- [38] J. Bardeen, L. N. Cooper, and J. R. Schrieffer, *Phys. Rev.* **108**, 1175 (1957).
- [39] D. D. Osheroff, R. C. Richardson and D. M. Lee, *Phys. Rev. Lett.* **28**, 885-887 (1972).
- [40] F. Steglich, J. Aarts, C.D. Bredl, W. Lieke, D. Meschede, W. Franz and H. Schäfer, *Phys. Rev. Lett.* **43**, 1892 (1979).
- [41] H.R. Ott, H. Rudigier, Z. Fisk and J.L. Smith, *Phys. Rev. Lett.* **50**, 1595 (1983).
- [42] G.R. Stewart, Z. Fisk, J.O. Willis and J.L. Smith, *Phys. Rev. Lett.* **52**, 679 (1984).
- [43] P. Hohenberg and W. Kohn, *Phys. Rev.* **136**, B864 (1964).
- [44] N. F. Berk, J. R. Schrieffer, *Phys. Rev. Lett.* **17**, 433 (1966).
- [45] D. Scalapino, E. Loh, J Hirsch, *Phys. rev. B* **34**, 8190 (1986); *Phys. rev. B* **35**, 6694 (1987).
- [46] A.G. Abanov and P.B. Wiegmann, Theta-terms in nonlinear sigma-models, *Nuclear Physics B*, **570**, FS 685–698 (2000).
- [47] M. V. Berry, Quantal phase factors accompanying adiabatic changes, *Proc. R. Soc. London Ser. A* **392**, 45-57 (1984).
- [48] M. Nakahara, *Geometry topology and physics*, Institute of physics publishing Bristol and Philadelphia (1990).
- [49] D. J. Thouless, M. Kohmoto, M. P. Nightingale, and M. den Nijs, *Phys. Rev. Lett.* **49**, 405 (1982).
- [50] D. J. Thouless, *Phys. Rev. B* **27**, 6083 (1983).

- [51] Q. Niu and D. J. Thouless, *J. Phys. A: Math. Gen.* **17**, 2453-2462 (1984).
- [52] B.I. Halperin, *Phys. Rev. B* **25**, 2185 (1982).
- [53] C. L. Kane and E. J. Mele, *Phys. Rev. Lett.* **95**, 226801 (2005).
- [54] C. L. Kane and E. J. Mele, *Phys. Rev. Lett.* **95**, 146802 (2005).
- [55] L. Fu and C. L. Kane, *Phys. Rev. B* **76**, 045302 (2007).
- [56] J. E. Moore¹ and L. Balents, *Phys. Rev. B* **75**, 121306(R).
- [57] L. Fu and C. L. Kane, *Phys. Rev. B* **74**, 195312 (2006).
- [58] T. Misawa and Y. Yamaji, Zeros of green functions in topological insulators, arxiv:2102.04665v1.
- [59] T. H. R. Skyrme, *Nucl. Phys.* **31**, 556–569 (1962).
- [60] S. L. Sondhi, A. Karlhede, S. A. Kivelson and E. H. Rezayi, *Phys. Rev. B* **47**, 16419–16426 (1993).
- [61] D. C. Wright and N. D. Mermin, *Rev. Mod. Phys.* **61**, 385–432 (1989).
- [62] T. L. Ho, *Phys. Rev. Lett.* **81**, 742–745 (1998).
- [63] U. K. Röβler, N. Bogdanov and C. Pfleiderer, *Nature* **442**, 797–801 (2006).
- [64] N. Bogdanov and D. A. Yablonskii, *Sov. Phys. JETP* **68**, 101–103 (1989).
- [65] R. Rajaraman, *Solitons and Instantons* (Elsevier, 1987).
- [66] H. -B. Braun, *Adv. Phys.* **61**, 1–116 (2012).
- [67] B. M. Tanygin, *Physica B* **407**, 868–872 (2012).
- [68] N. Nagaosa and Y. Tokura, *Nature Nanotechnology* **8**, 899–911 (2013).
- [69] S. Mühlbauer, *et al.*, *Science* **323**, 915 (2009).

- [70] Y. S. Lin, J. Grundy, and E. A. Giess, *Appl. Phys. Lett.* **23**, 485–487 (1973); A. P. Malozemoff, and J. C. Slonczewski, *Magnetic Domain Walls in Bubble Materials* 306–314 (Academic, 1979).; T. Garel, and S. Doniach, *Phys. Rev. B* **26**, 325–329 (1982); T. Suzuki, *J. Magn. Magn. Mater.* **31–34**, 1009–1010 (1983); B. Göbel, J. Henk, I. Mertig, *Sci. Reports* **9**, 9521 (2019). M. Ezawa, *Phys. Rev. Lett.* **105**, 197202 (2010).
- [71] A. N. Bogdanov and A. Hubert, *Sov.Phys.JETP* **68**, 101-103 (1989); *J. Magn. Magn. Mater.* **138**, 255-269 (1994); U. K. Roessler, A. N. Bogdanov, and C. Pfleiderer, *Nature* **442**, 797-801 (2006).
- [72] S. Rohart, and A. Thiaville, *Phys. Rev. B* **88**, 184422 (2013).
- [73] M. Hoffmann, B. Zimmermann, G. P. Muller, D. Schurhoff, N. S. Kiselev, C. Melcher, and S. Blugel. *Nat. comm.* **8**, 308 (2017).
- [74] E. Y. Vedmedenko, J. A. Arregi, P. Riego, A. Berger. *Phys. Rev. Lett.* **122**, 257 (2019)
- [75] S. Rohart and A. Thiaville, *Phys. Rev. B Condens. Matter Mater. Phys.* **88**, 184422 (2013).
- [76] B. Dupé, G. Bihlmayer, M. Böttcher, S. Blügel, and S. Heinze, *Nat. Commun.* **7**, 11779 (2016).
- [77] T. Okubo, S. Chung and H. Kawamura, *Phys. Rev. Lett.* **108**, 017206 (2012).
- [78] A. O. Leonov, and M. Mostovoy, *Nat. Commun.* **6**, 8275 (2015).
- [79] C. D. Batista, S. Z. Lin, S. Hayami, and Y. Kamiya, *Rep. Prog. Phys.* **79**, 084504 (2016).
- [80] T. Okubo, S. Chung, and H. Kawamura, *Phys. Rev. Lett.* **108**, 017206 (2012); A. Leonov, and M. and Mostovoy, *Nat. Commun.* **6**, 8275 (2015); S. Hayami, S. -Z. Lin, and Cristian D. Batista *Phys. Rev. B* **93**, 184413 (2016); C. D. Batista, S. -Z. Lin, S. Hayami, and K. Yoshitomo, *Reports on Progress in Physics*, **79**, 084504 (2016).
- [81] S. Banerjee, O. Erten, and M. randeria, *Nature Physics* **9**, 626-630 (2013).
- [82] R. Ozawa, S. Hayami, and Y. Motome, *Phys. Rev. Lett.* **118**, 147205 (2017).

- [83] I. Gross, W. Akhtar, A. Hrabec, J. Sampaio, L. J. Martinez, S. Chouaieb, B. J. Shields, P. Maletinsky, A. Thiaville, S. Rohart, and V. Jacques, *Phys. Rev. Mater.* **2**, 024406 (2017).
- [84] S. L. Sondhi, A. Karlhede, S. A. Kivelson, and E. H. Rezayi, *Phys. Rev. B* **47**, 16419 (1993).
- [85] L. S. Leslie, A. Hansen, K. C. Wright, B. M. Deutsch, and N. P. Bigelow, *Phys. Rev. Lett.* **103**, 250401 (2009).
- [86] A. H. C. Neto, F. Guinea, N. M. R. Peres, K. S. Novoselov, and A. K. Geim, *Rev. Mod. Phys.* **81**, 109 (2009).
- [87] M. A. McGuire, H. Dixit, V. R. Cooper, and B. C. Sales, *Chem. Mater.* **27**, 612–620 (2015); B. Huang, G. Clark, E. N. -Moratalla, D. R. Klein, R. Cheng, K. L. Seyler, D. Zhong, E. Schmidgall, M. A. McGuire, D. H. Cobden, W. Yao, D. Xiao, P. J. -Herrero, and X. Xu, *Nature* **546**, 270–273 (2017).
- [88] P. Moon and M. Koshino, *Phys. Rev. B* **90**, 155406 (2014).
- [89] R. Bistritzer, A.H. MacDonald, *Proc. Nat. Acad. Sci. (USA)* **108**, 12233 (2011).
- [90] N. Sivadas, S. Okamoto, X. Xu, C. J. Fennie, D. Xiao, *Nano Lett.* **18**, 7658-7664 (2018).
- [91] K. Hejazi, Z. -X. Luo, and L. Balents, *PNAS* **117**, 10721-10726 (2020).
- [92] Y. Cao, V. Fatemi, S. Fang, K. Watanabe, T. Taniguchi, E. Kaxiras, P. Jarillo-Herrero, *Nature* **556**, 43-50 (2018).
- [93] E. Y. Andrei, and A. H. MacDonald, *Nature Materials* **19**, 1265–1275 (2020).
- [94] F. Wu, A. H. MacDonald, and I. Martin, *Phys. Rev. Lett.* **121**, 257001 (2018).
- [95] F. Wu, T. Lovorn, E. Tutuc, I. Martin, and A. H. MacDonald, *Phys. Rev. Lett.* **122**, 086402 (2019).
- [96] T. Senthil, S. Sachdev and M. Vojta , *Phys. Rev. Lett.* **90**, 216403 (2003); T. Senthil, M. Vojta and S. Sachdev, *Phys. Rev. B* **69**, 035111 (2004); Kai-Yu Yang, T. M. Rice and

- Fu-Chun Zhang, Phys. Rev. B **73**, 174501 (2006); Y. Qi and S. Sachdev, Phys. Rev. B **81**, 115129 (2010).
- [97] A. J. Millis, H. Monien, and D. Pines, Phys. Rev. B **42**, 167 (1990).
- [98] S. Lederer, Y. Schattner, E. Berg, S. A. Kivelson, Proc. Nat. Acad. Sci. **114**, 4905 (2017).
- [99] R. Nandkishore, Max A. Metlitski, T. Senthil, Phys. Rev. B **86**, 045128 (2012); Max A. Metlitski, David F. Mross, Subir Sachdev, and T. Senthil, *ibid.* **91**, 115111 (2015); David F. Mross and T. Senthil, *ibid.* **84**, 165126 (2011).
- [100] S. -S. Lee, arXiv:1703.08172.
- [101] T. Das and C. Panagopoulos, New J. Phys. **18**, 103033 (2016).
- [102] H. Kontani, Rep. Prog. Phys. **71**, 026501 (2008).
- [103] S. L. Sondhi, S. M. Girvin, J. P. Carini, and D. Shahar, Rev. Mod. Phys. **69**, 315 (1997).
- [104] S. Sachdev, *Quantum Phase Transition* (Cambridge Univ. Press, Cambridge, 1999).
- [105] M. Vojta, Rep. Prog. Phys. **66**, 2069 (2003).
- [106] H. v. Löhneysen, A. Rosch, M. Vojta, and P. Wölfle, Rev. Mod. Phys. **79**, 1016 (2007).
- [107] A. V. Chubukov, and D. L. Maslov, Phys. Rev. B **68**, 155113 (2003); **69**, 121102(R) (2004); A. V. Chubukov, D. L. Maslov, and A. J. Millis, *ibid.* **73**, 045128 (2006); D.L. Maslov, A.V. Chubukov, and R. Saha, *ibid* **74**, 220402(R) (2006).
- [108] Ar. Abanov and A. V. Chubukov, Phys. Rev. Lett. **93**, 255702 (2004);
- [109] A. V. Chubukov, D. L. Maslov, S. Gangadharaiah, and L. I. Glazman, Phys. Rev. B **71**, 205112 (2005).
- [110] T. Senthil, Leon Balents, Subir Sachdev, Ashvin Vishwanath, and Matthew P. A. Fisher, Phys. Rev. B **70**, 144407 (2004); T. Senthil, Matthias Vojta, and Subir Sachdev, *ibid.* **69**, 035111 (2004).
- [111] S. Sachdev, N. Read, and R. Oppermann, Phys. Rev. B **52**, 10286 (1995).

- [112] G.R. Stewart, *Rev. Mod. Phys.* **73**, 797 (2001).
- [113] S. Sachdev, *Rev. Mod. Phys.* **75**, 913 (2003).
- [114] P. Coleman and A.J. Schofield, *Nature* **433**, 226-229 (2005)
- [115] L. Taillefer, *La Physique Au Canada* **67**, 109 (2011).
- [116] T. Shibauchi, A. Carrington and Y. Matsuda, *Annu. Rev. Cond. Mat. Phys.* **5**, 113-135 (2014).
- [117] N. Doiron-Leyraud, P. Auban-Senzier, S.R. de Cotret, A. Sedeki, C. Bourbonnais, D. Jerome, K. Bechgaard and L. Taillefer, *ArXiv:0905.0964* (2009).
- [118] P. Gegenwart, Q. Si and F. Steglich, *Nature Physics* **4**, 186 (2008) .
- [119] J. Chang *et al.*, *Nature communications* **4**, (2013).
- [120] M. Abdel-Jawad, M.P. Kennett, L. Balicas, A. Carrington, A.P. Mackenzie, R.H. McKenzie, and N.E. Hussey, *Nature Phys.* **2**, 821 (2006).
- [121] M. M. J. French, J. G. Analytis, A. Carrington, L. Balicas, and N. E. Hussey, *New J. Phys.* **11**, 055057 (2009).
- [122] S. Kambe, H. Sakai, Y. Tokunaga, G. Lapertot, T. D. Matsuda, G. Knebel, J. Flouquet, and R. E. Walstedt, *Nature Physics* **10**, 840–844 (2014).
- [123] T. Das, R.S. Markiewicz and A. Bansil, *Advances in Physics* **63**, 151-266 (2014).
- [124] T. Das, J.-X. Zhu and M. J. Graf, *Phys. Rev. Lett.* **108**, 017001 (2012).
- [125] T. Das, and K. Dolui, *Phys. Rev. B* **91**, 094510 (2015),
- [126] R.S. Dhaka, T. Das, N.C. Plumb, Z. Ristic, W. Kong, C.E. Matt, N. Xu, K. Dolui, E. Razzoli, M. Medarde, L. Patthey, M. Shi, M. Radovic and J. Mesot, *Phys. Rev. B* **92**, 035127 (2015).

- [127] X. Yin, S. Zeng, T. Das, G. Baskaran, T. C. Asmara, I. Santoso, X. Yu, C. Diao, P. Yang, M. B. H. Breese, T. Venkatesan, H. Lin, Ariando, A. Rusydi, Phys. Rev. Lett. **116** 197002 (2016).
- [128] S. Sachdev, A. V. Chubukov, and A. Sokol, Phys. Rev. B **51**, 14874 (1995).
- [129] C. Panagopoulos, J. L. Tallon, B. D. Rainford, T. Xiang, J. R. Cooper, and C. A. Scott, Phys. Rev. B **66**, 064501 (2002).
- [130] M.-H. Julien, Physica B **329**, 693–6 (2003).
- [131] M. A. Metlitski, S. Sachdev, Phys. Rev. B **82**, 075128 (2010).
- [132] M. P. M. Dean *et al.*, Nature Mat. **12**, 1019–2023 (2013).
- [133] M. Jarrell, Th. Maier, M. H. Hettler, and A. N. Tahvildarzadeh, Europhys. Lett. **56**, 563–569 (2001).
- [134] N. E. Bickers and D. J. Scalapino, Ann. Phys. (N. Y.), **193**, 206–251 (1989); N. E. Bickers, D. J. Scalapino, and S R White, Phys. Rev. Lett., **62**, 961–964 (1989); N. E. Bickers, and S. R. White, Phys. Rev. B **43**, 8044 (1991).
- [135] J. A. Hertz, Phys. Rev. B **14**, 1165 (1976); A. J. Millis, *ibid.* **48**, 7183 (1993).
- [136] P. Monthoux, and D. Pines, Phys. Rev. B **47**, 6069 (1993); T. Dahm and L. Tewordt, Phys. Rev. B **52**, 1297 (1995); Y. Yanase, and K. Yamada, J. Phys. Soc. Jpn. **68**, 548–560 (1999).
- [137] T. Das, R.S. Markiewicz, and A. Bansil, Phys. Rev. B **81**, 184515 (2010).
- [138] T. Moriya, Y. Takahashi, and K. Ueda, J. Phys. Soc. Japan. **59**, 2905 (1990); K. Ueda, T. Moriya, and Y. Takahashi, J. Phys. Chem. Solids **53**, 1515 (1992); T. Moriya, and K. Ueda, Adv. Phys. **49**, 555 (2000).
- [139] B. L. Altshuler, L. B. Ioffe, and A. J. Millis, Phys. Rev. B **50**, 14048 (1994); A. Liam Fitzpatrick, Shamit Kachru, Jared Kaplan, and S. Raghu, *ibid.* **88**, 125116 (2013), **89**, 165114 (2014); P. Sätterskog, B. Meszner, and K. Schalm, arXiv:1612.05326.

- [140] D. F. Mross, J. McGreevy, H. Liu, and T. Senthil, *Phys. Rev. B* **82**, 045121 (2010).
- [141] S. Chakravarty, R. E. Norton, and O. F. Syljuasen, *Phys. Rev. Lett.* **74**, 1423 (1995); I. Mandal, and Sung-Sik Lee, *Phys. Rev. B* **92**, 035141 (2015).
- [142] A. Abanov, and A. V. Chubukov, *Phys. Rev. Lett.* **84**, 5608 (2000); R. Haslinger, A. V. Chubukov, and A. Abanov, *Phys. Rev. B*, **63**, 020503 (2001); A. Abanov, A. V. Chubukov, and J. Schmalian, *Adv. Phys.* **52**, 119-218 (2003).
- [143] S. Nakatsuji, D. Pines, and Z. Fisk, *ibid.* **92**, 016401 (2004); Yi-feng Yang and D. Pines, *Phys. Rev. Lett.* **100**, 096404 (2008).
- [144] N. Nagaosa and P. A. Lee, *Phys. Rev. Lett.* **64**, 2450 (1990); P. A. Lee and N. Nagaosa, *Phys. Rev. B* **46**, 5621 (1992).
- [145] H. -C. Jiang, M. S. Block, R. V. Mishmash, J. R. Garrison, D. N. Sheng, O. I. Motrunich, M. P. A. Fisher, *Nature* **493**, 39-44 (2013).
- [146] W. Xu, K. Haule and G. Kotliar, *Phys. Rev. Lett.* **111**, 036401 (2013); X. Deng, J. Mravlje, R. Zitko, M. Ferrero, G. Kotliar and A. Georges, *Phys. Rev. Lett.* **110**, 086401 (2013); X. Deng, A. Sternbach, K. Haule, D.N. Basov and G. Kotliar, *Phys. Rev. Lett.* **113**, 246404 (2014).
- [147] W. Xu, G. Kotliar and A.M. Tsvelik, *Phys. Rev. B* **95**, 121113 (2017).
- [148] D. Bergeron, D. Chowdhury, M. Punk, S. Sachdev and A.-M.S. Tremblay, *Phys. Rev. B* **86**, 155123 (2012)
- [149] R. A. Davison, K. Schalm and J. Zaanen, *Phys. Rev. B* **89**, 245116 (2014); J. Zaanen, Y.-W. Sun, Y. Liu, K. Schalm, *Holographic Duality for Condensed Matter Physics* (Cambridge Univ. Press, 2015); Sung-Sik Lee, *Phys Rev D* **79**, 086006 (2009); Thomas Faulkner, Nabil Iqbal, Hong Liu, John McGreevy, David Vegh, arXiv:1003.1728; Raghu Mahajan, Maissam Barkeshli, and Sean A. Hartnoll, *Phys. Rev. B* **88**, 125107 (2013).
- [150] S.-S. Lee, *Phys. Rev. B* **80**, 165102 (2009); D. Dalidovich and S.-S. Lee, *Phys. Rev. B* **88**, 245106 (2013); I. Mandal and S.-S. Lee, *Phys. Rev. B* **92**, 035141 (2015).

- [151] C. M. Varma, P. B. Littlewood, S. Schmitt-Rink, E. Abrahams and A. E. Ruckenstein, Phys. Rev. Lett. **64**, 497 (1990); C. M. Varma, Phys. Rev. B **55**, 14554 (1997).
- [152] N. S. Vidhyadhiraja, A. Macridin, C. Sen, M. Jarrell and M. Ma, Phys. Rev. Lett. **102**, 206407 (2009).
- [153] R. Preuss, W. Hanke, C. Gröber, and H. G. Evertz, Phys. Rev. Lett. **79**, 1122 (1997).
- [154] A. Comanac, L. de' Medici, M. Capone, A. J. Millis, Nature Physics **4**, 287 - 290 (2008).
- [155] C. Weber , Kristjan Haule, and Gabriel Kotliar, Nature Physics **6**, 574-578 (2010).
- [156] R.S. Markiewicz, Tanmoy Das, S. Basak, and A. Bansil, J. Elect. Spect. Rel. Phenom. **181** 23-27 (2010).
- [157] E. Pavarini, I. Dasgupta, T. Saha-Dasgupta, O. Jepsen and O.K. Andersen, Phys. Rev. Lett. **87**, 047003 (2001).
- [158] R. S. Markiewicz, S. Sahrakorpi, M. Lindroos, Hsin Lin, and A. Bansil, Phys. Rev. B **72**, 054519 (2005).
- [159] E. E. Salpeter, and H. A. Bethe, Phys. Rev. **84**, 1232 (1951).
- [160] K. Maki, Progress of Theoretical Physics **39**, 897 (1968); **40**, 193 (1968); K. Maki, Journal of Low Temperature Physics **1**, 513 (1969); R. S. Thompson, Phys. Rev. B **1**, 327 (1970).
- [161] L. Aslamasov and A. Larkin, Physics Letters A **26**, 238 (1968).
- [162] L. Hedin, Phys. Rev. **139**, A796 (1965); L. Hedin and S. Lundqvist, in Solid State Physics, edited by F. Seitz *et al.* (Academic, New York, 1969), Vol. 23, p. 1.
- [163] L. Hedin, J. Phys. Condens. Matter. **11**, R489 (1999); G. Onida, L. Reining and A. Rubio, Rev. Mod. Phys. **74**, 601 (2002); G. F. Giuliani and G. Vignale, Quantum Theory of the Electron Liquid, *Cambridge University Press*, Chapter 8 (2005).

- [164] F. Aryasetiawan, and O. Gunnarsson, Rep. Prog. Phys. **61**, 237 (1998); W. G. Aulbur *et al.*, in Solid State Physics, edited by H. Ehrenreich and F. Spaepen (Academic, New York, 2000), **54**, p. 1.
- [165] H. Kontani, J. Phys. Soc. Jpn. **75**, 013703 (2006); S. Onari, H. Kontani, and Y. Tanaka, Phys. Rev. B **73**, 224434 (2006).
- [166] J. C. Ward, Phys. Rev. **78**, 182 (1950).
- [167] Gerald D. Mahan, Many-Particle Physics, *Plenum Press, New York*, Chapter 3,9 (1990).
- [168] L. Braicovich, *et al.* Phys. Rev. Lett **104**, 077002 (2010); M.P.M. Dean, *et al.* Nat. Mat. **12**, 1019–1023 (2013); M. Le Tacon, *et al.*, Phys. Rev. B **88**, 020501(R) (2013); S. Wakimoto, *et al.* Phys. Rev. B **91**, 184513 (2015).;
- [169] W. F. Brinkman and T. M. Rice, Phys. Rev. B **2**, 4302 (1970).
- [170] T. Das, R. S. Markeiwcz, and A. Bansil, Phys. Rev. B **85**, 144526 (2012).
- [171] S. Schmitt, Phys. Rev. B **82**, 155126 (2010).
- [172] L. Q. Doung, and T. Das, Phys. Rev. B **96**, 125154 (2017).
- [173] S. A. Hartnoll, D. M. Hofman, M. A. Metlitski, S. Sachdev, Phys. Rev. B **84**, 125115 (2011).
- [174] D. Bergeron, V. Hankevych, B. Kyung, and A.-M. S. Tremblay, Phys. Rev. B **84**, 085128 (2011).
- [175] T. Moriya, *Spin Fluctuations in Itinerant Electron Magnetism* (Berlin: Springer) (1985).
- [176] R. A. Cooper, Y. Wang, B. Vignolle, O. J. Lipscombe, S. M. Hayden, Y. Tanabe, T. Adachi, Y. Koike, M. Nohara, H. Takagi, Cyril Proust, N. E. Hussey, Science **323**, 603-607 (2009).
- [177] D. Pines and Ph. Nozieres, The Theory of Quantum Liquids, Cambridge, Massachusetts, Perseus books (1999).

- [178] T. Timusk and B. Statt, *Rep. Prog. Phys.* **62**, 61 (1999); D. N. Basov and T. Timusk, *Rev. Mod. Phys.* **77**, 721 (2005).
- [179] A. Abanov, A. V. Chubukov, *Phys. Rev. Lett.* **88**, 217001 (2002).
- [180] S. S. Kancharla, B. Kyung, D. Senechal, M. Civelli, M. Capone, G. Kotliar, A.-M.S. Tremblay, *Phys. Rev. B* **77**, 184516 (2008).
- [181] A. Macridin, M. Jarrell, T. Maier, and D. J. Scalapino, *Phys. Rev. Lett.* **99**, 237001 (2007).
- [182] H. Kontani, K. Kanki, and K. Ueda, *Phys. Rev. B* **59**, 14723 (1999).
- [183] T. Miyake, C. Martins, R. Sakuma, and F. Aryasetiawan, *Phys. Rev. B* **87**, 115110 (2013).
- [184] P. Ghaemi, T. Senthil, and P. Coleman, *Phys. Rev. B* **77**, 245108 (2008).
- [185] S. Sur and S.-S. Lee, *Phys. Rev. B* **91**, 125136 (2015).
- [186] W. Metzner, D. Rohe, and S. Andergassen, *Phys. Rev. Lett.* **91**, 066402 (2003).
- [187] Y. Takada, *Phys. Rev. Lett.* **87**, 226402 (2001).
- [188] B. L. Altshuler, L. B. Ioffe, and A. J. Millis, *Phys. Rev. B* **50**, 14048 (1994).
- [189] A. M. Black-Schaffer, Se. Doniach, *Phys. Rev. B* **75**, 134512 (2007); B. Uchoa and A. H. Castro Neto, *Phys. Rev. Lett.* **98**, 146801 (2007); Y. Jiang, D.-X. Yao, E. W. Carlson, H.-D. Chen, J. Hu, *Phys. Rev. B* **77**, 235420 (2008); S. Pathak, V. B. Shenoy, G. Baskaran, *Phys. Rev. B* **81**, 085431 (2010); R. Nandkishore, L. Levitov, A. Chubukov, *Nat. Phys.* **8**, 158-163 (2012); G.-W. Chern, R. M. Fernandes, R. Nandkishore, A. V. Chubukov, *Phys. Rev. B* **86**, 115443 (2012).
- [190] Y. Cao, V. Fatemi, A. Demir, S. Fang, S. L. Tomarken, J. Y. Luo, J. D. Sanchez-Yamagishi, K. Watanabe, T. Taniguchi, E. Kaxiras, R. C. Ashoori, P. Jarillo-Herrero, *Nature* **556**, 80-84 (2018).
- [191] J. Jung, A. Raoux, Z. Qiao, A. H. MacDonald, *Phys. Rev. B* **89**, 205414 (2014).

- [192] D. Wong, Y. Wang, J. Jung, S. Pezzini, A. M. DaSilva, H. Z. Tsai, H. S. Jung, R. Khajeh, Y. Kim, J. Lee, S. Kahn, S. Tollabimazraehno, H. Rasool, K. Watanabe, T. Taniguchi, A. Zettl, S. Adam, A. H. MacDonald, M. F. Crommie, *Phys. Rev. B* **92**, 155409 (2015).
- [193] M. Koshino, N. F. Q. Yuan, T. Koretsune, M. Ochi, K. Kuroki, L. Fu, *Phys. Rev. X* **8**, 031087 (2018); D. M. Kennes, J. Lischner, C. Karrasch, *Phys. Rev. B* **98**, 241407(R) (2018).
- [194] D. M. Kennes, J. Lischner, C. Karrasch, *Phys. Rev. B* **98**, 241407(R) (2018).
- [195] K. Takada, H. Sakurai, E. T. -Muromachi, F. Izumi, R. A. Dilanian, and T. Sasaki, *Nature* **422**, 53-55 (2003); M. L. Kiesel, C. Platt, W. Hanke, and R. Thomale, *Phys. Rev. Lett.* **111**, 097001 (2013); K. S. Chen, Z. Y. Meng, U. Yu, S. Yang, M. Jarrell, J. Moreno, *Phys. Rev. B* **88**, 041103(R) (2013).
- [196] A. H. Castro Neto, F. Guinea, N. M. R. Peres, K. S. Novoselov and A. K. Geim, *Rev. Mod. Phys.* **81**, 109 (2009).
- [197] K. Kim, A. DaSilva, S. Huang, B. Fallahazad, S. Larentis, T. Taniguchi, K. Watanabe, B. J. LeRoy, A. H. MacDonald and E. Tutuc, *Proc. Nat. Acad. Sci. (USA)* **114**, 3364 (2017).
- [198] D. J. Scalapino, *Rev. Mod. Phys.* **84**, 1383 (2012); A. V. Chubukov, D. Pines, J. Schmalian, In: Bennemann K.H., Ketterson J.B. (eds) *The Physics of Superconductors*. Springer, Berlin, Heidelberg;
- [199] D. J. Scalapino, E. Loh, Jr., and J. E. Hirsch, *Phys. Rev. B* **34**, 8190 (R) (1986); *Phys. Rev. B* **34**, 6420 (1986) J. R. Schrieffer, X. G. Wen, and S. C. Zhang, *Phys. Rev. B* **39**, 11663 (1989); P. Monthoux, A. V. Balatsky, and D. Pines, *Phys. Rev. Lett.* **67**, 3448 (1991); Manfred Sigrist and Kazuo Ueda, *Rev. Mod. Phys.* **63**, 239 (1991); D. J. Scalapino, *Rev. Mod. Phys.* **84**, 1383 (2012).
- [200] I. I. Mazin, D. J. Singh, M. D. Johannes, and M. H. Du, *Phys. Rev. Lett.* **101**, 057003S (2008); S. Graser, T. A. Maier, P. J. Hirschfeld, D. J. Scalapino, *New J. Phys.* **11**, 025016 (2009); Zi-Jian Yao, Jian-Xin Li, and Z D Wang, *New J. Phys.* **11**, 025009 (2009); T. Das,

- A. V. Balatsky, Phys. Rev. B **84**, 014521 (2011); T. Das, Europhys. J.: Web of Conference **23**, 00014 (2012); Andrey Chubukov, Ann. Rev. Condens. Mat. Phys. **3**, 57-92 (2012).
- [201] T. Takimoto, T. Hotta, and K. Ueda, Phys. Rev. B **69**, 104504 (2004); K. Kubo, Phys. Rev. B **69**, 104504 (2004); T. Das, J.-X. Zhu, M. J. Graf, Sci. Rep. **5**, 8632 (2015); H. Ikeda, M.-T. Suzuki, R. Arita, Phys. Rev. Lett. **114**, 147003 (2015); T. Nomoto, H. Ikeda, Phys. Rev. Lett. **117**, 217002 (2016); T. Nomoto, H. Ikeda, J. Phys. Soc. Jpn. **86**, 023703 (2017).
- [202] J. Schmalian, Phys. Rev. Lett. **81**, 4232 (1998).
- [203] J. Jung and A. H. MacDonald, Phys. Rev. B **87**, 195450 (2013).
- [204] E. H. Hwang and S. Das Sarma, Phys. Rev. B **75**, 205418 (2007)
- [205] X.-F. Wang and T. Chakraborty, Phys. Rev. B **75**, 033408 (2007)
- [206] C. Kumar, M. Kuri, J. Jung, Tanmoy Das, A. Das, Nano Letters **16**, 1042-1049 (2016).
- [207] A. M. Black-Schaffer and C. Honerkamp J. Phys. Condens. Matter **26**, 423201 (2014).
- [208] M. Y. Kagan, V. V. Val'kov, V. A. Mitskan, M. M. Korovushkin, Solid State Communications **188**, 61–66 (2014).
- [209] A. P. Mackenzie, and Y. Maeno, Rev. Mod. Phys. **75**, 657 (2003).
- [210] J. A. Sauls, Adv. Phys. **43**, 113-141 (1994).
- [211] H. Guo, X. Zhu, S. Feng, and R. T. Scalettar, arXiv:1804.00159; T. Huang, L. Zhang, T. Ma, arXiv:1804.06096; J. F. Dodaro, S. A. Kivelson, Y. Schattner, X.-Q. Sun, C. Wang, arXiv:1804.03162; C.-C. Liu, L.-D. Zhang, W.-Q. Chen, and F. Yang, Phys. Rev. Lett. **121**, 217001 (2018).
- [212] B. Roy, V. Juricic, arXiv:1803.11190.
- [213] G. Baskaran, arXiv:1804.00627.

- [214] T. A. Maier and D. J. Scalapino, *Phys. Rev. B* **78**, 020514(R) (2008); I. I. Mazin and V. M. Yakovenko, *Phys. Rev. Lett.* **75**, 4134 (1995); D. K. Morr, P. F. Trautman, and M. J. Graf, *Phys. Rev. Lett.* **86**, 5978 (2001).
- [215] T. Hanaguri, Y. Kohsaka, M. Ono, M. Maltseva, P. Coleman, I. Yamada, M. Azuma, M. Takano, K. Ohishi, H. Takagi, *Science*, **323**, 923-926 (2009); T. Hanaguri, S. Niitaka, K. Kuroki, H. Takagi, *Science* **328**, 474-476 (2010); Tanmoy Das, and A. V. Balatsky, *J. Phys.: Cond. Mat. (First Track Comm.)* **24**, 182201 (2012).
- [216] A. V. Balatsky, I. Vekhter, and Jian-Xin Zhu, *Rev. Mod. Phys.* **78**, 373 (2006).
- [217] X. Wang, K. Du, Y. Y. F. Liu, P. Hu, J. Zhang, Q. Zhang, M. H. S. Owen, X. Lu, C. K. Gan, and P. Sengupta, *2D Materials* **3**, 3, 031009 (2016).
- [218] J. U. Lee, S. Lee, J. H. Ryoo, S. Kang, T. Y. Kim, P. Kim, C. H. Park, J. G. Park, and H. Cheong, *Nano Lett.* **16**, 12, 7433-7438 (2016).
- [219] P. A. Joy, and S. Vasudevan, *Phys. Rev. B* **46**, 5425-5433 (1992).
- [220] C. C. Mayorga-Martinez, Z. Sofer, D. Sedmidubsky, S. Huber, A. Y. S. Eng, and M. Pumera, *ACS Appl. Mater. Interfaces* **9**, 12563–12573 (2017).
- [221] Z. Fei, B. Huang, P. Malinowski, W. Wang, T. Song, J. Sanchez, W. Yao, D. Xiao, X. Zhu, A. F. May, W. Wu, D. H. Cobden, J. -H. Chu, and X. Xu, *Nat. Materials*, **17**, 778–782 (2018).
- [222] H. J. Deiseroth, K. Aleksandrov, C. Reiner, L. Kienle, and R. K. Kremer, *Eur. J. Inorg. Chem.*, 1561–1567 (2006).
- [223] M. Kan, S. Adhikari, and Q. Sun, *Phys. Chem. Chem. Phys.* **16**, 4990-4994 (2016).
- [224] C. Ataca, and H. Sahin, and S. Stable, *J. Phys. Chem. C* **116**, 8983-8999 (2012).
- [225] Y. Ma, Y. Dai, M. Guo, C. Niu, Y. Zhu, B. Huang, *ACS Nano* **6**, 1695-1701 (2013).
- [226] M. Bonilla, S. Kolekar, Y. Ma, H. C. Diaz, V. Kalappattil, R. Das, T. Eggers, H. R. Gutierrez, M. -H. Phan, and M. Batzill, *Nat. Nanotechnology* **13**, 289-293 (2018).

- [227] G. Duvjir, B. K. Choi, I. Jang, S. Ulstrup, S. Kang, T. T. Ly, S. Kim, Y. H. Choi, C. Jozwiak, A. Bostwick, E. Rotenberg, J. -G. Park, R. Sankar, K. -S. Kim, J. Kim, and Y. Jun Chang, *Nano. Lett.* **18**, 5432-5438 (2018).
- [228] C. Gong, L. Li, Z. Li, H. Ji, A. Stern, Y. Xia, T. Cao, W. Bao, C. Wang, Y. Wang, Z. Q. Qiu, R. J. Cava, S. G. Louie, J. Xia, X. Zhang, *Nature* **546**, 265-269 (2017).
- [229] B. Huang, G. Clark, E. N.-Moratalla, D. R. Klein, R. Cheng, K. L. Seyler, D. Zhong, E. Schmidgall, M. A. McGuire, D. H. Cobden, W. Yao, D. Xiao, P. J.-Herrero, and X. Xu, *Nature* **546**, 270-273 (2017).
- [230] B. Huang, G. Clark, D. R. Klein, D. MacNeill, E. N. -Moratalla, K. L. Seyler, N. Wilson, M. A. McGuire, D. H. Cobden, D. Xiao, W. Yao, P. J. -Herrero, and X. Xu, *Nat. Nanotechnology* **13**, 544–548 (2018).
- [231] S. Jiang, L. Li, Z. Wang, K. F. Mak, and J. Shan, *Nat. Nanotechnology* **13**, 549–553 (2018).
- [232] T. Bömerich, L. Heinen, and A. Rosch, *Phys. Rev. B* **102**, 100408(R) (2020).
- [233] Q. Tong, F. Liu, J. Xiao, and W. Yao *Nano Lett.* **18**, 7194-7199 (2018).
- [234] M. Akram, and O. Erten, *Phys. Rev. B* **103**, L14040 (2021).
- [235] M. Yang, Q. Li, R. V. Chopdekar, R. Dhall, J. Turner, J. D. Carlström, C. Ophus, C. Klewe, P. Shafer, A. T. N’Diaye, J. W. Choi, G. Chen, Y. Z. Yu, C. Hwang, F. Wang, and Z. Q. Qiu, *Science Advances* **6**, eabb5157 (2020).
- [236] T.-E. Park, L. Peng, J. Liang, A. Hallal, F. S. Yasin, X. Zhang, S. J. Kim, K. M. Song, K. Kim, M. Weigand, G. Schuetz, S. Finizio, J. Raabe, K. Garcia, J. Xia, Y. Zhou, M. Ezawa, X. Liu, J. Chang, H. C. Koo, Y. D. Kim, M. Chshiev, A. Fert, H. Yang, X. Yu, and S. Woo, *Phys. Rev. B* **103**, 104410 (2021).
- [237] T. H. R. Skyrme, A non-linear field theory. *Proc. Royal Soc. Lond. A: Math. Phys. Eng. Sci.* **260**, 127 (1961); T. H. R. Skyrme, A unified field theory of mesons and baryons. *Nucl. Phys.* **31**, 556 (1962).

- [238] N. Nagaosa and Y. Tokura, *Nature Nanotechnology* **8**, 899-911 (2013).
- [239] J. H. Han, *Skyrmions in Condensed Matter*, Springer Tracts in Modern Physics, Volume **278**
- [240] S. Mühlbauer, B. Binz, F. Jonietz, C. Pfleiderer, A. Rosch, A. Neubauer, R. Georgii, and P. Böni, *Science* **323**, 915-919 (2009).
- [241] W. Münzer, A. Neubauer, T. Adams, S. Mühlbauer, C. Franz, F. Jonietz, R. Georgii, P. Böni, B. Pedersen, M. Schmidt, A. Rosch, and C. Pfleiderer *Phys Rev. B* **81**, 041203(R) (2010).
- [242] X. Z. Yu, Y. Onose, N. Kanazawa, J. H. Park, J. H. Han, Y. Matsui, N. Nagaosa and Y. Tokura, *Nature* **465**, 901–904 (2010); D. Morikawa, K. Shibata, N. Kanazawa, X. Z. Yu, and Y. Tokura, *Phys. Rev. B* **88** 024408 (2013).
- [243] P. Milde, D. Köhler, J. Seidel, L. M. Eng, A. Bauer, A. Chacon, J. Kindervater, S. Mühlbauer, C. Pfleiderer, S. Buhrandt, C. Schütte, and A. Rosch, *Science* **340**, 1076-1080 (2013).
- [244] S. Seki, X. Z. Yu, S. Ishiwata, and Y. Tokura, *Science* **336**, 198-201 (2012).
- [245] Y. Tokunaga, X. Z. Yu, J. S. White, H. M. Ronnow, D. Morikawa, Y. Taguchi, and Y. Tokura, *Nat. Commun.* **6**, 7638 (2015).
- [246] X. Zhao, C. Jin, C. Wang, H. Du, J. Zang, M. Tian, R. Che, and Y. Zhang, *Proc. Natl. Acad. Sci.* **113**, 4918 (2016).
- [247] S. Heinze, K. von Bergmann, M. Menzel, J. Brede, A. Kubetzka, R. Wiesendanger, G. Bihlmayer, S. Blügel, *Nat. Phys.* **7**, 713-718 (2011);
- [248] Z. Hou, W. Ren, B. Ding, G. Xu, Y. Wang, B. Yang, Q. Zhang, Y. Zhang, E. Liu, F. Xu, W. Wang, G. Wu, X. -X. Zhang, B. Shen, Z. Zhang, *Advanced Materials* **29**, 1701144 (2017).
- [249] R. Wiesendanger, Nanoscale magnetic skyrmions in metallic films and multilayers: a new twist for spintronics. *Nat. Rev. Mat.* **1**, 16044 (2016).

- [250] A. K. Nayak, V. Kumar, T. Ma, P. Werner, E. Pippel, R. Sahoo, F. Damay, U. K. Rübler, C. Felser and S. S. P. Parkin, *Nature* **548**, 561-566 (2017).
- [251] W. Koshibae, and N. Nagaosa, *Nat. Commun.*, **7**, 10542 (2016); M. Hoffmann, B. Zimmermann, G. P. Müller, D. Schürhoff, N. S. Kiselev, C. Melcher, and S. Blügel *Nat. Commun.* **8**, 308 (2017)
- [252] N. Romming, C. Hanneken, M. Menzel, J. E. Bickel, B. Wolter, K. von Bergmann, A. Kubetzka, and R. Wiesendanger, *Science* **341**, 636-639 (2013).
- [253] J. Sampaio, V. Cros, S. Rohart, A. Thiaville, and A. Fert, *Nature Nanotechnology* **8**, 839–844 (2013).
- [254] M. Mochizuki, X. Z. Yu, S. Seki, N. Kanazawa, W. Koshibae, J. Zang, M. Mostovoy, Y. Tokura, and N. Nagaosa, *Nature Materials* **13**, 241–246 (2014).
- [255] W. Jiang, P. Upadhyaya, W. Zhang, G. Yu, M. B. Jungfleisch, F. Y. Fradin, J. E. Pearson, Y. Tserkovnyak, K. L. Wang, O. Heinonen, S. G. E. te Velthuis, and A. Hoffmann, *Science* **349**, 283-286 (2015).
- [256] A. Fert, N. Reyren, and V. Cros, *Nature Reviews Materials*, **2**, 17031 (2017); A. Fert, V. Cros, and J. Sampaio, *Skyrmions on the track. Nat. Nanotechnol.* **8**, 152-156 (2013).
- [257] S. S. P. Parkin, M. Hayashi, and L. Thomas, *Science* **320**, 190–194 (2008).
- [258] R. Tomasello, E. Martinez, R. Zivieri, L. Torres, M. Carpentieri, and G. Finocchio, *Sci. Rep.* **4**, 6784 (2014); P. F. Bessarab, G. P. Müller, I. S. Lobanov, F. N. Rybakov, N. S. Kiselev, H. Jónsson, V. M. Uzdin, S. Blügel, L. Bergqvist, and A. Delin, *Sci. Reports* **8**, 3433 (2018).
- [259] T. Bömerich, L. Heinen, and A. Rosch, arXiv:2004.13684v2;
- [260] C. Gong, L. Li, Z. Li, H. Ji, A. Stern, Y. Xia, T. Cao, W. Bao, C. Wang, Y. Wang, Z. Q. Qiu, R. J. Cava, S. G. Louie, J. Xia, and X. Zhang, *Nature* **546**, 265–269 (2017); M. Bonilla, S. Kolekar, Y. Ma, H. C. Diaz, V. Kalappattil, R. Das, T. Eggers, H. R. Gutierrez, M. -H. Phan, and M. Batzill, *Nat. Nanotech.* **13**, 289–293 (2018); D. J. ÓHara, T. Zhu, A.

- H. Trout, A. S. Ahmed, Y. K. Luo, C. H. Lee, M. R. Brenner, S. Rajan, J. A. Gupta, D. W. McComb, and R. K. Kawakami, *Nano Lett.* **18**, 3125-3131 (2018).
- [261] A. Bansil, H. Lin, T. Das, *Rev. Mod. Phys.* **88**, 021004 (2016); M. Z. Hasan, C. L. Kane, *Rev. Mod. Phys.* **82**, 3045 (2010); X. L. Qi, S. C. Zhang, *Rev. Mod. Phys.* **83**, 83, 1057 (2011).
- [262] A. Malozemoff, and J. Slonczewski, *Magnetic Domain Walls in Bubble Materials* (Academic press, 1979); A. H. Eschenfelder, *Magnetic bubble technology* (Springer-Verlag Berlin Heidelberg New York, 1980).
- [263] T. Bzdušek, Q. Wu, A. Rüegg, M. Sigrist, and A. A. Soluyanov, *Nature* **538**, 75–78 (2016).
- [264] P. Streda, *J. Phys. C: Solid State Phys.*, **15**, L717-L721 (1982).
- [265] P. Huang, *et al.* *Nat. Nanotech.* **15**, 761-767 (2020).
- [266] J. R. Schrieffer, X. G. Wen, and S. C. Zhang, *Phys. Rev. B* **39**, 11663 (1989).
- [267] J. R. Schrieffer, X. G. Wen, and S. C. Zhang, *Phys. Rev. B* **39**, 11663 (1989).
- [268] A. A. Abrikosov, *Methods of Quantum Field Theory in Statistical Physics* (Dover Books on Physics) (1975).
- [269] T. Kotani, M. van Schilfgaarde, S. V. Faleev, *Phys. Rev. B* **76**, 165106 (2007).

Appendix A

A.1 Extraction of the exponents

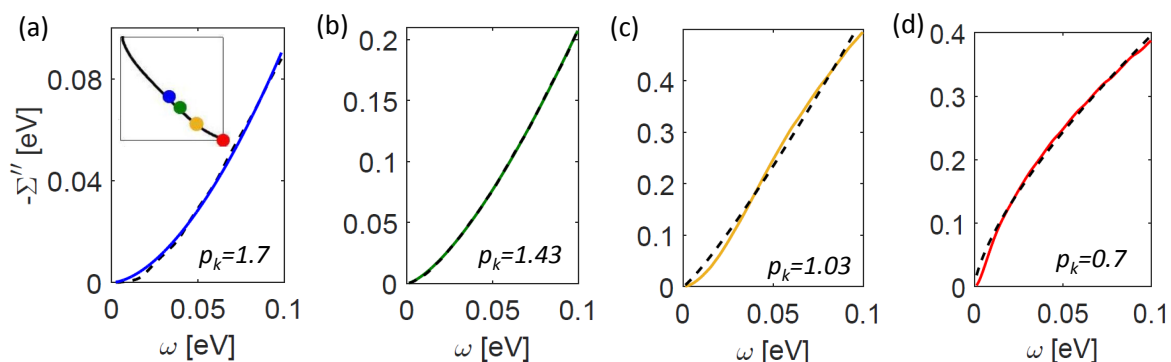


Figure A.1: Here I illustrate the curve fitting procedure. In (a-d) I plot $\Sigma''(\mathbf{k}, \omega)$ (solid line) and fitted curve (dashed line) at different points of BZ as given in Fig. 2.5. Same color scheme has been used as indicated in the inset of (a). The black dashed line is the fitted curve with a k-dependent exponent p_k upto a frequency limit ω_u .

As mentioned in chapter 2, the exponent p_k is also frequency dependent, but usually the frequency dependence is so small at low frequencies that one can approximate it as constant in this frequency range. This behavior is also observed in experiments where exponent is extracted using an upper limit (ω_u) in frequency, and ω_u is found to vary over the BZ.[119] In my calculations, I use a fixed ω_u (0.1 eV) since finding ω_u for every points of the BZ can be ambiguous. I then take the average of exponent in that frequency window. The procedure is illustrated by plotting the calculated and the fitted curves in Fig. A.1.

A.2 Details of the MRDF calculations

A.2.1 Self-energy dressed susceptibilities:

I start with the standard definition of spin/charge susceptibility [167, 266] which is given by

$$\chi^{ij}(\mathbf{q}, \tau) = \frac{1}{N} \langle T_\tau \Pi^i(\mathbf{q}, \tau) \Pi^j(-\mathbf{q}, 0) \rangle, \quad (\text{A.2.1})$$

where $\Pi^i(\mathbf{q}, \tau)$ denotes the spin/charge density where indices i, j denote different components (for example x, y, z components) in case of spin susceptibility. Charge and spin densities ($\Pi^i(\mathbf{q}, \tau)$) are given in the second quantized notation as

$$\rho_{\mathbf{q}}(\tau) = \sum_{\mathbf{k}, \sigma} c_{\mathbf{k}+\mathbf{q}, \sigma}^\dagger(\tau) c_{\mathbf{k}, \sigma}(\tau), \quad (\text{A.2.2})$$

$$S_{\mathbf{q}}^i(\tau) = \sum_{\mathbf{k}, \alpha, \beta} c_{\mathbf{k}+\mathbf{q}, \alpha}^\dagger(\tau) \sigma_{\alpha\beta}^i c_{\mathbf{k}, \beta}(\tau), \quad (\text{A.2.3})$$

where σ^i 's are the Pauli spin matrices in 2D. $c_{\mathbf{k}, \sigma}^\dagger(\tau)$ is the dressed quasi-particle creation operator (sometimes called Dyson orbital) at the Bloch momentum \mathbf{k} and spin σ . Since the ground state is spinless, both transverse and longitudinal spin-densities, as well as the charge density term yield the same bare susceptibility. In general, Eq. (A.2.1) can be written as

$$\chi(\mathbf{q}, \tau) = \frac{1}{N} \sum_{\mathbf{k}, \mathbf{k}', \sigma, \sigma', \sigma'', \sigma'''} \langle T_\tau S(\infty) c_{\mathbf{k}+\mathbf{q}, \sigma}^\dagger(\tau) c_{\mathbf{k}, \sigma'}(\tau) c_{\mathbf{k}'-\mathbf{q}, \sigma''}^\dagger(0) c_{\mathbf{k}', \sigma'''}(0) \rangle, \quad (\text{A.2.4})$$

where the momentum conservation law is imposed. $S(\infty)$ is the usual S-matrix which arises in the interaction picture.[267, 268] The four-field terms can be decomposed into bi-linear terms within the Wick's theorem, and the spin-conservation condition can be allowed for the ground state. I restrict to the bubble diagrams for the density-density correlations and the density vertex correction contains the ladder diagrams. Furthermore, I include only the RPA terms, with all the bubbles containing the same density vertex term. I am not including the higher order ladder diagrams here, which was derived by MT,[160] and AL.[161] These two terms are discussed in chapter 2 for the current-current correlation functions (Sec. 2.8.6), and

one would obtain similar terms for the density-density correlation term. I have showed that these terms give negligible contributions in the intermediate coupling range, and is discussed in Sec. 2.8.6. Since the ground state has both spin-rotational and gauge symmetry, the bare spin and charge susceptibilities are the same without the vertex term. They become decoupled in the RPA label, and give different self-energies for the spin and charge channels. In this MRDF self-consistent approximation, the vertex correction depends on the self-energy, and thus it has different contributions from the spin and charge sectors. Therefore, it makes more sense to decouple the bare spin ($\nu = 1$) and charge ($\nu = 2$) susceptibilities at this bare level, and I obtain

$$\begin{aligned}
\chi_\nu(\mathbf{q}, \tau) &= \frac{1}{N} \sum_{\mathbf{k}, \mathbf{k}', \sigma, \sigma', \sigma'', \sigma'''} \langle T_\tau c_{\mathbf{k}, \sigma'}(\tau) c_{\mathbf{k}' - \mathbf{q}, \sigma''}^\dagger(0) \delta_{\sigma' \sigma''} \rangle \langle T_\tau c_{\mathbf{k}', \sigma'''}(0) c_{\mathbf{k} + \mathbf{q}, \sigma}^\dagger(\tau) \delta_{\sigma \sigma'''} \rangle \\
&\quad \times \Gamma_\nu(\mathbf{k}, \mathbf{k} + \mathbf{q}, \tau), \\
&= \frac{1}{N} \sum_{\mathbf{k}, \sigma \sigma'} G_{\sigma'}(\mathbf{k}, \tau) G_\sigma(\mathbf{k} + \mathbf{q}, -\tau) \Gamma_\nu(\mathbf{k}, \mathbf{k} + \mathbf{q}, \tau),
\end{aligned} \tag{A.2.5}$$

where the terms in the brackets can be identified as self-energy dressed Green's functions. Using the Fourier transformation, I get

$$\begin{aligned}
\chi_\nu(\mathbf{q}, i\epsilon_m) &= \frac{1}{N\beta^2} \sum_{\mathbf{k}, n, n'} \int_0^\beta d\tau e^{(-i\omega_n + i\omega_{n'} + i\epsilon_m)\tau} \Gamma_\nu(\mathbf{k}, \mathbf{k} + \mathbf{q}, i\omega_n, i\epsilon_m) G(\mathbf{k}, i\omega_n) G(\mathbf{k} + \mathbf{q}, i\omega_{n'}), \\
&= \frac{1}{N\beta} \sum_{\mathbf{k}, i\omega_n} \Gamma(k, k + q) G(k) G(k + q).
\end{aligned} \tag{A.2.6}$$

Here I use compact, four-vector, notation $k = (\mathbf{k}, i\omega_n)$, and $k + q = (\mathbf{k} + \mathbf{q}, i\omega_n - i\epsilon_m)$, where $i\omega_n$ and $i\epsilon_m$ are the fermionic and bosonic Matsubara frequencies, respectively. From here onwards I drop the index σ and assume an implied sum over σ index. It is not easy to perform the Matsubara frequency summation using self-energy dressed Green's function. So I use its

spectral representation as

$$G(\mathbf{k}, i\omega_n) = \int_{-\infty}^{\infty} \frac{d\omega'}{2\pi} \frac{A(\mathbf{k}, \omega')}{i\omega_n - \omega'}, \quad (\text{A.2.7})$$

where the corresponding spectral weight defined as $A(\mathbf{k}, \omega) = -\text{Im}G(\mathbf{k}, \omega)/\pi$, where $G(\mathbf{k}, \omega)$ is obtained by taking the analytical continuation to the real frequency $i\omega_n = \omega + i\delta$, with δ being infinitesimal broadening. So the susceptibility expression becomes

$$\begin{aligned} \chi_\nu(q) = & \frac{1}{N} \sum_{\mathbf{k}} \int_{-\infty}^{\infty} \int_{-\infty}^{\infty} \frac{d\omega_1}{2\pi} \frac{d\omega_2}{2\pi} \Gamma_\nu(k, k+q) A(\mathbf{k}, \omega_1) A(\mathbf{k} + \mathbf{q}, \omega_2) \\ & \times \left(\frac{1}{\beta} \sum_n \frac{1}{i\omega_n - \omega_1} \frac{1}{i\omega_n - i\epsilon_m - \omega_2} \right). \end{aligned} \quad (\text{A.2.8})$$

Consistently, I define $q = (\mathbf{q}, i\epsilon_m)$. The term in the bracket can be evaluate by the Matsubara summation technique [167] and I arrive at the expression

$$\chi_\nu(q) = \frac{1}{N} \sum_{\mathbf{k}} \int_{-\infty}^{\infty} \int_{-\infty}^{\infty} \frac{d\omega_1}{2\pi} \frac{d\omega_2}{2\pi} A(\mathbf{k}, \omega_1) A(\mathbf{k} + \mathbf{q}, \omega_2) \Gamma(k, k+q) \frac{f(\omega_1) - f(\omega_2)}{i\epsilon_m - \omega_2 + \omega_1}, \quad (\text{A.2.9})$$

where $f(\omega)$ denotes the Fermi distribution function. The computation of the susceptibility is done using analytical continuation to the real frequency as discussed before. The susceptibility in the RPA becomes

$$\chi_\nu^{\text{RPA}}(q) = \frac{\chi_\nu(q)}{1 \pm U\chi_\nu(q)}, \quad (\text{A.2.10})$$

for charge and spin, respectively.

A.2.2 Self-energy

Next I calculate the self energy using the Hedin's approach,[162] which is given by

$$\Sigma_\nu(k) = -\frac{1}{N\beta} \sum_{\mathbf{q}, m} G(k+q) W_\nu(q) \Gamma(k, k+q). \quad (\text{A.2.11})$$

W is the fluctuation-exchange potential which can be obtained within the RPA as

$$W_\nu(q) = \frac{\eta_\nu}{2} U^2 \chi_\nu^{\text{RPA}}(q), \quad (\text{A.2.12})$$

where $\eta = 3$ and 1 for spin ($\nu = 1$) and charge ($\nu = 2$) density fluctuations. Again, to aid the Matsubara frequency summation, I use the spectral representation of W as

$$W_\nu(\mathbf{q}, i\epsilon_m) = \int_{-\infty}^{\infty} \frac{d\varepsilon'}{2\pi} \frac{\text{Im}[W_\nu(\mathbf{q}, \varepsilon')]}{i\epsilon_m - \varepsilon'}. \quad (\text{A.2.13})$$

I denote the fluctuation-exchange potential as $V_\nu(\mathbf{q}, \varepsilon) = \text{Im}[W_\nu(\mathbf{q}, \varepsilon)]$. Therefore, using Eqs. (A.2.11) and (A.2.13), I get

$$\begin{aligned} & \Sigma_\nu(k) \\ &= -\frac{1}{N} \sum_{\mathbf{q}} \int_{-\infty}^{\infty} \frac{d\varepsilon}{2\pi} \int_{-\infty}^{\infty} \frac{d\omega'}{2\pi} A(\mathbf{k} - \mathbf{q}, \omega') V_\nu(\mathbf{q}, \varepsilon) \Gamma(k, k + q) \\ & \quad \times \left(\frac{1}{\beta} \sum_{\epsilon_m} \frac{1}{i\omega_n - i\epsilon_m - \omega'} \frac{1}{i\epsilon_m - \varepsilon} \right) \\ &= \frac{1}{N} \sum_{\mathbf{q}} \int_{-\infty}^{\infty} \frac{d\varepsilon}{2\pi} \int_{-\infty}^{\infty} \frac{d\omega'}{2\pi} A(\mathbf{k} - \mathbf{q}, \omega') V_\nu(\mathbf{q}, \varepsilon) \Gamma(k, k + q) \frac{f(-\omega') + n(\varepsilon)}{i\omega_n - \omega' - \varepsilon}, \quad (\text{A.2.14}) \end{aligned}$$

$$\begin{aligned} &= \frac{1}{N} \sum_{\mathbf{q}} \int_{-\infty}^{\infty} \frac{d\varepsilon}{2\pi} \int_{-\infty}^{\infty} \frac{d\omega'}{2\pi} A(\mathbf{k} - \mathbf{q}, \omega') V_\nu(\mathbf{q}, \varepsilon) \Gamma(k, k + q) \\ & \quad \times \left[\frac{1 - f(\omega') + n(\varepsilon)}{i\omega_n - \omega' - \varepsilon} + \frac{f(\omega') + n(\varepsilon)}{i\omega_n - \omega' + \varepsilon} \right]. \quad (\text{A.2.15}) \end{aligned}$$

All other symbols are defined in chapter 2.

The MRDF method is very similar to the Hedin's equations of self-energy calculation using density-density fluctuations[162]. Different approximations are usually distinguished by different models, such as FLEX[134] or GW methods[164, 269]. In the FLEX approach[134], one calculates the single-particle green's function self-consistently, but not the two-particle one. The extension of the FLEX method where both the single-, and two-particle terms include self-energy correction in a self-consistent way is called the mode-mode coupling theory.[175, 138] While in the GW-approach, one often neglects the vertex correction or use a quasiparticle–GW approximation etc[269]. In this MRDF approach, the single-particle

Green's function, the density-density correlation function, and the vertex correction are calculated by including the self-energy correction.

Appendix B

B.1 Ground state spin configurations

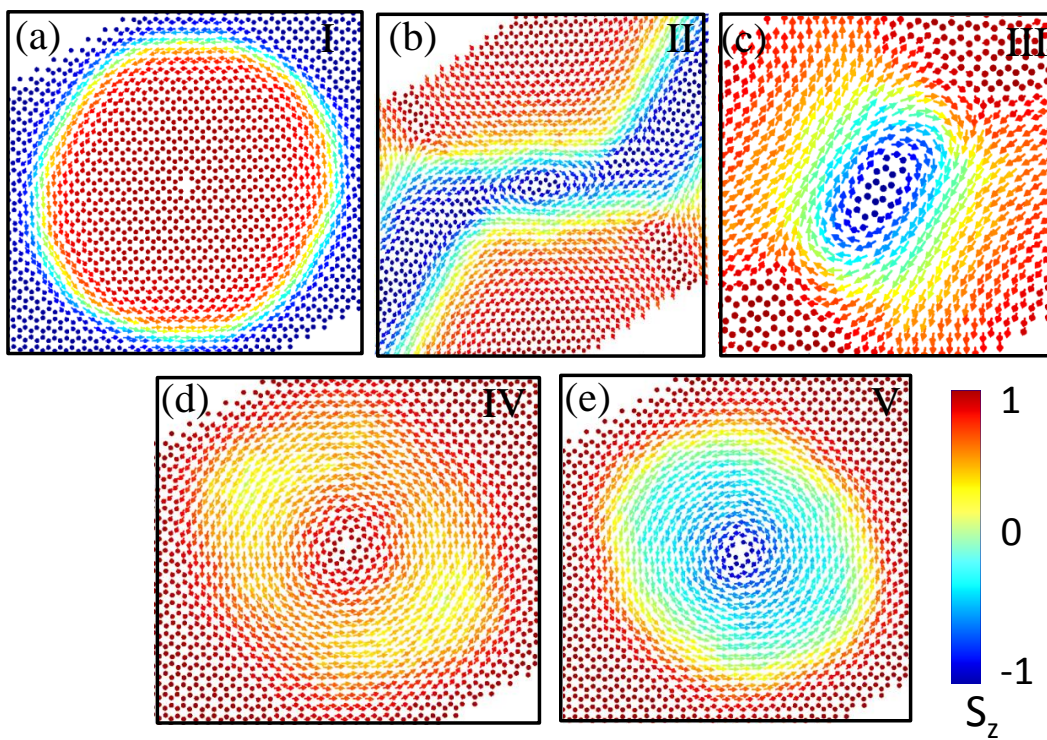


Figure B.1: Ground state spin configurations from Monte Carlo simulation for different phases.

B.2 Dipole and quadrupole moments in Phase II

The field lines in phase II shown in Fig. 4.6(c) indicate that the charge distribution can be approximated with point charges ($q_i, i = 1, 2, 3, 4, 5$) as shown in Fig. 4.6(f). As the total charge of this configuration is zero the higher moments (dipole and quadrupole) of this charge distribution are investigated. Dipole moment is calculated for charge pair (q_1, q_2) and (q_4, q_5) and taking the origin of the co-ordinate at one of the charge center (see Fig. 4.6(f)) the quadrupole moments are calculated, which are given by

$$Q = \begin{bmatrix} Q_{xx} & Q_{xy} \\ Q_{yx} & Q_{yy} \end{bmatrix} = \begin{bmatrix} \sum_i \rho_i x_i x_i & \sum_i \rho_i x_i y_i \\ \sum_i \rho_i y_i x_i & \sum_i \rho_i y_i y_i \end{bmatrix} \quad (\text{B.2.1})$$

Values of the dipole and quadrupole moments for Phase II are given in table B.1.

Table B.1: Values of charge, dipole moments, quadrupole moments in phase II for two different dipole coupling strengths (J_D). (x,y) are given in unit of Moiré lattice constant $35.6a_0$. *caution: the estimate of the fractional charge is subjected to the integration contour around each charge centers, since there is no compact domain wall boundary here.*

quantities	$J_D = 0.53$	$J_D = 1.0$
q_1	-0.23	-0.23
q_2	0.22	0.22
q_3	-0.25	-0.24
q_4	0.22	0.24
q_5	-0.20	-0.22
(x_1, y_1)	(0.20 , 0.07)	(0.20 , 0.07)
$(x_2, -y_2)$	(0.35 , -0.09)	(0.35 , -0.09)
\mathbf{p}_1	$0.033\hat{x} + 0.035\hat{y}$	$0.033\hat{x} + 0.035\hat{y}$
\mathbf{p}_2	$-0.033\hat{x} - 0.035\hat{y}$	$-0.034\hat{x} - 0.037\hat{y}$
Q_{xx}	-0.035	-0.037
Q_{yy}	-0.001	-0.001
Q_{xy}	0.021	0.020

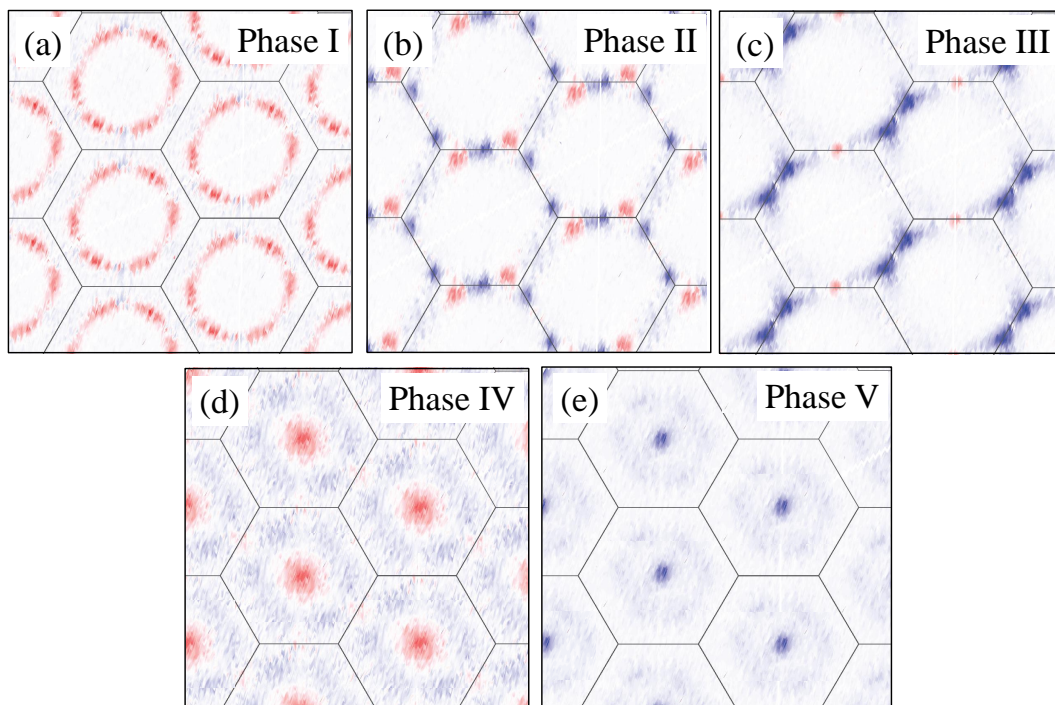


Figure B.2: Plots of topological charge density in many Moiré unit cells.